Jelena Todorovic

Correlated Transmission Electron Microscopy and Micro-photoluminescence Studies of GaAs-based Heterostructured Semiconductor Nanowires

Thesis for the degree of Philosophiae Doctor

Trondheim, December 2012

Norwegian University of Science and Technology
Faculty of Natural Sciences and Technology
Department of Physics

NTNU – Trondheim
Norwegian University of
Science and Technology

NTNU
Norwegian University of Science and Technology

Thesis for the degree of Philosophiae Doctor

Faculty of Natural Sciences and Technology
Department of Physics

© Jelena Todorovic

ISBN 978-82-471-3958-5 (printed ver.)
ISBN 978-82-471-3959-2 (electronic ver.)
ISSN 1503-8181

Doctoral theses at NTNU, 2012:319

Printed by NTNU-trykk

Abstract

The focus of this work was to study the nanowire (NW) optical and structural properties on a single NW level. The GaAs-based heterostructured semiconductor NWs, grown by Au-assisted molecular beam epitaxy (MBE), were studied throughout this work. Due to diversity of the NWs within each growth batch, it is essential to study the same single NWs both by different micro-photoluminescence (PL) and transmission electron microscopy (TEM) techniques. An efficient method for such a correlated study was developed (paper I), and applied in all following studies. The key feature is that the single NWs of desired morphology are preselected by low voltage scanning TEM (STEM) for the micro-PL study. Subsequently, TEM characterization is performed, and in such a way a detailed set of information is obtained for each single NW.

Wurtzite (WZ) GaAs/AlGaAs core-shell NWs were studied to determine the fundamental optical properties of WZ GaAs, a crystal phase found only in NW form for GaAs (paper III). To this cause, low temperature power-dependent, temperature-dependent, polariztion-resolved and time-resolved micro-PL were employed in correlation with conventional TEM characterization. The room temperature (294 K) WZ GaAs bandgap was determined to be 1.444 eV $\pm$ 1 meV which is $\sim$ 20 meV higher than the well known bulk zinc blende (ZB) GaAs value. On the other hand, the low temperature free exciton emission energy was found to be approximately the same as in ZB GaAs, 1.516 eV at 15 K. The conduction band symmetry of WZ GaAs is proposed to be Γ_8. In addition, the results demonstrate that the Au-assisted MBE grown NWs can have high PL brightness.

WZ GaAs/ZB GaAsSb axially heterostructured NWs were studied in order to understand the cause of variations of the ZB GaAsSb insert optical properties among the NWs (paper I, II, IV). The Sb concentration variation among and within ZB GaAsSb inserts was studied by energy dispersive X-ray spectroscopy (EDX), quantitative high angle annular dark field (HAADF) STEM and correlated PL-TEM (paper IV). A clear trend

of increasing Sb concentration with increasing insert length was observed. It was found that the Sb concentration increases gradually from the lower insert interface along the NW axis, reaches a maximum value and decreases towards the upper insert interface. The Sb concentration variation within the GaAsSb inserts induces both type I and type II optical transitions within the insert. To verify the EDX and quantitative HAADF STEM results independently, the Sb concentration was calculated from the ground state energies of the GaAsSb PL emission using an empirical model for low temperature bandgap of unstrained bulk GaAsSb. The calculated Sb concentration values were in agreement with quantitative HAADF STEM results, and systematically higher than the values obtained by the EDX quantification.

Acknowledgements

First of all, I would like to thank my supervisor Associate Professor A. T. J. van Helvoort for all that he taught me, for creative discussions and for his constant interest in my work. I am grateful for his support, for his pursue of my best interests and for the generous help he offered me in the course of my PhD.

I would also like to thank my co-supervisor Professor Helge Weman for his support, for the constructive criticism of my work, for always asking questions to think about and for offering many explanations. Professor Bjørn-Ove Fimland deserves my gratitude as well, for his support and for help in improving my manuscripts. The NW growers, Dheeraj and Mazid, deserve special acknowledgement for growing the most intriguing and complex NW heterostructures which challenged us both experimentally and when it comes to interpretation of the optical properties in correlation with the structure, composition and defects.

I also want to thank my colleagues and co-authors for their cooperation and interesting and inspiring discussions which led to a deeper understanding of the problems we were dealing with. I thank NTNU Nanolab for the access to Hitachi S5500, my favourite little microscope, which was an essential part of my work. Special thanks goes to Bjørn Soleim for helping me whenever I had troubles with the microscopes. Thanks to the successful PhD students in the previous two years, Dheeraj, Malin and Ruben, for the inspiration to write the Introduction for my thesis. I would also like to thank Professor Randi Holmestad and the colleagues from TEM Gemini Centre for friendly and relaxing atmosphere at work.

It takes two to tango. It also takes two to do a correlated PL-TEM study. And as in tango, there are distinct roles: a leader and a follower. Without good communication and connection between the two, the dance is impossible. The same happens in such a close collaboration. So, special thanks goes to my PL colleagues and good friends, Lyubomir and Phillip. Without them this work would have been impossible.

Hvala to my family and friends from Beograd for believing in me and for 24/7 Skype availability. Tusen takk to my friends here, for always being there for me and for all the fun times we spent together. I would like to thank Hanne for sharing these three years with me in the office, for listening to me and talking through all sort of problems, and for helping me a lot with the last manuscript. And one big abrazo to the tango dancers, here and scattered around the world, for transcending my consciousness from the PhD mode to tango space-time during the last two years.

Trondheim, September 2012

Jelena Todorović

Preface

This thesis is submitted in partial fulfilment of the requirements for the PhD degree at the Norwegian University of Science and Technology (NTNU). This PhD project was a part of the project “Development of semiconductor nanowire based solar cells” financed by the “RENERGI” program (Grant No. 190871) of the Research Council of Norway. The work has been caried out at TEM Gemini Centre at the Department of Physics from September 2009 to September 2012. The NWs were grown in the MBE lab at the Department of Electronics and Telecommunications (IET), NTNU. SEM/STEM characterization has been performed at NTNU Nanolab. The optical characterization of the NWs has been carried out in the Nano Photonics lab at IET, NTNU.

The thesis consists of two parts. Part I contains the introduction about the studied GaAs-based heterostructured semiconductor NWs, theoretical background and description of experimental techniques used in this work. The introduction about the NWs includes Au-assisted MBE growth procedures, description of NW crystal structure, defects and morphology, and some examples of correlated PL-TEM studies carried out within this PhD. The theoretical background focuses on the theory of electron diffraction, description of NW crystal phases and derivation of the structural factors for the two dominant crystal phases. The experimental part describes MBE, micro-PL and the different electron microscopy techniques used in this work. Part I ends with a summary of the entire PhD project, including the main conclusions and an outlook for future correlated studies based on the developed PL-TEM method. Part II contains the collection of own journal publications and manuscripts either accepted or to be submitted.

Included papers

I *Correlated micro-photoluminescence and electron microscopy studies of the same individual heterostructured semiconductor nanowires.* J. Todorovic, A. F. Moses, T. Karlberg, P. Olk, D. L. Dheeraj, B. O. Fimland, H. Weman and A. T. J. van Helvoort. Nanotechnology **22**(32) (2011) 325707.

II *Correlated micro-photoluminescence and electron microscopy study of a heterostructured semiconductor nanowire.* J. Todorovic, A. F. Moses, D. L. Dheeraj, P. Olk, B. O. Fimland, H. Weman and A. T. J. van Helvoort. Journal of Physics: Conference Series **326** (2011) 012043.

III *A story told by a single nanowire: Optical properties of wurtzite GaAs.* L. Ahtapodov, J. Todorovic, P. Olk, T. S. Mjåland, P. Slåttnes, D. L. Dheeraj, A. T. J. van Helvoort, B. O. Fimland and H. Weman. Accepted in Nano Letters. DOI: 10.1021/nl3025714.

IV *Antimony concentration variation among and within zinc blende GaAsSb inserts in wurtzite GaAs and GaAs/AlGaAs core-shell nanowires.* J. Todorovic, H. Kauko, L. Ahtapodov, A. F. Moses, P. Olk, D. L. Dheeraj, B. O. Fimland, H. Weman and A. T. J. van Helvoort. *To be submitted.*

The co-authors listed above have contributed to these papers either through experimental or numerical work, or analysis, presentation and interpretation of the results, or writing of the papers.

D. L. Dheeraj has grown the NWs for all four papers and contributed to the interpretation and discussion in paper IV. The micro-PL measurements were performed mostly by A. F. Moses in papers I, II and IV. T. Karlberg (paper I), T. Mjåland (paper III) and P. Slåttnes (paper III) helped with the micro-PL measurements. HAADF STEM images in paper II were acquired by A. T. J. van Helvoort. L. Ahtapodov performed all micro-PL experiments and complete analysis of the PL results for paper III and wrote the manuscript. In addition, L. Ahtapodov performed PL-related calculations, helped with PL calibration and contributed to the interpretation and discussion in paper IV. H. Kauko performed the experimental and quantitative HAADF STEM and the corresponding EDX, and contributed to the interpretation and discussion in paper IV. P. Olk, B. O. Fimland, H. Weman and A. T. J. van Helvoort contributed to the interpretation, discussion and presentation of the results in all four papers.

My experimental contribution in all four papers was PL-TEM sample preparation, single NW mapping and pre-selection by optical microscopy and low voltage STEM, and finally conventional TEM/HAADF STEM/EDX characterization. For papers I, II and IV, I collected together and analysed all experimental PL-TEM results, did the initial interpretation of the results and wrote the manuscripts.

Co-authored papers

- *Crystal phase tuning in self-catalyzed GaAs nanowires by modifying the Ga droplet contact angle*, A. M. Munshi, D. L. Dheeraj, J. Todorovic, A. T. J. van Helvoort, B. O. Fimland, and H. Weman. *To be submitted.*

My contribution to this work was BF TEM and HRTEM imaging of the NWs of interest at the Jeol 2010F microscope.

Conference presentations

Presenter underlined.

- *Correlated micro-photoluminescence and electron microscopy studies of individual heterostructured semiconductor nanowires.* J. Todorovic, A.F. Moses, T. Karlberg, D.L. Dheeraj, P. Olk, B.O. Fimland, H. Weman and A.T.J. van Helvoort. Microscopy of Semiconducting materials 2011 (MSM XVII), 4-7 April, Churchill College, Cambridge, UK.

- *Consecutive micro-PL and TEM on a single GaAs/AlGaAs nanowire with a GaAsSb insert.* A.F. Moses, J. Todorovic, D.L. Dheeraj, T. Karlberg, P. Olk, A.T.J. van Helvoort, B.O. Fimland and H. Weman. MRS Spring meeting, 25-29 April 2011, San Francisco, California, USA.

- *Consecutive optical and structural characterization of a single heterostructured III-V semiconductor nanowire.* A.F. Moses, J. Todorovic, D.L. Dheeraj, P. Olk, A.T.J. van Helvoort, B.O. Fimland and H. Weman. 2nd Nano-network Workshop, 15-17 June 2011, Oslo, Norway.

- *Combined studies of single Au-assisted GaAs/AlGaAs core-shell nanowires with PL spectroscopy and TEM.* L. Ahtapodov, P. Olk, J.

Todorovic, T.S. Mjåland, M. Eriksson, P. Bergman, D.L. Dheeraj, A.T.J. van Helvoort, B.O. Fimland and H. Weman. PDI Topical Workshop on MBE-grown Arsenide Nanowires, 8-9 September 2011, Berlin, Germany.

- *Combined studies of single Au-assisted GaAs/AlGaAs core-shell nanowires with PL spectroscopy and TEM.* L. Ahtapodov, P. Olk, J. Todorovic, T.S. Mjåland, M. Eriksson, P. Bergman, D.L. Dheeraj, A.T.J. van Helvoort, B.O. Fimland and H. Weman. 4th Meeting of the French GDR "Nanofils Semiconducteurs", 17-21 October 2011, Porquerolles, France.

- *Optical spectroscopy of single semiconductor nanowires.* L. Ahtapodov, P. Olk, J. Todorovic, T.S. Mjåland, D.L. Dheeraj, A.T.J. van Helvoort, B.O. Fimland and H.Weman. 6th Nanolab User Meeting, 16 November 2011, Trondheim, Norway.

- *Crystal phase and position control of self-catalyzed GaAs nanowires grown on a Si substrate.* A.M. Munshi, D.L. Dheeraj, D.C. Kim, J. Todorovic, A.T.J. van Helvoort, B.O. Fimland, and H. Weman. 6th Nanolab User Meeting, 16 November 2011, Trondheim, Norway.

- *Zinc blende and wurtzite GaAs nanowires grown by self-catalyzed molecular beam epitaxy.* A.M. Munshi, D. L. Dheeraj, J. Todorovic, A. T. J. van Helvoort, B. O. Fimland and H. Weman. MRS Spring meeting, 8-13 April 2012, San Francisco, USA.

- *Wurtzite vs. Zinc Blende GaAs: A Thorough Comparison.* L. Ahtapodov, P. Olk, J. Todorovic, T. S. Mjåland, P. R. T. Slåttnes, D. L. Dheeraj, A. T. J. van Helvoort, B. O. Fimland and H. Weman. MRS Spring meeting, 8-13 April 2012, San Francisco, California, USA.

- *Photocurrent study of single wurtzite GaAs/AlGaAs core-shell nanowires.* D.C. Kim, L. Ahtapodov, D.L. Dheeraj, J. Todorovic, A.T.J. van Helvoort, B.O. Fimland and H. Weman. MRS Spring meeting, 8-13 April 2012, San Francisco, USA.

- *GaAs nanowires grown on Si substrates: Crystal phase perfection, heterostructures and position control.* A.M. Munshi, D.L. Dheeraj, D.C. Kim, J. Todorovic, O.M. Christoffersen, A.T.J. van Helvoort, B.O. Fimland and H. Weman. 3rd Nano-network Workshop, 11-13 June 2012, Trondheim, Norway.

- *Correlation of optical and structural properties of single semiconductor heterostructured nanowires.* J. Todorovic, A.F. Moses, L. Ahtapodov, P. Olk, D.L. Dheeraj, H. Kauko, B.O. Fimland, H. Weman and A.T.J. van Helvoort. Scandinavian Society for Electron Microscopy (SCANDEM), 13-15 June 2012, Bergen, Norway.

- *Combined micro-photoluminescence and electron microscopy investigation of single GaAs nanowires.* L. Ahtapodov, P. Olk, J. Todorovic, T.S. Mjåland, P.R.T. Slåttnes, D.L. Dheeraj, A.T.J. van Helvoort, B.O. Fimland and H. Weman. 31st ICPS Zurich, 29 July - 03 August 2012, Switzerland.

- *Crystal phase tuning in self-catalyzed GaAs nanowires induced by Ga-droplet contact angle.* A. M. Munshi, D. L. Dheeraj, J. Todorovic, A. T. J. van Helvoort, B. O. Fimland and H. Weman. MBE2012, 23-28 September 2012, Nara, Japan.

Posters

- *Insights into growth mechanisms of self-catalyzed GaAs nanowires grown by molecular beam epitaxy.* A.M. Munshi, D.L. Dheeraj, J. Todorovic, A.T.J. van helvoort, B.O. Fimland and H. Weman. MRS Spring Meeting, 25-29 April 2011, San Francisco, California, USA.

- *Positioned self-catalyzed GaAs nanowire arrays on Si substrates grown by molecular beam epitaxy.* A.M. Munshi, D.C. Kim, D.L. Dheeraj, J. Todorovic, A.T.J. van Helvoort, B.O. Fimland and H. Weman. 2nd Nano-network Workshop, 15-17 June 2011, Oslo, Norway. Won poster price.

- *Characterization of single GaAs nanowires with combined micro-PL spectroscopy and TEM on the same nanowire.* L. Ahtapodov, J. Todorovic, P. Olk, T.S. Mjåland, P.R.T. Slåttnes, D.L. Dheeraj, A.T.J. van Helvoort, B.O. Fimland and H. Weman. 3rd Nano-network Workshop, 11-13 June 2012, Trondheim, Norway.

Abbreviations

{111}A/B - a {111} surface terminated with group III/V element
BF - bright field
BSE - backscattered electron
CCD - charge-coupled device
DF - dark field
DP - diffraction pattern
EDX - energy dispersive X-ray spectroscopy
HAADF - high angle annular dark field
HRTEM - high resolution transmission electron microscopy
MBE - molecular beam epitaxy
ML - monolayer
NW - nanowire
PL - photoluminescence
SAED - selected area electron diffraction
SE - secondary electron
SEM - scanning electron microscopy
SF - stacking fault
STEM - scanning transmission electron microscopy
TDS - thermal diffuse scattering
TEM - transmission electron microscopy
VLS - vapour-liquid-solid
WZ - wurtzite
ZB - zinc-blende

Contents

I Introduction **1**

1 Introduction and Motivation **3**

2 Heterostuctured GaAs-based semiconductor NWs **9**
2.1 MBE growth of Au-assisted GaAs-based NWs 9
2.2 Crystal phases and defects 11
2.3 NW morphology 14
2.4 NW faceting 15
2.5 Heterostructured NWs studied by correlated PL-TEM 20
2.5.1 WZ GaAs/AlGaAs core-shell NWs 20
2.5.2 WZ GaAs inserts in WZ AlGaAs NWs 23

3 Theoretical background **25**
3.1 Theory of electron diffraction 25
3.1.1 Scattering of electrons from a single atom 26
3.1.2 Kinematical theory of electron diffraction 27
3.1.3 DF image contrast in the kinematical theory 31
3.1.4 Dynamical theory of electron diffraction 32
3.2 Crystal phases and Structure factors 35
3.2.1 Space groups for ZB and WZ GaAs 35
3.2.2 The Structure factor for ZB 36
3.2.3 The Structure factor for WZ 38

4 Experimental Techniques **41**
4.1 Molecular beam epitaxy 41
4.2 Micro-photoluminescence 42
4.3 The Transmission Electron Microscope 47
4.3.1 Introduction to TEM 47
4.3.2 Conventional TEM 48
4.3.3 High resolution TEM 51

4.3.4 Scanning TEM 53
4.3.5 Energy dispersive X-ray spectroscopy 54
4.4 The Scanning Electron Microscope 58

5 Conclusions and Outlook 61
5.1 Summary and Conclusions 61
5.2 Outlook 64

References 67

II Papers 75

6 Correlated micro-photoluminescence and electron microscopy studies of the same individual heterostructured semiconductor NWs 77

7 Correlated micro-photoluminescence and electron microscopy study of a heterostructured semiconductor NW 79

8 A Story Told by a Single Nanowire: Optical Properties of WZ GaAs 81

9 Antimony concentration variation among and within zinc blende GaAsSb inserts in wurtzite GaAs and GaAs/AlGaAs core-shell nanowires 83

Part I

Introduction

Chapter 1

Introduction and Motivation

A bright future within a broad range of applications is expected for the vast variety of heterostructured semiconductor nanowires (NWs) [1, 2]. The NW research worldwide has been expanding during the last decade within many applications, such as solar cells [3–5], lasers [6–9], transistors [10] and light emitting diodes [11].

Semiconductor NWs as a solar cell material [12], have a great potential to reduce the cost and to improve the efficiency of a solar cell device. NWs have several important advantages over thin films for solar cell applications. In a NW, electrons and holes move across a short distance (order of 100 nm in radial direction) and therefore the electron-hole recombination rate is reduced. Good optical absorption is achieved since the light is mainly absorbed along the NW axis. Moreover, NWs accommodate strain easily and can be grown on cheap and lattice-mismatched substrates [13,14]. The first NW solar cells using Si as an active material were demonstrated in 2007 [3, 4]. Compared to Si, the advantage of GaAs is a direct bandgap and thus more efficient absorption of light. The solar cell efficiency for GaAs NWs is expected to be higher by a factor or two compared to Si NWs, due to the bandgap type and a better optimized bandgap to the solar radiation spectrum [15].

The long-term aim of the NW project where this PhD was a part of, is to realize a solar cell consisting of a GaAs-based core-shell NW heterostructure with a p-type core, intrinsic-GaAs shell and a n-type shell, grown on a Si substrate. Moreover, positioned self-catalysed NW growth needs to be achieved by patterning the Si substrate, which is a part of another PhD within the NW project. This has already been demonstrated for self-catalysed GaAs NWs grown by molecular beam epitaxy (MBE) on patterned SiO_2 [13], and for other semiconductor NWs using various growth techniques [16].

For solar cell applications, bandgap design of the active material is an important requirement. This is well possible for the two most commonly used growth techniques for III-V semiconductor NWs, metalorganic vapour phase epitaxy (MOVPE) and MBE. Bandgap engineering is achieved by controlling and tuning the composition of a ternary III-V alloy [17]. The bandgap also depends on the crystal phase of the material [17, 18]. As different polytypes of a same material can exist at the nm-scale, different bandgaps can be expected as well. The crystal phase and bandgap control in NWs is achieved by alloying [19, 20] or by varying growth parameters [21, 22].

The basic building blocks for NW heterostructure design are axial inserts, of different crystal phase and/or material than the surrounding core, and radial shells, which commonly follow the core crystal structure [23, 24]. These building blocks allow vast freedom of design both for MBE and MOVPE. For example, complex NW heterostructures, such as twinning [25] or polytypic superlattices [26, 27] can be achieved for some III-V systems by MOVPE. Achieving such a precise growth control is more challenging in MBE, and there have been some recent developments towards crystal phase control [28] and superlattices [29], for example.

In general, NWs from a same growth batch usually exhibit variation in the structural characteristics and often suffer from inherent structural defects [19, 20, 26, 30]. The most common defects, stacking faults (SFs) in wurtzite (WZ) phase or twinning in zinc blende (ZB) phase, are expected to influence the NW optical properties. Moreover, NWs may grow with $\{111\}$A/B facets [25, 26] or a mixture of hexagonal ($\{11\bar{2}0\}$ or $\{1\bar{1}00\}$) and other facets [31, 32], which might hinder applications where perfect hexagonal morphology is needed.

While a significant amount of research is invested in optimising NW growth, exploring new NW heterostructures and designing new NW devices, understanding the fundamental physical properties of such complex nano-systems still remains a challenge. The question is to which extent the inherent NW imperfections, such as the structural defects and potential composition variation, influence the targeted opto-electronic properties for a device application.

The NWs studied in this PhD were based on WZ GaAs (core or axial insert) and ternary alloys WZ AlGaAs (radial shell or core) and GaAsSb (ZB axial insert or WZ radial shell). As an introduction to these alloys, the room temperature bandgaps for bulk ZB $Al_xGa_{1-x}As$ and ZB $GaAs_{1-x}Sb_x$ as a function of the content, x, are presented in figure 1.1. The bandgaps of WZ AlAs and WZ GaSb are predicted to be lower than for their ZB phase, and WZ GaAs bandgap remains lower than for WZ AlAs [18]. Thus, for a

GaAs/AlGaAs heterostructure type I band alignment (carriers confined in GaAs) and the absence of strain due to lattice-match (see inset of figure 1.1) are expected. On the other hand, for a GaAs/GaAsSb heterostructure strain should be expected. Presently, there is no consensus on the type of band alignment of ZB or WZ GaAs/ZB GaAsSb heterojunction, and both type I and type II are reported for ZB GaAs/GaAsSb quantum wells and pseudomorphic ZB GaAsSb thin films on ZB GaAs [33–38].

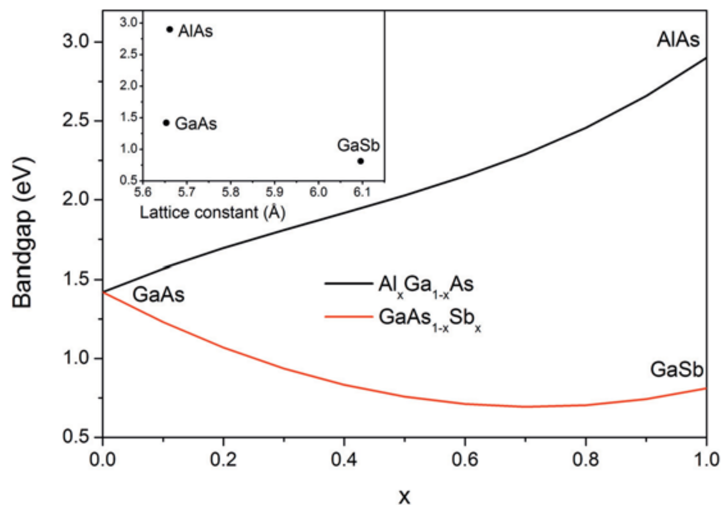

Figure 1.1: The room temperature bandgap as a function of the content, x, for bulk ZB ternary alloys $Al_xGa_{1-x}As$ and $GaAs_{1-x}Sb_x$. (Inset) Bandgap versus the lattice constant for bulk ZB GaAs, ZB AlAs and ZB GaSb. The figure is adapted from reference [17].

One of the aims of this PhD project was to support the MBE growth and micro-photoluminescence (PL) characterization by routine (scanning) transmission electron microscopy ((S)TEM) studies of novel GaAs-based heterostructured NWs. Conventional TEM characterization of NW size, morphology, crystal phases and lattice defects is important for the interpretation of the optical properties as well as a feedback for optimisation of the growth procedures. In addition, high angle annular dark field (HAADF) STEM and energy dispersive X-ray spectroscopy (EDX) provide information about the structural quality of a core-shell structure and give a rough insight into the concentration of different elements in a heterostructured NW. At the nm-scale, the basic TEM studies show that every NW is different. Namely, there can be a huge variation not only in NW sizes, but more importantly in defect type, density and distribution, for NWs within a sin-

gle batch. The time-consuming nature of (S)TEM work combined with the variation among the NWs and huge number of NWs in each growth batch, presents a challenge in obtaining reasonable statistics on the NW structural characteristics for a single batch.

On the other hand, micro-PL characterization faces its own challenges in studying NWs. The resolution of the objective lens in a micro-PL setup is not high enough to distinguish single NWs from the NWs that stick together, or to spot NW fragments. To make a micro-PL study meaningful, one must be certain that the measured object is a single NW. In addition, information about the NW structural characteristics is necessary to support the interpretation of the PL results. However, standard substrates for PL measurements are not electron transparent. Therefore, in case of a separate PL and TEM characterization, the interpretation of the PL results depends on some other NWs from the same batch, studied by TEM, which might be significantly different than those studied by PL. The interpretation of the optical properties in such an uncorrelated study may be based on the wrong assumptions and hence inaccurate.

Therefore, a need for establishing a correlated PL-TEM method emerged as another aim of this PhD project. The main motivation was to interpret the NW optical properties in direct correlation with its structure and composition. A significant part of this work was devoted to development of an efficient PL-TEM method (paper I). At the time of onset of this part of the project (beginning of 2010), a few correlated PL-TEM studies on NWs had been reported [39, 40]. In 2011, a correlated study of GaAs NWs by Heiss et al. [41], similar to our approach, has been published. By the time paper I was published (July 2011), there was still no routine application of the correlated PL-TEM characterization within the NW community.

The starting point was to find a TEM grid appropriate for micro-PL measurements and to adapt it for PL sample stage. Most importantly, we needed a tool for pre-selecting single NWs suitable for PL studies, and for mapping the NWs within the specimens. To this cause, a systematic study of the effects of electron beam exposure in Hitachi S5500 (1-30 kV) and Phillips CM30 (200 kV), on NW optical properties needed to be carried out. Low voltage (30 kV) scanning electron microscopy (SEM) or STEM proved to be a non-destructive and quick way for NW selection. Already at this stage, the obtained results led to a better understanding of the correlation between the optical and structural properties of axially and radially heterostructured NWs. Even though the main aim was to establish a correlated method, this initial study was instructive to determine directions of future correlated studies.

In the course of this work, the PL-TEM method was used to study many different NW heterostructures:

- WZ GaAs NWs with axial ZB GaAsSb inserts. Aim: to investigate the band alignment between the insert and the core, and influence of the structural defects in the core on the optical properties of the insert.
- WZ GaAs/GaAsSb core-shell NWs. Aim: to study novel WZ GaAsSb and to investigate the band alignment between the core and the shell, and whether there is inbuilt radial separation of electrons and holes.
- WZ GaAs inserts in WZ AlGaAs NWs with AlGaAs shells. Aim: to observe quantum confinement effect in WZ GaAs inserts grown for 30 s or shorter, and to compare to the bulk PL behaviour for longer inserts ($1-2$ min).
- ZB GaAs inserts in WZ GaAs NWs. Aim: to observe the expected type II transition between ZB and WZ GaAs [18, 41]. Growth optimisation of ZB/WZ GaAs interfaces.
- WZ GaAs/AlGaAs core-shell NWs. Aim: investigation of the fundamental optical properties of WZ GaAs.

The basic PL-TEM method provided some insight into optical property-structure relation for all these NW heterostructures. Moreover, the initial PL-TEM method became a sound basis for further development. To begin with, a couple of more advanced PL techniques were included (paper III). Fortunately, the TEM facilities available at TEM Gemini Centre, Phillips CM30 and Jeol 2010F, were suitable for investigation of fundamentally intriguing NW heterostructures with a simple design: WZ GaAs/AlGaAs core-shell NWs (paper III) and WZ GaAs/ZB GaAsSb axially heterostructured NWs (papers I, II, IV).

The WZ GaAs bandgap and conduction band symmetry have been a highly controversial topic during the last couple of years. Theoretical works predict values of 1.553 eV [42] and 1.504 eV [18] for the low temperature WZ GaAs bandgap versus 1.5194 eV in bulk ZB GaAs [17, 43]. Reported experimental results indicate higher [44, 45], lower [46] or approximately the same [47, 48] value as for ZB GaAs. The symmetry of the lowest conduction band of WZ GaAs has been uncertain: Γ_8, as proposed by De and Pryor [18], or Γ_7, as claimed by Ketterer et al. [48].

Fundamental optical properties of WZ GaAs were studied on carefully selected single NWs by several complementary micro-PL techniques: power-dependent, temperature-dependent, polarization-resolved and time-resolved;

and conventional TEM (paper III). In our work, the direct PL-TEM correlation was an advantage compared to the references [44–48]. Moreover, NWs with high purity of WZ phase are necessary for such study, with no SFs or low density of uncoupled SFs, and no ZB segments at all within them. In contrast to other reports on WZ GaAs bandgap where the study is based on GaAs NWs of a mixed WZ-ZB phase [41, 45, 48], we were able to find and study GaAs NWs with pure WZ phase. In this work, we present values for WZ GaAs low temperature free exciton emission and room temperature bandgap, and discuss the conduction band symmetry and the optical quality of Au-assisted WZ GaAs NWs.

Investigating the Sb concentration levels in ZB GaAsSb inserts within WZ GaAs NWs, is crucial for understanding the insert growth kinetics and to optimise the growth procedures in order to precisely control the Sb content and thus the insert's bandgap (paper IV). The structural and the optical properties of ZB GaAsSb inserts in GaAs NWs have been studied previously without direct correlation [19, 20, 49, 50]. Moreover, a novel quantitative HAADF STEM study of the Sb concentration within the ZB GaAsSb inserts has been reported recently [51]. However, there is no study reported that gathers and correlates all these aspects on a single NW level, and that is what we aimed to achieve.

By studying a substantial number of both bare-core and core-shell NWs by TEM-EDX, a clear trend between the Sb concentrations and the insert lengths emerged. Moreover, the Sb concentration variation was observed both along and across the inserts by quantitative HAADF STEM study. The Sb concentration gradient within and variation among the inserts were directly correlated with the ZB GaAsSb optical properties. In addition, the Sb concentration was calculated from the GaAsSb PL emission energy, for a large number of NWs studied by correlated PL-TEM, and compared to values obtained by EDX and quantitative HAADF STEM. This study provided a much more detailed insight into relation between the crystal structure, composition and the optical properties of the GaAsSb inserts than the initial works (paper I and II).

To summarize this introduction, a number of different correlated PL-TEM studies was carried out within this work and provided a detailed insight into the relation between the structural and optical properties of GaAs-based NWs. Moreover, the structural characterization by (S)TEM on its own resulted in a better understanding of how close the designed heterostructured NWs are to the experimentally observed NWs. This knowledge will be useful for further NW growth optimisation and design of new NW heterostructures for solar cell applications.

Chapter 2

Heterostuctured GaAs-based semiconductor NWs

The studied GaAs-based heterostructured NWs grown on GaAs (111)B substrates are described in detail in this chapter through: the Au-assisted MBE growth procedures (**2.1**), the commonly observed crystal phases and defects (**2.2**), NW morphology (**2.3**) and faceting (**2.4**). The main focus of this work, the correlated PL-TEM studies, and some examples of the studied NW heterostructures are discussed in the last part of this chapter (**2.5**).

2.1 MBE growth of Au-assisted GaAs-based NWs

The NW growth in MBE is governed by vapour-liquid-solid (VLS) mechanism where a liquid metal catalyst particle [52], usually gold, is needed for nucleation and growth of NWs. The growth procedure of Au-assisted bare-core GaAs NWs grown on GaAs (111)B substrates can be divided into several stages [23]:

1. GaAs substrate is deoxidized at 620°C and a ~ 100 nm thick buffer layer is grown by MBE to achieve a flat surface. The buffer layer can be pure GaAs [19,20] or GaAs/AlGaAs/GaAs, where AlGaAs serves as marker layer [49,53]. A thin Au film (< 1 nm) is deposited on such prepared GaAs (111)B substrate in the electron beam evaporator. Transferred back into the MBE, the substrate is heated up to temperatures suitable for NW growth ($540-550^{o}$C) under As_4 flux of 6×10^{-6} Torr, which induces the dissociation of Au film into particles. At this stage, the gold particles are alloyed with the substrate material. The liquid-alloy particles are effectively Au-Ga since the solubility of As in Au is very low [54]. This process results in random positions and sizes (30-100 nm) of the catalyst nanoparticles.

2. The NW growth is initiated by supplying Ga flux at substrate temperatures of $540 - 550^{o}$C. The source materials dissolve in the liquid-alloy particle until the composition reaches saturation. When the alloy particle becomes saturated with Ga and As while the gas supply continues, the excess material segregates below the particle in solid form. The VLS growth model explains that a seed particle favours to form at the triple-phase line [55]. The seed particle extends and grows into a monolayer (ML) below the alloy particle. The solid NW forms ML by ML, with the same diameter as the alloy particle. The NW growth direction is $[111]_{ZB}$ or $[0001]_{WZ}$, which represent the same direction but in the cubic and hexagonal lattice respectively. The Ga flux is such that the planar growth rate of GaAs is ~ 0.7 MLs^{-1} [19]. Under these growth conditions, predominantly WZ phase is obtained in GaAs NWs.

3. As the NW continues to grow, the Ga and As adatoms are supplied by direct impingement to the particle, by diffusion from the side walls and from the substrate, up the side walls towards the particle [56]. Since Ga and As adatoms fall onto the substrate, a two-dimensional (2D) GaAs layer forms on the substrate around the NWs at the same time as the NWs grow. The AlGaAs marker layer is useful to estimate the height of the 2D GaAs growth (~ 400 nm) by SEM [49,53]. The core is usually grown for $20-25$ min which results in $2 - 3\,\mu$m long NWs.

The VLS technique allows tailoring of NW composition both in axial and radial directions by adjusting the growth parameters. The growth parameters such as source fluxes, dimer species and substrate temperature affect the NW growth rate, NW sizes, morphology (for example tapering), composition and purity of the desired crystal phase [23]. By carefully tuning the growth parameters, it is possible to achieve a variety of axial and radial heterostructures by MBE growth, for example: WZ GaAs NWs with ZB GaAsSb or ZB GaAs inserts, WZ GaAs NWs with WZ AlGaAs or WZ GaAsSb shell, WZ AlGaAs NWs with WZ GaAs inserts. The basic growth procedures for a GaAsSb axial insert and an AlGaAs radial shell are described below.

Axial GaAsSb inserts in GaAs NWs are grown by introducing Sb flux at some point during NW growth without any growth interruption. The inserts are usually grown for about 30 s under Sb_2 flux of 6×10^{-7} Torr and at substrate temperatures of $540 - 580^{o}$C [20, 49].

To grow a radial AlGaAs shell, the substrate temperature is kept at $540-550^{o}$C [23]. The temperature of Al effusion cell is set to achieve nominal composition of $Al_{0.3}Ga_{0.7}As$ as for 2D growth on a GaAs (100) substrate. The shell growth is initiated by opening the Al shutter without growth

interruption. The As_2 flux is adjusted in such a way that V/III ratio remains constant. The shell is usually grown for 15 min and during that time an axial AlGaAs segment forms on top of the GaAs core as well [53, 57]. In addition, core-shell NWs need to be capped by a thin GaAs layer since AlGaAs oxidizes quickly. The GaAs cap is grown for 5 min under As_2 flux of $6-9\times10^{-6}$ Torr at $400-500^{o}$C, i.e. at the conditions which favour radial GaAs growth.

Introducing shells is important for enhancement of the optical properties since the shell passivates the interface states of the NW core [58,59]. AlGaAs shells are very desirable for bare-core GaAs NWs, because the wide bandgap allows carrier flow to lower bandgap core [17]. Another advantage of AlGaAs is that the lattice constants are almost the same as for GaAs [17]. Hence, no matter how high Al composition is, the strain between the core and the shell is elegantly avoided. The unintentionally grown axial AlGaAs segment, which has a contribution to the PL spectra of core-shell NWs [53], is a drawback for example for laser application and NW contacting, since it covers the NW core from above.

2.2 Crystal phases and defects

Bulk III-V semiconductor materials in most cases adopt ZB phase [17]. Both ZB and WZ phase are found in NW form of III-V compounds. WZ phase exists as well, for example in bulk form of III-nitrides and some II-VI compounds [60]. In contrast to bulk, polytypism (i.e. mixture of WZ and ZB phases and stacking irregularities) often occurs in NW form of III-V compounds [26, 41, 55].

Atomic arrangements of a III-V compound in ZB phase on a $\langle 1\bar{1}0\rangle_{ZB}$ zone, and in WZ phase on a $\langle 11\bar{2}0\rangle_{WZ}$ zone, are shown in figure 2.1(a,b). A common way to compare the atomic arrangements of ZB and WZ phases is to refer to their stacking sequences in $[111]_{ZB}$ and $[0001]_{WZ}$ direction respectively, indicated by the arrow in figure 2.1. The ZB stacking sequence is described as ABCABCABC, whereas WZ stacking sequence is ABABAB. Each letter (A, B, C) represents one bilayer consisting of a group III and a group V element which are bound to each other along $[111]_{ZB}$ or $[0001]_{WZ}$ direction.

The most common structural defect for III-V NWs in ZB phase is rotational twinning around a $\langle 111\rangle_{ZB}$ axis. As example, dark field (DF) TEM image of a twinned ZB GaAs insert in a WZ GaAs/AlGaAs core-shell NW is shown in figure 2.2(a). In general, twinning in a crystal means that the crystal is composed of parts that are oriented with respect to one another

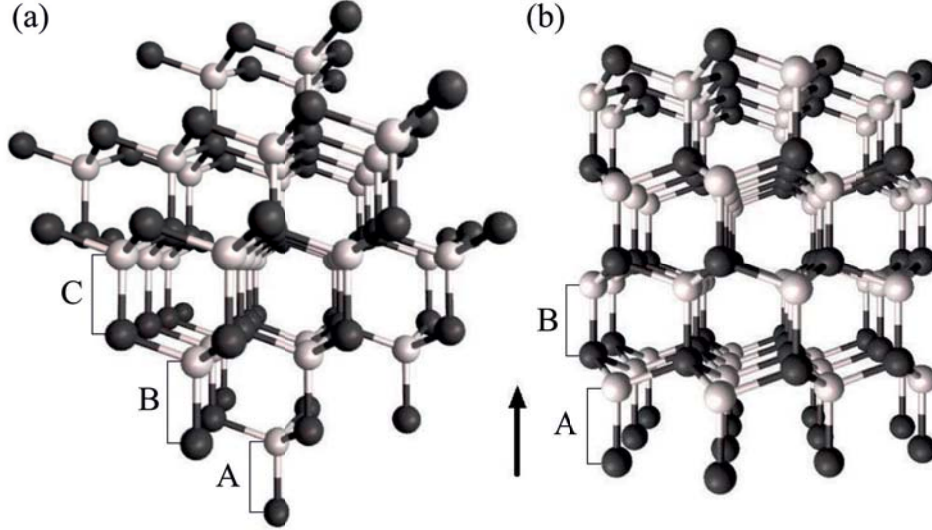

Figure 2.1: Stacking sequence for a III-V compound in (a) ZB phase on a $\langle 1\bar{1}0\rangle_{\mathrm{ZB}}$ zone, and (b) WZ phase on a $\langle 11\bar{2}0\rangle_{\mathrm{WZ}}$ zone, made in JEMS software [61]. The NW growth direction, $[111]_{\mathrm{ZB}}$ or $[0001]_{\mathrm{WZ}}$, is indicated by the arrow. A, B, C are bilayers of group III element (black) and group V element (white).

according to some symmetry rule [62]. In case of a ZB NW, twinning means that two ZB segments are rotated with respect to each other for 60° around a $\langle 111\rangle_{\mathrm{ZB}}$ axis, which changes the stacking sequence from ABC to CBA. This rotation occurs around the growth direction in most cases, see figure 2.2(a), but can occur in another $\langle 111\rangle_{\mathrm{ZB}}$ direction.

Stacking sequence for twinned ZB is ABCAB$\underline{\mathrm{C}}$BACBA, where the plane which lies between group III and group V atoms within the bilayer $\underline{\mathrm{C}}$, represents the twin boundary. Note that the twin boundary is not a mirror plane, because the bonding orientation between group III and V atoms is not mirrored across the boundary. In other words, only the stacking sequence is mirrored and the bonding occurs between group III and V atoms across the twin boundary. The bilayer $\underline{\mathrm{C}}$, at the twin boundary, could be considered to be in WZ-like surrounding (...B$\underline{\mathrm{C}}$B...). However, B$\underline{\mathrm{C}}$B is not a WZ segment. There is a clear distinction between the twin interface and a WZ segment in ZB phase. The smallest segment of WZ phase within ZB phase consists of four bilayers and occurs when two consecutive bilayers are misplaced (i.e. two consecutive twin boundaries): ABCA(BC$\underline{\mathrm{BC}}$)ABC, where the bilayers within the brackets have WZ atomic arrangement [26].

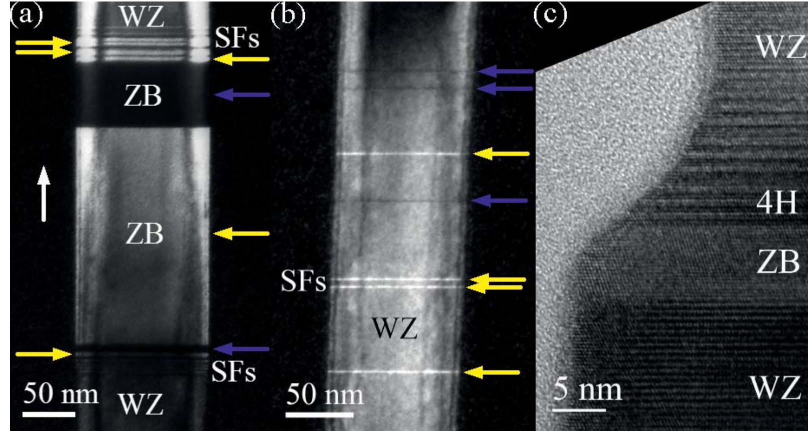

Figure 2.2: (a) DF TEM image of a twinned ZB GaAs insert in a WZ GaAs/AlGaAs core-shell NW. The growth direction for all three NWs is indicated by the white arrow. (b) DF TEM image of a WZ AlGaAs NW with SFs. The yellow and blue arrows in (a) and (b) point at rotationally twinned ZB segments or SFs of different orientations. (c) High resolution (HR) TEM image of a tip of a WZ GaAs/AlGaAs/GaAs core-shell-cap NW with variation of crystal phase: WZ, ZB, 4H and WZ.

In WZ phase, SFs are the most common structural defect. An example of a WZ AlGaAs NW with SFs is shown in figure 2.2(b). A SF is defined as a single additional layer (extrinsic SF) or a single missing layer (intrinsic SF) in an otherwise perfect crystal [62]. WZ stacking sequence with a single SF is ABAB$\underline{\text{ABC}}$ABAB or ABAB$\underline{\text{ABC}}$BCBC where the bilayers $\underline{\text{ABC}}$ are arranged as in ZB phase. This represents the smallest unit of ZB stacking sequence (0.979 nm long). Another possibility for occurrence of a single SF is sequence ABA$\underline{\text{BAC}}$BABA or ABA$\underline{\text{BAC}}$ACAC. These two ZB unit sequences, ABC and BAC have different orientation, i.e. are rotated with respect to each other for 60° around the $[0001]_{\text{WZ}}$ axis. These are effectively twinned ZB units, which results in their reflections being mirrored with respect to $\langle 0001 \rangle_{\text{WZ}}$ direction in the diffraction pattern (DP). Therefore these two SFs would appear bright and dark in a DF TEM image formed by a reflection characteristic for one of the SFs, see for example figure 2.2(b). SFs can be extended into more than three bilayers of ZB stacking sequence, for example: AB$\underline{\text{ABCA}}$BA or AB$\underline{\text{ABCA}}$CA (4/3 ZB unit), AB$\underline{\text{ABCAB}}$AB (5/3 ZB unit), AB$\underline{\text{ABCABC}}$AB (two ZB units). A ZB stacking sequence larger than two ZB unit sequences can be considered as a ZB segment within WZ phase.

4H polytype with stacking sequence ABACABAC, is another phase which can be found in III-V NWs [20, 63, 64]. For example, 4H polytype segment is observed in WZ GaAs NWs with axial ZB GaAsSb inserts, directly after the insert before WZ GaAs continues [20], or in the tappered tip of a WZ GaAs/AlGaAs/GaAs core-shell-cap NW, shown in figure 2.2(c), where a mixture of WZ, ZB and 4H phases occurs.

2.3 NW morphology

The most common types of NW morphology observed in GaAs-based NWs throughout this work, are presented in figure 2.3. The bare-core NWs usually have constant, or nearly constant, diameter along the whole length, as shown in figures 2.3(a,b). For some bare-core NWs, tapering close to the droplet may occur (figure 2.3(b)) [23]. The core-shell(-cap) NWs are in most cases pencil-shaped (figure 2.3(c)), i.e. anti-tapered up to the tapered tip region. The anti-tapering could be due to a high density of the NWs on the substrate and shadowing effect during the NW growth in MBE [23, 53]. A special case of a core-shell(-cap) NW with a pronounced anti-tapered axial AlGaAs segment and an elongated tapered tip is shown in figure 2.3(d). Similar morphology has been reported previously [31, 32] and this type of morphology is further discussed in chapter **2.4**.

An interesting feature of the NWs with AlGaAs shell and GaAs cap are the characteristically tapered tips, as can be seen in figures 2.3(c,d). For example, this occurs in WZ GaAs/AlGaAs/GaAs core-shell-cap NWs and WZ AlGaAs NWs capped with GaAs. As example, DF TEM and HAADF STEM images of a tapered tip belonging to a WZ AlGaAs NW with a WZ GaAs insert and GaAs cap, are shown in figure 2.4. A mixture of crystal phases and defects (WZ, SFs, ZB, 4H) occurs within the tapered NW tips (figure 2.2(c)). Small ZB segments commonly appear at the step of diameter decrease in the tip (figures 2.2(c) and 2.4(a)).

A brighter region is usually observed by HAADF STEM in the evenly thick region just below the tapered tip (figure 2.4(b)). The HAADF STEM intensity appears to be higher towards the NW wedges in figure 2.4(c), suggesting that GaAs is building up onto the axial AlGaAs segment in this region during the GaAs cap growth. Moreover, the intensity profile in figure 2.4(d) indicates a local increase of the average atomic number, and possible segregation of GaAs at the beginning of the tip. Thus, a question for further correlated PL-TEM studies emerged: if the tip region is pure GaAs, would it contribute to the GaAs related PL emission from other heterostructure elements (GaAs core or a GaAs insert)?

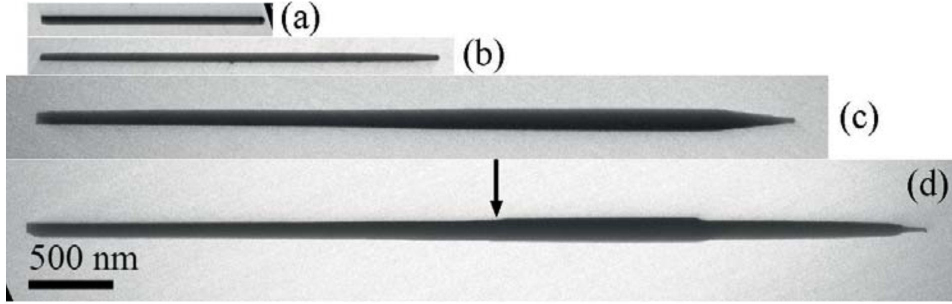

Figure 2.3: 30 kV bright field (BF) STEM images of a bare-core WZ GaAs NW (a) with a constant diameter and (b) slightly tapered towards the tip, and anti-tapered WZ GaAs/AlGaAs/GaAs core-shell-cap NW (c) without and (d) with outer facet rotation. The arrow in (d) marks the position of where facet rotation occurs and the axial AlGaAs segment starts. The scale bar is the same for all four images.

2.4 NW faceting

As reported previously, GaAs-based NWs grown in $[0001]_{WZ}$ (or $[111]_{ZB}$) direction by Au-assisted MBE have hexagonal cross section with $\{1\bar{1}0\}_{ZB}$ or equivalent $\{11\bar{2}0\}_{WZ}$ facets [19, 23]. In the course of this work, this was confirmed in most cases of the studied NWs (figures 2.3(a,b,c)). However, different families of facets for different axial segments along a NW, were observed for one particular morphology of WZ GaAs/AlGaAs core-shell NWs, i.e. very long NWs ($\sim 5\,\mu$m) with a pronounced axial AlGaAs segment (see for example figure 2.3(d)). For example, similar facet rotation has been reported for tapered WZ GaAs NWs [30] and recently for InAs/InAsSb axial NW heterostructures [31].

One approach to study the outer facets of core-shell NWs is to use complementary TEM/STEM techniques. By comparing DF TEM and HAADF STEM image intensities of a whole (as-dispersed) NW, it is possible to deduce the faceting of the NW all along its length. A limitation of this approach is that the core-shell interfaces cannot be determined.

A NW of interest, which exhibits transition from $\{1\bar{1}00\}_{WZ}$ to $\{11\bar{2}0\}_{WZ}$ facets along its length, is shown in figure 2.5. The NW ($4.4\,\mu$m long) has pure WZ phase (see DP in figure 2.5(b)) for about $2.9\,\mu$m with only one SF at the very bottom. There is step-wise increase of the NW diameter, shown in figure 2.5(c). The transition from the core-shell structure to the axial AlGaAs segment occurs about the region marked by the red arrows in figure 2.5(a). This was indicated by EDX line scans across the NW at

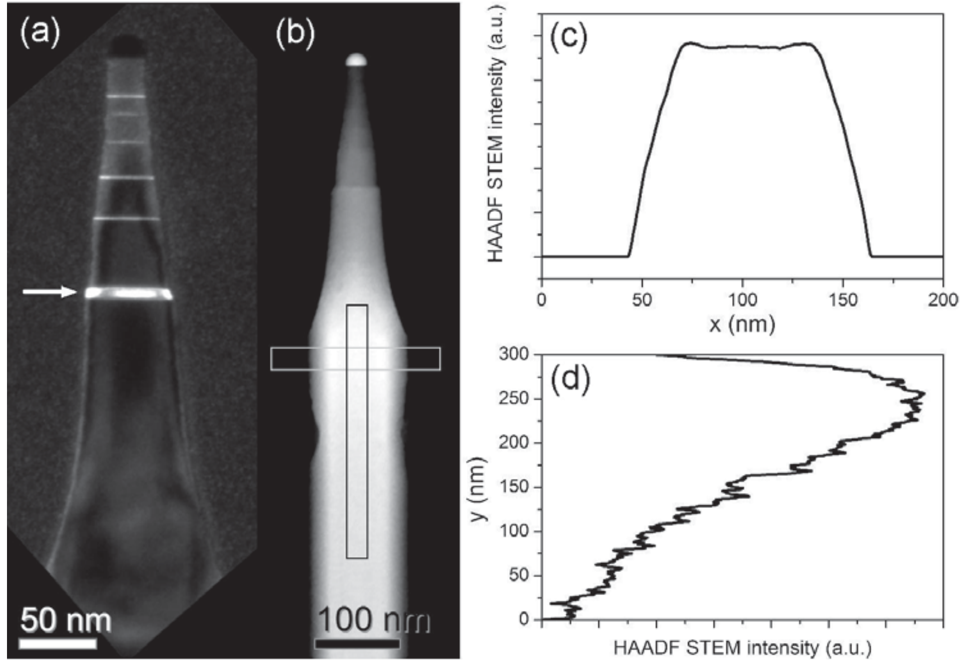

Figure 2.4: The tapered tip in a WZ AlGaAs NW with a WZ GaAs insert and GaAs cap: (a) DF TEM image, WZ phase with a ZB segment (marked by white arrow) and some SFs. (b) HAADF STEM image. The boxes mark the regions where the intensity profiles are taken from. HAADF STEM intensity profile (c) across and (d) along the evenly thick region just below the tip.

several positions along the NW (not shown). The first SFs appear within the axial AlGaAs segment (marked by the black arrow in figure 2.5(a)), and are followed by bands of SFs and a twinned ZB region (see DP in figure 2.5(d)). The crystal phase changes from twinned ZB back to WZ with SFs within the tip region.

A comparison between HAADF STEM and DF TEM images and their intensity profiles at the bottom part of the NW is shown in figure 2.6. The HAADF STEM intensity profiles depend on thickness across the NW and its composition (figure 2.6(c)). Thickness fringes in DF TEM image are symmetrical with respect to the NW axis and the intensity oscillates across the whole diameter (figure 2.6(d)). Note that the fringes are reversing contrast and that the number of fringes is changing along the NW. This depends on the NW thickness (increasing, i.e. NW is anti-tapering) and orientation with respect to the electron beam (chapter **3.1.3**). Namely, different parts

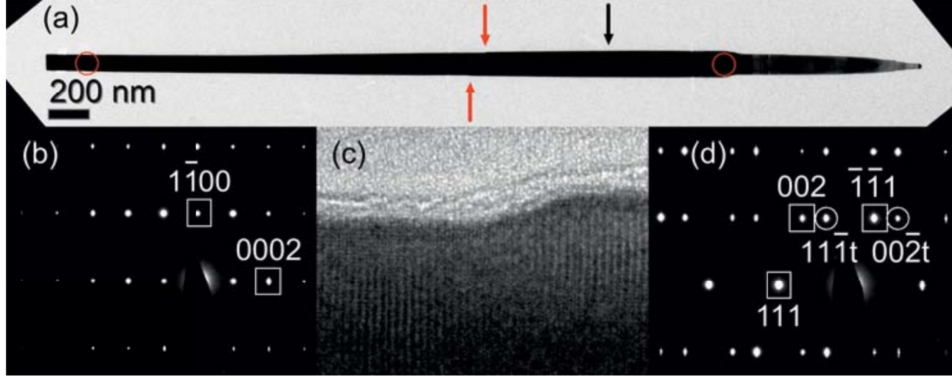

Figure 2.5: (a) Overview BF TEM image of a WZ GaAs/AlGaAs core-shell NW. The red arrows point at the step-wise increase of the diameter and transition region from the core-shell to the axial AlGaAs segment. The black arrow marks where the SFs start in the axial AlGaAs segment. The red circles indicate regions where the DPs is (b) and (d) are taken from. (b) DP from the bottom part of the NW, showing WZ phase. (c) HRTEM showing the diameter increase at the region marked by the red arrows in (a). (d) DP from the top part of the NW, showing twinned ZB phase.

of the NW have varying deviation parameters for the two reflections ((000$\bar{2}$) and (000$\bar{3}$)) included in the DF TEM image, due to slight NW bending. DF TEM thickness fringes also indicate that there is no even thickness across the NW. Given that the NW was oriented onto a $\langle 11\bar{2}0\rangle$ zone, HAADF STEM and DF TEM intensity profiles together indicate $\{1\bar{1}00\}$ outer facets in the bottom part of the NW. The $\{1\bar{1}00\}$ facet family is equivalent to $\{11\bar{2}\}$ in ZB phase, and rotated for 30° around the NW axis with respect to $\{11\bar{2}0\}$ facets.

DF TEM image and the intensity profiles of the middle part of the NW are shown in figure 2.7. Profiles (1-4) exhibit symmetric contrast reversals all across the NW diameter, which indicate $\{1\bar{1}00\}$ facets (as in figures 2.6 (b,d)). Profile 5, taken from the region between the two red arrows, contains in addition $20-30$ nm of flat intensity region in the centre in contrast to profiles (1-4). The central flat region in profile 6, approximately half of NW diameter wide, and symmetric contrast reversals only outside this region, indicate $\{11\bar{2}0\}$ facets. Therefore, the step-wise increase of the diameter (figure 2.5(c)) is located exactly where the transition from $\{1\bar{1}00\}$ to $\{11\bar{2}0\}$ facets occurs.

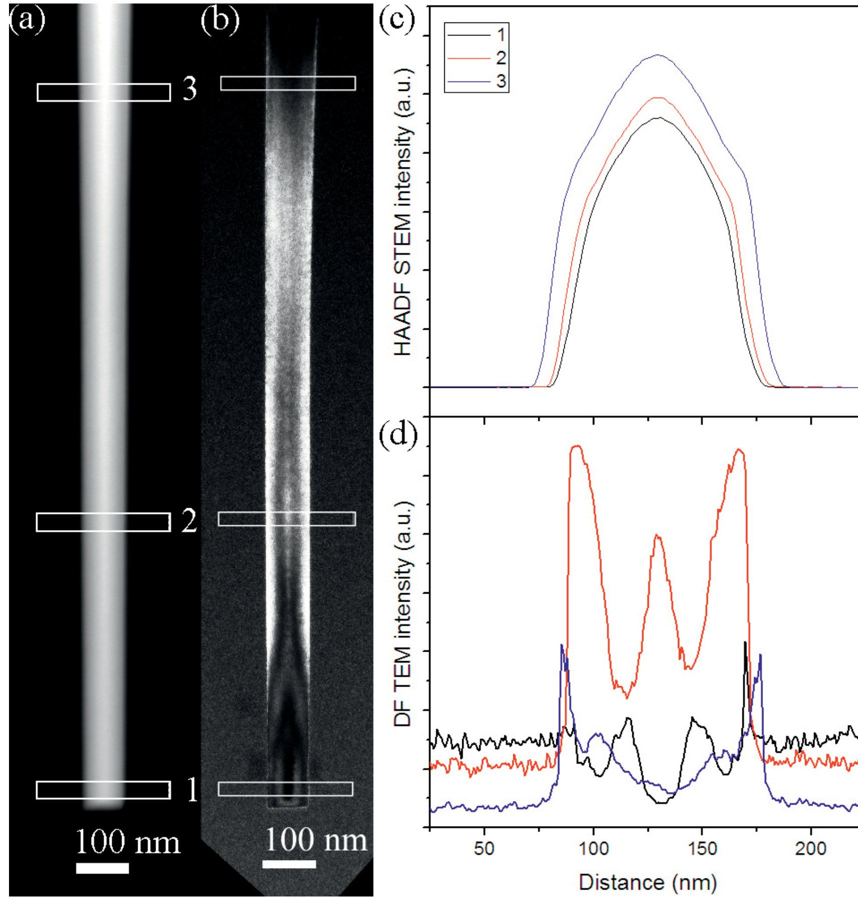

Figure 2.6: WZ GaAs/AlGaAs core-shell part of the NW (bottom): (a) HAADF STEM image and (b) DF TEM image taken from $(000\bar{2})$ and $(000\bar{3})$ reflections. (c) HAADF STEM and (d) DF TEM intensity profiles across the NW taken from the regions (1, 2, 3) in (a) and (b) respectively.

To conclude, the core-shell part of the NW has $\{1\bar{1}00\}$ facets, whereas the axial AlGaAs segment adopts the default $\{11\bar{2}0\}$ facets. These preliminary results demonstrate that the contrast in conventional TEM images holds valuable information and should be explored further, for example with image simulations. This simple approach enables quick assessment of the structural quality and outer facets of NWs. Recognizing morphology and facets is useful for pre-selection of NWs for a PL study as well as for the growth optimisation.

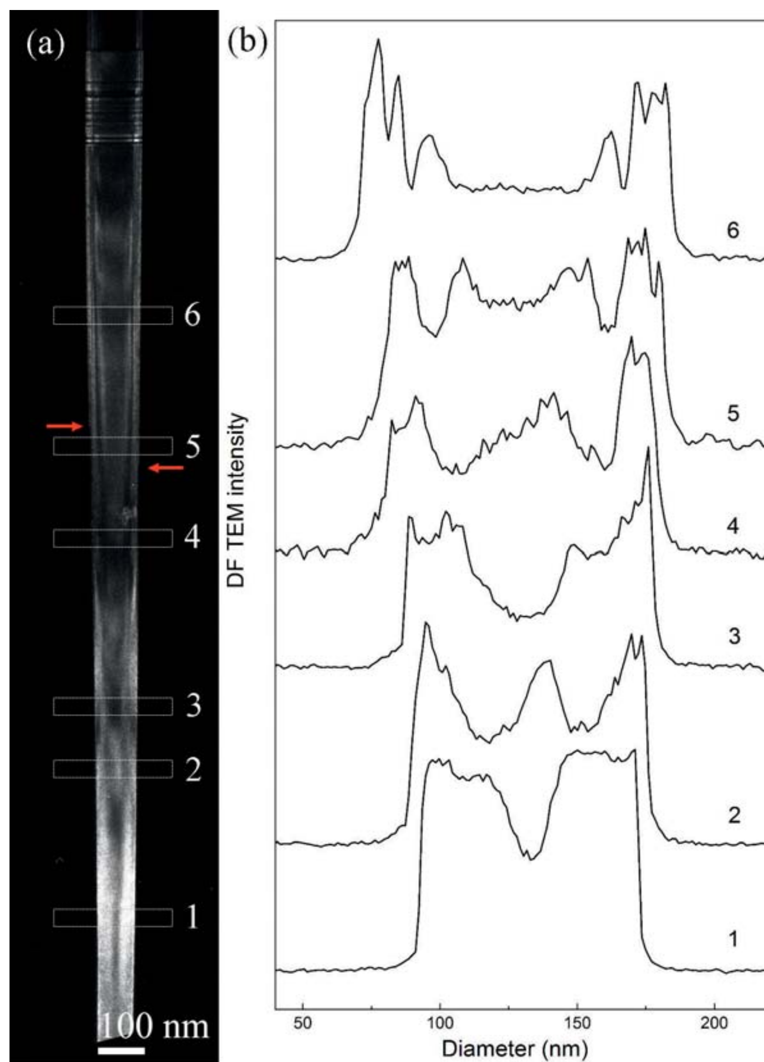

Figure 2.7: (a) DF TEM image of the NW middle. The red arrows mark the step-wise increase of the diameter. (b) DF TEM intensity profiles from the regions (1-6) in (a). Profiles (1-4) reveal $\{1\bar{1}00\}$ facets, profile 5 is located at the transition region, profile 6 reveals $\{11\bar{2}0\}$ facets.

2.5 Heterostructured NWs studied by correlated PL-TEM

The first and the crucial part of this work was development of the correlated PL-TEM method (paper I). This development led to routine correlated studies of different axial and radial GaAs-based heterostructured NWs. To achieve a better understanding of the correlation between the optical and the structural properties, many NWs need to be studied for each selected NW heterostructure and different PL and (S)TEM techniques need to be employed. This implies that correlated PL-TEM studies are very time-consuming.

WZ GaAs/ZB GaAsSb(insert) NWs, with or without the AlGaAs shells, were studied in papers I, II and IV. At first, the aim was to investigate how the optical properties of the ZB GaAsSb inserts depend on the neighbouring defects within the WZ GaAs core (papers I and II). Next, the Sb concentration variation among and within the GaAsSb inserts was observed, studied in more detail and related to the optical properties (paper IV).

WZ GaAs/AlGaAs core-shell NWs were thoroughly studied in paper III. The motivation was to determine the low temperature free exciton energy, room temperature bandgap and the lowest conduction band symmetry of WZ GaAs. Understanding the optical selection rules for ZB and WZ GaAs is important in a broader context of all NWs studied here, which are GaAs-based. The optical selection rules and an example of a WZ GaAs/AlGaAs core-shell NW with a high density of SFs are presented in chapter **2.5.1**.

Due to complexity of the heterostructured NWs or a need for further growth optimisation, some of the PL-TEM studies remained inconclusive in the course of this work, but may become subject of a future work. Examples of such studies are WZ GaAs/GaAsSb core-shell NWs, ZB GaAs inserts in WZ GaAs NWs, and WZ GaAs inserts in WZ AlGaAs NWs with AlGaAs shells. The last NW heterostructure is especially interesting given the growing interest in quantum dots within NWs, and some preliminary results are presented in chapter **2.5.2**.

2.5.1 WZ GaAs/AlGaAs core-shell NWs

Search for the NWs that exhibited the desired WZ GaAs PL behaviour was a large part of this correlated study. Preselection of single NWs was performed by 30 kV BF STEM. Subsequent selection of optically desired NWs by PL was based on the optical selection rules. Afterwards, the PL judgement of WZ phase purity was verified by TEM.

For ZB GaAs, the optical transitions are unpolarized according to the selection rules [18,42]. However, due to the dielectric contrast effect [65], ZB GaAs PL emission is polarized parallel to the NW axis. For WZ GaAs, the optical selection rules can be derived by combining the approaches described by Dresselhaus [66] and Birman [67]. Double group representation of the WZ point group C_{6v} needs to be used when the spin-orbit coupling is included [67]. Hence, the possible symmetries of the conduction and valence band states at the centre of the Brillouin zone in WZ GaAs are Γ_7, Γ_8 and Γ_9. The optical transitions from the highest valence band state Γ_9 (heavy hole) to the two lowest conduction band states, Γ_7 and Γ_8 [18], are orthogonally polarized with respect to the NW axis ($[0001]_{\mathrm{WZ}}$).

In case of a GaAs NW with mixed WZ and ZB phases (i.e. with high density of SFs and/or ZB segments), there is possibility for several different PL transitions which may be differently polarized. Namely, the band alignment between WZ and ZB GaAs is considered to be type II, with electrons in ZB conduction band and holes in WZ valence band [18, 41]. Moreover, quantum confinement can occur in SFs and small ZB or WZ segments, making the possible PL transition routes even more complex. Thus, the question is whether one GaAs peak, orthogonally polarized with respect to the NW axis, or several GaAs peaks of different polarizations, are detected by polarization-resolved PL.

An example of an undesired WZ GaAs/AlGaAs core-shell NW is shown in figure 2.8. This NW has a high density of SFs in the bottom (figure 2.8(b)) core-shell part for about $1.3\,\mu$m (up til arrow 1 in figure 2.8(a)). The SF density gradually decreases between arrows 1 and 2, and above the arrow 2 the structure becomes WZ with few SFs. It is not clear from HAADF STEM where the axial AlGaAs segment starts.

Low temperature polarization-resolved PL spectrum in figure 2.8(c) contains two peaks at 1.513 eV (weak) and 1.517 ± 0.001 eV (strong), which are differently polarized. The polarization of the weak lower energy peak is at 10° with respect to the NW axis (figure 2.8(d)), whereas the strong higher energy peak is polarized at 65° (figure 2.8(e)). Both peaks differ from parallel or perpendicular polarization which is expected for ZB or WZ GaAs respectively. This is a good example of how a mixture of WZ and ZB crystal phases in a GaAs NW results in complex polarized-PL properties. It is illustrative to compare this NW with the pure WZ one presented in paper III.

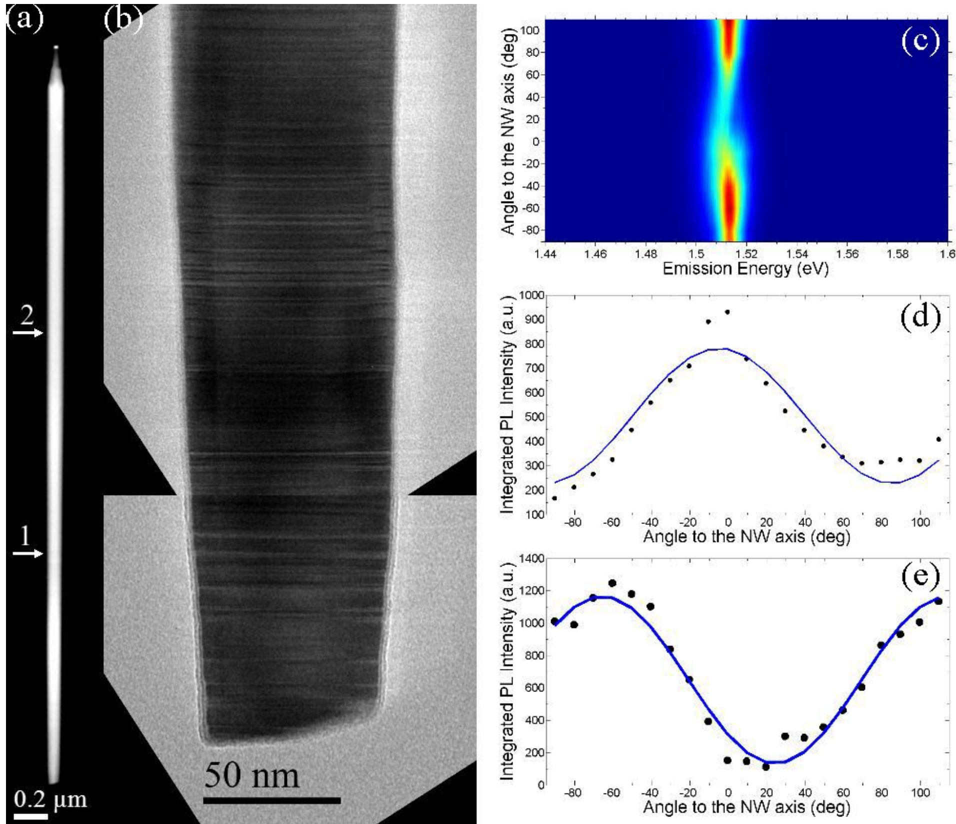

Figure 2.8: (a) Overview HAADF STEM image of a WZ GaAs/AlGaAs core-shell NW ($4.2\,\mu$m long). There is a high density of SFs below arrow 1, the SF density decreases between arrows 1 and 2, and above arrow 2 the structure is WZ with few SFs. (b) HRTEM image of the bottom part ot the NW. (c) Polarization-resolved PL spectrum at 12 K. Two PL peaks at 1.513 eV (weak) and 1.517 ± 0.001 eV (strong) are distinguished. Integrated PL intensity as a function of angle to the NW axis for (d) lower and (e) higher energy PL peak. The PL was measured by L. Ahtapodov.

2.5.2 WZ GaAs inserts in WZ AlGaAs NWs

Investigation of the optical properties of quantum confined WZ GaAs within a larger bandgap material, in this case AlGaAs, was the motivation for this study. Several batches of WZ AlGaAs NWs with WZ GaAs inserts of different lengths (growth time 30, 60 and 120 s) were grown to compare the quantum confined and bulk PL behaviour. These NWs also had an axial AlGaAs segment above the GaAs insert, a radial AlGaAs shell and a GaAs cap.

The MBE growth of small GaAs segments in NWs is a challenge on its own. Pure WZ structure within the GaAs insert is desired, which is difficult to achieve due to random appearance of SFs. The growth time needs to be short (< 10 s) to obtain a quantum confined insert (length $\lesssim 10$ nm). However, for such a short growth time the AlGaAs/GaAs interfaces may not be sharp. Namely, some Al remains dissolved in the alloy particle after the Al flux is shut off, and it takes some time to reach equilibrium Al concentration in the droplet after the GaAs insert growth [68]. Therefore, longer inserts (1 and 2 min), where no quantum confinement is expected, were grown to assess the quality of the growth by PL-TEM.

The majority of the PL spectra contained broad GaAs related PL emission, characteristic for bulk GaAs, which indicated the presence of a long GaAs insert. For some NWs with 1 min GaAs insert, GaAs PL emission was complex and consisted of several or many well defined peaks.

Observing WZ GaAs inserts by HAADF STEM proved to be a rather difficult task. Moreover, the spatial resolution and sensitivity of the EDX system in Jeol 2010F was not sufficient to distinguish a GaAs insert in AlGaAs. Out of about 40 NWs with 1 min or 2 min inserts, only a couple of NWs had a distinguishable bright central region somewhere along their axis. This can occur due to locally higher average atomic number, and may indicate the presence of a GaAs insert.

An example of a NW with a visible 1 min GaAs insert and sharper PL peaks is shown in figure 2.9. The brighter region in the NW core, extends over ~ 350 nm along the NW axis (figure 2.9(a)), which is much longer than the expected length of a 1 min insert. There are SFs all along the NW length, and a small ZB segment within the tapered tip.

The broad PL emission starting at ~ 1.65 eV (figure 2.9(b)) is related to AlGaAs [53]. The WZ GaAs PL emission is starting at ~ 1.54 eV at the lowest excitation power, which is higher than the expected WZ GaAs free exciton energy [47, 48]. Moreover, as the excitation power increases, several excited states appear. This may indicate the presence of a quantum confined insert within the NW. An interesting observation is that there is

a redshift of GaAs related PL peaks with increase of the excitation power. This redshift was observed for other NWs with WZ GaAs inserts as well, and needs further investigation in future work.

To study quantum confined WZ GaAs inserts in MBE grown WZ AlGaAs NWs, a better growth control of the insert size and interface sharpness is needed first. On the characterization side, combining advanced PL techniques, for example polarization and time-resolved PL, and (S)TEM techniques that can visualize the compositional difference with sufficient spatial resolution, would be an useful approach to study such quantum confined inserts.

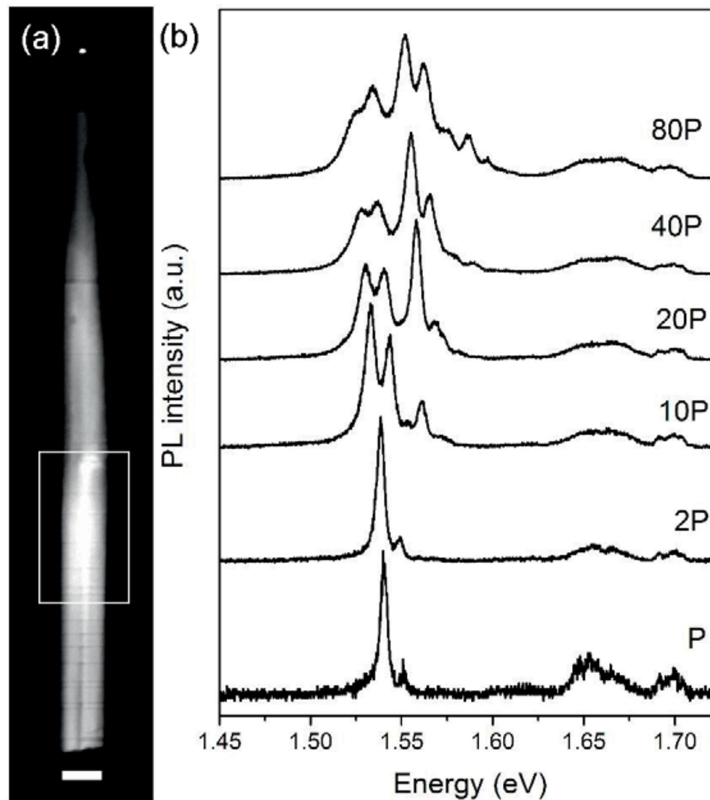

Figure 2.9: (a) Overview HAADF STEM image of a WZ AlGaAs NW (1.75 μm long) with a 1 min WZ GaAs insert. The white box surrounds the brighter region in the image. The scale bar is 100 nm. (b) Low temperature power-dependent PL spectra, where $P = 28$ W/cm^2. The PL was measured by A. F. Moses.

Chapter 3

Theoretical background

3.1 Theory of electron diffraction

In order to interpret TEM images and DPs in detail, a thorough understanding of the factors which determine the intensities and directions of diffracted beams is necessary. The electrons accelerated in a TEM (> 100 kV) are relativistic particles with a wavelength of:

$$\lambda = \frac{h}{\sqrt{2meE(1 + \frac{eE}{2mc^2})}} \quad (3.1)$$

where m is electron rest mass and E the accelerating voltage. The relativistic nature of electrons leads into relativistic quantum mechanics if we want to describe the interaction between the electrons and a crystalline material accurately. However, the problem can be simplified immensely by considering certain approximations.

This chapter approaches the theory of electron diffraction starting from the scattering by single atoms, and extends into scattering by crystals. The scattering is treated as elastic. Kinematical theory assumes single scattering event per electron, whereas dynamical theory deals with multiple scattering within the crystal. The crystal thickness and deviation from the diffraction condition determine whether kinematical or dynamical approach is suitable. Diffracted intensities as a function of crystal thickness and deviation from diffraction condition are derived. The extinction distance emerges as an important parameter that influences the image contrast.

3.1.1 Scattering of electrons from a single atom

First we consider how a fast, but non-relativistic, electron interacts with a single atom. The scattering process is considered to be elastic, meaning that it does not change the state of the atom. This case is well-described by the time independent Schrödinger equation [69, 70]:

$$-\frac{h^2}{8\pi^2 m}\bigtriangledown^2 \psi(\vec{r}) - eV(\vec{r})\psi(\vec{r}) = eE\psi(\vec{r}) \tag{3.2}$$

where $V(\vec{r}) > 0$ is the atomic potential. The general solution of the equation (3.2) is a linear combination of the incident and the scattered electron wave function. The incident electron wave function is a plane wave $e^{i\vec{k}\vec{r}}$, where $\vec{k}$ is the incident electron wave vector, $|\vec{k}| = \frac{2\pi}{\lambda}$, and λ is the non-relativistic electron wavelength:

$$\lambda = \frac{h}{\sqrt{2meE}}. \tag{3.3}$$

If the scattering is weak, i.e. $V(\vec{r}) \ll E$, the scattered wave amplitude is much weaker than the incident wave amplitude. This means that the first Born approximation can be applied to the general solution of the Schrödinger equation (3.2). Thus, the scattered electron wave function [69] obtains the form:

$$\psi_s(\vec{r}) = \frac{2\pi me}{h^2}\int_{\text{atom}} V(\vec{r'})\frac{e^{ik|\vec{r}-\vec{r'}|}}{|\vec{r}-\vec{r'}|}e^{i\vec{k}\vec{r'}}d\vec{r'} \tag{3.4}$$

where the total wave function $\psi(\vec{r'})$ in the integral has been replaced by the incident plane wave $e^{i\vec{k}\vec{r'}}$ under the first Born approximation. In addition, the scattered wave function is observed at a distance much larger than the dimensions of the atom: $|\vec{r}-\vec{r'}| \gg |\vec{r'}|$. By applying this approximation to the equation (3.4), the scattered wave function reduces to:

$$\psi_s(r) = f^{\text{B}}(\vec{K'})\frac{e^{ikr}}{r} \tag{3.5}$$

$$f^{\text{B}}(\vec{K'}) = \frac{2\pi me}{h^2}\int_{\text{atom}} V(\vec{r})e^{-i\vec{K'}\vec{r}}d\vec{r} \tag{3.6}$$

where $\vec{K'} = \vec{k'} - \vec{k}$ is the scattering vector, and $\vec{k}$ and $\vec{k'}$ are the incident and the scattered wave vector, respectively. For elastic scattering $|\vec{k}| = |\vec{k'}|$ and thus $K' = \frac{4\pi\sin\theta}{\lambda}$, where 2θ is the scattering angle. The quantity $f^{\text{B}}(\vec{K'})$ is the atomic scattering amplitude in the first Born approximation. We see that the atomic scattering amplitude is proportional to the Fourier transform of

the potential. For analogy, in X-ray diffraction, the atomic scattering (form) factor is equal to the Fourier transform of the electron charge density. The potential and the total (atomic) charge density are connected through the following relation:

$$V(\vec{r}) = \int_{\text{atom}} \frac{\rho(\vec{r'})d\vec{r'}}{|\vec{r}-\vec{r'}|} \tag{3.7}$$

where $\rho(\vec{r}) = eZ\delta(\vec{r}) - e\rho_e(\vec{r})$ contains nucleus and electron charge density. Hence the atomic scattering amplitude becomes:

$$f^{\mathrm{B}}(\vec{K'}) = \frac{2\pi me^2}{h^2} \iint_{\text{atom}} (Z\delta(\vec{r'}) - \rho_e(\vec{r'}))e^{-i\vec{K'}\vec{r'}}d\vec{r'}\frac{e^{-\vec{K'}(\vec{r}-\vec{r'})}}{|\vec{r}-\vec{r'}|}d\vec{r}. \tag{3.8}$$

The first integral in equation (3.8) yields $Z - f^{\mathrm{X}}(\vec{K'})$ where f^{X} is the atomic scattering factor for X-rays. The second integral in equation (3.8) is equal to $4\pi/K'^2$. Finally, we obtain the atomic scattering amplitude [69] as a function of the scattering angle 2θ:

$$f^{\mathrm{B}}(\theta) = \frac{me^2}{2h^2}(\frac{\lambda}{\sin\theta})^2(Z - f^{\mathrm{X}}(\theta)) \tag{3.9}$$

where the first term in the last bracket is due to Rutherford scattering from the nucleus and the second term is due to scattering from the electron charge density. The factor $(\sin\theta)^{-2}$ implies that $f^{\mathrm{B}}(\theta)$ is sharply peaked in the forward direction (it decreases rapidly with increasing angle). In the theory of electron scattering from a crystal (chapter **3.1.2**), it will be more useful to express the atomic scattering amplitude as a function of the scattering vector, since it belongs to the reciprocal space. Note that for a relativistic electron, $f^{\mathrm{B}}(\theta)$ can be corrected in a simple way by replacing the electron rest mass and the wave length by their relativistic analogues.

3.1.2 Kinematical theory of electron diffraction

Now let us consider scattering of electrons from a perfect crystal. Electrons experience the total crystal potential, which is in principle, a complex quantity including terms responsible for diffraction, refraction and absorption. Here, we deal only with the elastic scattering which is due to the periodic crystal potential. Thus, the diffraction is due to the interaction between the incident electron beam and the total charge distribution in the crystal. The underlying assumption in the kinematical theory of electron diffraction is that the scattering within the crystal is weak. This means that each incident electron is considered to be elastically scattered by the crystal only once.

The problem is described by the time independent Schrödinger equation (3.2) as well, with the periodic potential in this case. The periodic potential is defined as $V(\vec{r}) = V(\vec{r} + \vec{r}_n)$ [71], where $\vec{r}_n = u_n\vec{a}_1 + v_n\vec{a}_2 + w_n\vec{a}_3$ is the lattice vector at the unit cell n, and $\vec{a}_i$, $i = 1, 2, 3$ are the primitive vectors of the Bravais lattice which describes the underlying crystal symmetry. The reciprocal lattice of this Bravais lattice, is defined by the primitive vectors:

$$\vec{b}_i = 2\pi \frac{\varepsilon_{ijk}\vec{a}_j \times \vec{a}_k}{\vec{a}_1 \cdot (\vec{a}_2 \times \vec{a}_3)} \tag{3.10}$$

and a reciprocal lattice vector is expressed as $\vec{g} = h\vec{b}_1 + k\vec{b}_2 + l\vec{b}_3$.

The periodic potential can be expanded into a Fourier series [70, 71]:

$$V(\vec{r}) = \sum_{\vec{g}} V_{\vec{g}}\, e^{i\vec{g}\vec{r}}. \tag{3.11}$$

The Fourier coefficients of the periodic potential are:

$$V_{\vec{g}} = \frac{1}{V_{\text{cell}}} \int_{\text{cell}} V(\vec{r}) e^{-i\vec{g}\vec{r}} d\vec{r} \tag{3.12}$$

where integration goes over the unit cell and V_{cell} is the unit cell volume. The solution of the Schrödinger equation describing the interaction between the incident electrons and the crystal, i.e. the wave function scattered by the unit cell, takes the same form as in equation (3.5) since single scattering event per electron is assumed. The structure factor of the unit cell [69] is obtained in this case, instead of the atomic scattering amplitude. The structure factor of the unit cell is defined as:

$$F_{\vec{g}} = \sum_i f_i(\vec{g}) e^{-i\vec{g}\vec{r}_i} \tag{3.13}$$

where summation goes over all atoms in the unit cell and f_i, the atomic scattering amplitude (equation (3.6)) for the atom i, is expressed as a function of the reciprocal lattice vector. Here $\vec{r}_i = u_i\vec{a}_1 + v_i\vec{a}_2 + w_i\vec{a}_3$ represents the position of the atom i within the unit cell. The same expression (equation 3.13) for the structure factor is valid for X-ray diffraction, except that $f_i(\vec{g})$ is the atomic form factor in that case. On the other hand, following equation (3.6) an equivalent expression for the structure factor is obtained:

$$F_{\vec{g}} = \frac{2\pi m e}{h^2} \int_{\text{cell}} V(\vec{r}) e^{-i\vec{g}\vec{r}} d\vec{r} \propto V_{\vec{g}} \tag{3.14}$$

where the scattering vector $\vec{K}'$ is a reciprocal lattice vector $\vec{g}$, and relation $\vec{g} = \vec{k'} - \vec{k}$ represents the Laue condition. Note that the structure factor is

proportional to the corresponding Fourier coefficient of the periodic potential.

The exact diffraction (Laue) condition $\vec{k''} - \vec{k} = \vec{g'}$ and deviation from this condition $\vec{k'} - \vec{k} = \vec{g} + \vec{s}$ for a given incident wave vector $\vec{k}$ and two different scattered wave vectors are shown in the Ewald sphere construction for an infinite crystal in figure 3.1. Here $\vec{s}$ is a small vector in the reciprocal space and represents the deviation from the exact Laue condition.

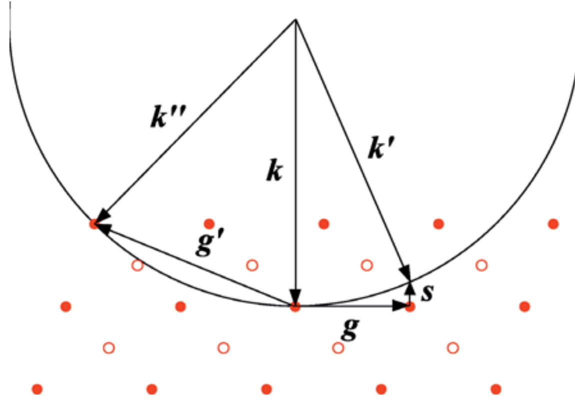

Figure 3.1: Ewald (reflecting) sphere construction for an infinite crystal. Exact diffraction condition and deviation from diffraction condition are depicted. Full red dots represent $\vec{g}$-s where $F_{\vec{g}} \neq 0$, whereas hollow red dots represent $\vec{g}$-s where $F_{\vec{g}} = 0$.

The reciprocal lattice vectors $\vec{g}$ where $F_{\vec{g}} \neq 0$ construct the actual reciprocal lattice of the given crystal. This means that when the content of the unit cell is taken into account, the reciprocal lattice of the crystal differs from the reciprocal lattice of the starting Bravais lattice by exclusion of the sites where $F_{\vec{g}} = 0$, i.e. where the scattered amplitude is zero. Therefore, in case of an infinite crystal and a given incident wave vector, the diffracted intensity will be non-zero only for the reciprocal lattice vectors which satisfy diffraction condition (intersect the Ewald sphere) and have a corresponding non-zero structure factor.

For a finite crystal, which is a realistic case, the diffracted intensities will be non-zero also in directions other than those which satisfy the diffraction condition. In order to obtain a qualitative expression for intensity distribution as a function of crystal size and deviation from the diffraction condition, we consider a real crystal with for example orthorhombic symmetry with dimensions A, B, C in directions $\vec{e}_i$, $i = x, y, z$. The lattice vectors are expressed as $\vec{r} = ua\vec{e}_x + vb\vec{e}_y + wc\vec{e}_z$, where a, b, c are the lattice constants.

The deviation vector is defined as $\vec{s} = 2\pi(s_x\vec{e}_x + s_y\vec{e}_y + s_z\vec{e}_z)$ in this case. If we leave out the factor $\frac{e^{ikr}}{r}$ [69, 70] the amplitude scattered by the whole crystal in the direction $\vec{k'} = \vec{k} + \vec{g} + \vec{s}$ becomes:

$$\psi_{\vec{g}} = \sum_n F_{\vec{g}} e^{-i(\vec{g}+\vec{s})\vec{r}_n} = F_{\vec{g}} \sum_n e^{-2\pi i(u_n a s_x + v_n b s_y + w_n c s_z)} \tag{3.15}$$

where summation goes over all unit cells. After summation or integration over the whole crystal (assuming large number of unit cells), we obtain the amplitude distribution in reciprocal space:

$$|\psi_{\vec{g}}| = \frac{F_{\vec{g}}}{V_{\text{cell}}} \frac{\sin \pi A s_x}{\pi s_x} \frac{\sin \pi B s_y}{\pi s_y} \frac{\sin \pi C s_z}{\pi s_z} \tag{3.16}$$

where $V_{\text{cell}} = abc$. The intensity distribution is given by $I_{\vec{g}}(\vec{s}) = |\psi_{\vec{g}}|^2$. The intensity distribution is a function of deviation from the diffraction condition and therefore similar for each reciprocal lattice vector $\vec{g}$. The equation (3.16) qualitatively shows how the intensity distribution in the reciprocal space depends on the crystal shape and size. In general, the intensity distribution becomes rod-like in a direction parallel to the shortest dimension of the crystal.

In case of a general TEM specimen, the crystal can be approximated to a thin plate of thickness t (C), and large in x and y directions compared to the thickness ($t \ll A, B$). Hence the intensity diffracted by a plate of thickness t becomes [70]:

$$I_{\vec{g}}(\vec{s}, t) = \frac{ABF_{\vec{g}}^2}{V_{\text{cell}}^2} (\frac{\sin \pi t s_z}{\pi s_z})^2 \delta(s_x)\delta(s_y). \tag{3.17}$$

The diffracted intensity distribution forms a spike (or a reciprocal lattice rod) in the reciprocal space. The intensity has absolute maximum for $s_z = 0$, which is the exact diffraction condition, and the minima (zero intensity) are at $s_z = nt^{-1}$, n - integer. Therefore, it is sufficient that the reciprocal lattice rod intersects the Ewald sphere to satisfy the diffraction condition for a thin crystal. The intensity distribution described by equation (3.17) is measured in DPs. In the next chapter, the diffracted intensity distribution in the real space is derived and the most important parameters which affect the image contrast are discussed.

3.1.3 DF image contrast in the kinematical theory

The absolute intensity of a diffracted beam emerging from the crystal, can be derived by several different approaches. The approach proposed by Humphreys [70], is to start from equation (3.17) and integrate over a sphere about the diffracted beam direction. In the column approximation, described by Hirsh et al. [69], the amplitude of the diffracted beam at a point at the exist surface of the crystal, can be obtained by adding the contributions from all points along a narrow column parallel to the diffracted beam. The amplitude contribution at $\vec{r}_n$ along the column is:

$$d\psi_{\vec{g}} = \frac{i\lambda F_{\vec{g}}}{V_{\text{cell}} \cos\theta} e^{-i(\vec{g}+\vec{s})\vec{r}_n} dz. \tag{3.18}$$

Here $z \parallel \vec{k'}$ and the propagation factor $e^{-i\vec{k'}\vec{r}}$ =const is omitted. The deviation parameter $\vec{s}$ is nearly parallel to z, thus $(\vec{g}+\vec{s})\vec{r}_n \approx 2\pi sz$. Next, the amplitude contribution is integrated over the crystal thickness, t:

$$\psi_{\vec{g}} = \frac{i\lambda F_{\vec{g}}}{V_{\text{cell}} \cos\theta} \int_0^t e^{-2\pi isz} dz \tag{3.19}$$

and the total amplitude of the diffracted beam $\vec{g}$ at the point of the exit crystal surface is:

$$\psi_{\vec{g}} = \frac{i\pi}{\xi_{\vec{g}}} \frac{\sin \pi ts}{\pi s} e^{-i\pi ts} \tag{3.20}$$

where $\xi_{\vec{g}}$ is called extinction distance. The extinction distance is defined as twice the distance in the crystal, which provides the unit amplitude [69, 70]:

$$\xi_{\vec{g}} = \frac{\pi V_{\text{cell}} \cos\theta}{\lambda F_{\vec{g}}} \tag{3.21}$$

where λ is the incident electron wavelength (equation 3.3). Including the equations (3.12, 3.14) into (3.21), an equivalent expression for $\xi_{\vec{g}}$ is obtained:

$$\xi_{\vec{g}} = \frac{h^2 \cos\theta}{2me\lambda V_{\vec{g}}} \tag{3.22}$$

which is useful for comparison with the extinction distance in the dynamical theory (chapter **3.1.4**).

The intensity of $\vec{g}$ diffracted beam per unit area (flux), scattered through 2θ from a crystal of thickness t in the kinematical theory of electron diffraction follows from equation (3.20):

$$I_{\vec{g}}(t,s) = (\frac{\pi}{\xi_{\vec{g}}})^2 (\frac{\sin \pi ts}{\pi s})^2 \tag{3.23}$$

where s is the deviation component normal to the crystal. The equation (3.23) describes well thickness fringes in a wedge-shaped crystal. Thickness fringes arise from the term $(\sin \pi ts)^2$ and are dependent on which diffracted beam $\vec{g}$ is selected through the extinction distance.

At the end of this section, it is useful to mention under which conditions the kinematical theory of electron diffraction breaks down. At the exact diffraction condition ($s = 0$), the diffracted flux becomes $I_{\vec{g}}(t) = (\frac{\pi t}{\xi_{\vec{g}}})^2$. Since the incident beam flux is unity, it must be $I_{\vec{g}}(t) \leq 1$. In two-beam approximation, where only the transmitted and the strongest diffracted beam are included, the maximum thickness becomes $t_{max} = \xi_{\vec{g}}/\pi$ (for $s = 0$). Thus, the kinematical theory is valid for specimen thickness below this value, which is in the order of 10 nm. This is the upper limit, since the original assumption was single scattering per electron and hence the diffracted beams should be much weaker than the incident beam.

The kinematical theory of electron diffraction gives a good approximation of how electron beam is scattered by a perfect crystal and qualitatively describes the scattered intensity distribution. This approach is however too simplified because in reality, the specimen thickness by far exceeds the maximum allowed by the kinematical theory and multiple scattering events within the crystal have to be taken into account.

3.1.4 Dynamical theory of electron diffraction

The main principles of the dynamical theory of electron diffraction are described in this chapter. The dynamical theory introduces the realistic assumption that a fast electron experiences multiple scattering within the crystal. As in the kinematical theory, the starting point is the time independent Schrödinger equation (3.2) with the periodic crystal potential described by equations (3.11, 3.12) and the scattering is considered to be elastic. However, the multiple-scattering events have to be included in the solution. Contrary to the kinematical theory where the solution takes the same form as for electron scattering by single atom, here the solution takes the same form as in Bloch band theory [71]. A Bloch wave can be expressed as [70, 71]:

$$\psi(\vec{r}) = C(\vec{r})e^{i\vec{k}\vec{r}} \tag{3.24}$$

where $C(\vec{r})$ has the periodicity of the lattice and can be expanded into a Fourier series over the reciprocal lattice:

$$\psi(\vec{r}) = \sum_{\vec{g}} C_{\vec{g}} e^{i(\vec{k}+\vec{g})\vec{r}}. \tag{3.25}$$

When the Bloch wave, equation (3.25), and the periodic potential, equation (3.11), are included into the Schrödinger equation (3.2), an infinite set of equations is obtained, i.e. one equation for each reflection $\vec{g}$ (or for each $C_{\vec{g}}$). The problem of electron diffraction by a crystal is in principle similar to the band theory. In contrast with the band theory, the total electron energy is a given quantity in electron diffraction and allowed electron wave vectors $\vec{k}$ within the crystal need to be determined from the Schrödinger equation. Therefore, an infinite set of Bloch waves with differing wave vectors $\vec{k}_i$ is obtained.

The general solution of Schrödinger equation or the total wave function of a fast electron within a crystal is a linear combination of the Bloch waves [70]:

$$\Psi(\vec{r}) = \sum_i \sum_{\vec{g}} \alpha_i C^i_{\vec{g}} e^{i(\vec{k}_i+\vec{g})\vec{r}}. \tag{3.26}$$

At the exit surface of the crystal, the total wave function decouples into an ensemble of plane waves propagating into directions $\vec{k}_i + \vec{g}$. These plane waves interfere resulting in the $\vec{g}$ diffracted beam with the amplitude:

$$\psi_{\vec{g}}(t) = \sum_i \alpha_i C^i_{\vec{g}} e^{ik_{iz}t} \tag{3.27}$$

where t is the crystal thickness and z is defined as perpendicular to $\vec{g}$.

In practice, a finite number of reflections is taken into account for calculations. The first approximation is two-beam approach where only the transmitted beam $\vec{g} = 0$ and one reflected beam $\vec{g}$ are considered. The two-beam approximation gives as the solution two values of the electron wave vector inside the crystal ($\vec{k}_1$, $\vec{k}_2$), each corresponding to a different Bloch wave, for a given incident electron energy eE. In this approximation, the extinction distance is defined as the inverse of the separation between the z-components of the two wave vector solutions [70]:

$$\xi_{\vec{g}} = \frac{2\pi}{k_{1z} - k_{2z}} = \frac{h^2 \cos\theta}{2me\bar{\lambda}V_{\vec{g}}} \tag{3.28}$$

where $\bar{\lambda} = \frac{h}{\sqrt{2me(E+V_0)}}$ is the mean electron wavelength within the crystal and V_0 the mean crystal potential. The expression for the extinction distance in the dynamical theory, equation (3.28), is exactly the same as in the kinematical theory, equation (3.22), except that the mean electron wavelength within the crystal is substituting the incident electron wavelength.

The equation (3.27) is the starting point for calculation of the diffracted intensities in the two-beam approximation. At the exact Bragg condition,

the intensities are $I_0(t) = \cos^2(\pi t/\xi_{\vec{g}})$ and $I_{\vec{g}}(t) = \sin^2(\pi t/\xi_{\vec{g}})$. In general case, when the deviation from the diffraction condition is included, the diffracted intensity becomes:

$$I_{\vec{g}}(t) = (\frac{\pi}{\xi_{\vec{g}}})^2(\frac{\sin \pi t s_{\mathrm{eff}}}{\pi s_{\mathrm{eff}}})^2 \tag{3.29}$$

where s_{eff} is the effective deviation parameter, defined as:

$$s_{\mathrm{eff}} = \sqrt{s^2 + \frac{1}{\xi_{\vec{g}}^2}}. \tag{3.30}$$

This is an important difference compared to the kinematical theory. The extinction distance is an extremely important parameter affecting the image contrast in the dynamical theory. The effective deviation parameter implies that the periodicity of the thickness fringes depends not only on the deviation from the diffraction condition but on the extinction distance for the selected reflection as well.

To conclude, the theory of electron diffraction explains the intensity variations in the DF and BF images and DPs. This is important for qualitative understanding of the TEM images and DPs, especially in the case of a nanostructured material where both crystal size and morphology matter.

3.2 Crystal phases and Structure factors

The two dominant crystal phases for III-V NWs are described in more detail in this chapter. Structure factors for ZB and WZ GaAs are derived and example of a simulated electron DP is presented for each phase.

3.2.1 Space groups for ZB and WZ GaAs

The space group describing ZB GaAs is T_d^2 in Schönflies notation or $F\bar{4}3m$ in Hermann-Mauguin notation (No 216). The lattice constant of ZB GaAs is of $a_{\mathrm{ZB}} = 5.65325$ Å [17]. The ZB unit cell is shown in figure 3.2(a). The Ga and As atoms are at $(0, 0, 0)$ (Wyckoff position a) and $(\frac{1}{4}, \frac{1}{4}, \frac{1}{4})$ (Wyckoff position c) respectively with cite symmetry T_d.

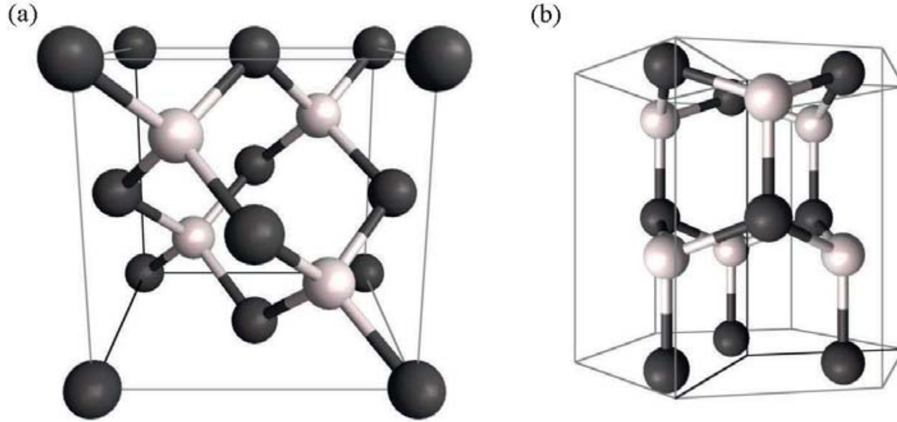

Figure 3.2: (a) ZB GaAs unit cell on [014] zone, (b) WZ GaAs unit cell on $[5\bar{1}\bar{4}0]$ zone. Ga - black, As - white. Images are made in JEMS software [61].

The space group describing WZ GaAs is C_{6v}^4 or $P6_3mc$ (No 186) [72]. The lattice constants are $a_{\mathrm{WZ}} = 3.989(1)$ Å and $c = 6.564(1)$ Å. The ratio $\frac{c}{a_{\mathrm{WZ}}} = 1.6455(5)$ is slightly larger than the ratio of $\sqrt{8/3}$ for an ideal hexagonal lattice. The WZ unit cell is shown in figure 3.2(b). The Ga and As atoms are at $(\frac{1}{3}, \frac{2}{3}, 0)$ and $(\frac{1}{3}, \frac{2}{3}, u)$ respectively with cite symmetry C_{3v} (Wyckoff position b), where the experimental value of $u = 0.373(1)$ [72] is very close to the ideal value of 0.375 [71].

The lattice constants for ZB phase and the corresponding ideal WZ phase are related as $a_{\mathrm{ZB}} = a_{\mathrm{WZ}}\sqrt{2}$. The experimental value for a_{WZ} deviates for less than 0.009 Å from this condition. The Ga-As bond length is considered to be the same for ZB and corresponding ideal WZ phase:

$d_{\text{Ga-As}} = \frac{\sqrt{3}}{4}a_{\text{ZB}} = \sqrt{\frac{3}{8}}a_{\text{WZ}} = \frac{3}{8}c$. In both phases, Ga (As) atoms are tetrahedrally surrounded by As (Ga) atoms and 9 out of 12 nearest neighbours are at the same positions, see figure 3.2.

3.2.2 The Structure factor for ZB

To calculate the structure factor, we can consider the ZB structure as a simple cubic lattice with a basis. The primitive vectors of the simple cubic lattice are: $\vec{a}_i = a_{\text{ZB}}\vec{e}_i$, $i = x, y, z$, where $\vec{e}_i$ are the orts of an orthogonal coordinate system with the origin at a lattice site, see figure 3.2(a). The basis of ZB GaAs therefore, consists of four Ga and four As atoms at the following positions, represented in the cubic $\{\vec{a}_i\}$ basis:

$$\text{Ga}: \ \vec{r}_1 = (0,0,0),\ \vec{r}_2 = (\frac{1}{2},\frac{1}{2},0),\ \vec{r}_3 = (\frac{1}{2},0,\frac{1}{2}),\ \vec{r}_4 = (0,\frac{1}{2},\frac{1}{2});$$

$$\text{As}: \ \vec{r}_5 = (\frac{1}{4},\frac{1}{4},\frac{1}{4}),\ \vec{r}_6 = (\frac{3}{4},\frac{3}{4},\frac{1}{4}),\ \vec{r}_7 = (\frac{3}{4},\frac{1}{4},\frac{3}{4}),\ \vec{r}_8 = (\frac{1}{4},\frac{3}{4},\frac{3}{4}).$$

The reciprocal lattice is simple cubic with primitive vectors: $\vec{b}_i = \frac{2\pi}{a_{\text{ZB}}}\vec{e}_i$, $i = x, y, z$. Following equation (3.13), the structure factor for ZB GaAs is given by:

$$F_{\vec{g}} = \sum_{j=1}^{8} f_j(\vec{g})e^{-2\pi i(hu_j+kv_j+lw_j)} \tag{3.31}$$

where $f_j(\vec{g})$ is the atomic scattering amplitude for electron diffraction (or atomic form factor for X-ray diffraction) associated with a reflection given by the reciprocal lattice vector $\vec{g} = (h, k, l)$, for the atom within the basis, at the position $\vec{r}_j = (u_j, v_j, w_j)$. Further development of the equation (3.31) results in:

$$F_{\vec{g}} = (f_{\text{Ga}}(\vec{g}) + f_{\text{As}}(\vec{g})e^{-\frac{i\pi}{2}(h+k+l)})S_{hkl}^{\text{FCC}} \tag{3.32}$$

$$S_{hkl}^{\text{FCC}} = 1 + e^{-i\pi(h+k)} + e^{-i\pi(k+l)} + e^{-i\pi(l+h)} \tag{3.33}$$

where S_{hkl}^{FCC} is the geometrical structure factor for a monoatomic face centered cubic (FCC) lattice. The equation (3.33) gives the allowed and forbidden reflections for the FCC lattice:

$$S_{hkl}^{\text{FCC}} = \begin{Bmatrix} 0 & h,k,l \text{ mixed} \\ 4 & h,k,l \text{ all odd or all even} \end{Bmatrix}. \tag{3.34}$$

The sites with $S_{hkl}^{\text{FCC}} = 4$ construct the body centered cubic (BCC) lattice with a lattice constant of $\frac{4\pi}{a_{\text{FCC}}}$, where $a_{\text{FCC}} = a_{\text{ZB}}$ in this case. Finally

the structure factor for ZB GaAs is obtained from the equations (3.32) and (3.34):

$$F_{\vec{g}}^{\text{ZB GaAs}} = \begin{Bmatrix} 0 & h,k,l \text{ mixed} \\ 4(f_{\text{Ga}}(\vec{g}) - i f_{\text{As}}(\vec{g})) & h,k,l \text{ all odd and } h+k+l = 4n+1 \\ 4(f_{\text{Ga}}(\vec{g}) + i f_{\text{As}}(\vec{g})) & h,k,l \text{ all odd and } h+k+l = 4n+3 \\ 4(f_{\text{Ga}}(\vec{g}) - f_{\text{As}}(\vec{g})) & h,k,l \text{ all even and } h+k+l = 4n+2 \\ 4(f_{\text{Ga}}(\vec{g}) + f_{\text{As}}(\vec{g})) & h,k,l \text{ all even and } h+k+l = 4n \end{Bmatrix} \tag{3.35}$$

where n is integer. The kinematically allowed reflections are for example (000), (111), (002), (220), (113). ZB GaAs DP on $[1\bar{1}0]$ zone, obtained by all beams dynamical calculation for a 100 nm thick crystal, is shown in figure 3.3. For comparison see experimental DP (recorded on film) of a twinned ZB segment in NW, shown in figure 2.5(d).

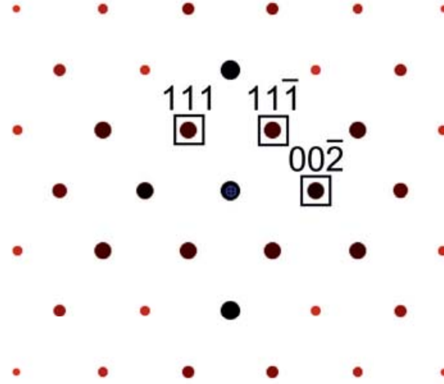

Figure 3.3: ZB GaAs DP on $[1\bar{1}0]$ zone made in JEMS software [61], for crystal thickness of 100 nm. The hue and size of the spots reflects the intensity of reflections. The intensities depend of the crystal thickness.

3.2.3 The Structure factor for WZ

The WZ structure consists of two, Ga and As, inter-penetrating hexagonal close-packed (HCP) lattices. To calculate the structure factor, we consider the WZ structure as a simple hexagonal lattice with a basis. First, we define the primitive vectors of the simple hexagonal lattice in an orthogonal coordinate system defined in figure 3.4:

$$\vec{a}_1 = (1, -\sqrt{3}, 0)\frac{a_{\mathrm{WZ}}}{2},\ \vec{a}_2 = (1, \sqrt{3}, 0)\frac{a_{\mathrm{WZ}}}{2},\ \vec{c} = (0, 0, 1)c$$

where $c = \sqrt{\frac{8}{3}}a_{\mathrm{WZ}}$ for the ideal simple hexagonal lattice. Following equation (3.10), the simple hexagonal reciprocal lattice is obtained with the primitive vectors:

$$\vec{b}_1 = (\sqrt{3}, -1, 0)\frac{2\pi}{a_{\mathrm{WZ}}\sqrt{3}},\ \vec{b}_2 = (\sqrt{3}, 1, 0)\frac{2\pi}{a_{\mathrm{WZ}}\sqrt{3}},\ \vec{c'} = (0, 0, 1)\frac{2\pi}{c}.$$

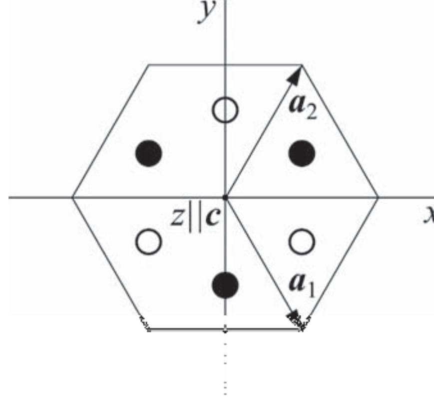

Figure 3.4: A coordinate system for a simple hexagonal lattice and primitive vectors. Example: Ga atoms in WZ structure at $\vec{c} = 0$ (full black circles) and at $\vec{c} = \frac{c}{2}\vec{e}_z$ (hollow black circles).

The basis of ideal WZ GaAs consists of two Ga and two As atoms at the following positions, represented in the hexagonal $\{\vec{a}_1, \vec{a}_2, \vec{c}\}$ basis:

$$\mathrm{Ga}:\ \vec{r}_1 = (\frac{1}{3}, \frac{2}{3}, 0),\ \vec{r}_2 = (\frac{2}{3}, \frac{1}{3}, \frac{1}{2});$$

$$\mathrm{As}:\ \vec{r}_3 = (\frac{1}{3}, \frac{2}{3}, \frac{3}{8}),\ \vec{r}_4 = (\frac{2}{3}, \frac{1}{3}, \frac{7}{8}).$$

Following the equation (3.13) and performing summation over the WZ basis, the structure factor for WZ GaAs is given by:

$$F_{\vec{g}} = f_{\mathrm{Ga}}(\vec{g})(e^{-2\pi i(\frac{1}{3}h+\frac{2}{3}k)} + e^{-2\pi i(\frac{2}{3}h+\frac{1}{3}k+\frac{1}{2}l)})$$
$$+ f_{\mathrm{As}}(\vec{g})(e^{-2\pi i(\frac{1}{3}h+\frac{2}{3}k+\frac{3}{8}l)} + e^{-2\pi i(\frac{2}{3}h+\frac{1}{3}k+\frac{7}{8}l)}). \tag{3.36}$$

Equation (3.36) can be developed further into:

$$F_{\vec{g}} = (f_{\mathrm{Ga}}(\vec{g}) + f_{\mathrm{As}}(\vec{g})e^{-\frac{3}{4}i\pi l})S_{hkl}^{\mathrm{HCP}} \tag{3.37}$$

$$S_{hkl}^{\mathrm{HCP}} = e^{-2\pi i(\frac{1}{3}h+\frac{2}{3}k)} + e^{-2\pi i(\frac{2}{3}h+\frac{1}{3}k+\frac{1}{2}l)} \tag{3.38}$$

where S_{hkl}^{HCP} is the geometrical structure factor for a monoatomic hexagonal close-packed lattice. Equation (3.38) gives the allowed and forbidden reflections for the hexagonal close-packed lattice. To develop further and simplify the equation (3.38), we take the square amplitude of S_{hkl}^{HCP}:

$$|S_{hkl}^{\mathrm{HCP}}|^2 = \left\{ \begin{matrix} 0 & l \text{ odd}, \ h-k=3n \\ 3 & l \text{ odd}, \ h-k \neq 3n \\ 4 & l \text{ even}, \ h-k=3n \\ 1 & l \text{ even}, \ h-k \neq 3n \end{matrix} \right\} \tag{3.39}$$

where n is integer. The additional factor $f_{\mathrm{Ga}}(\vec{g}) + f_{\mathrm{As}}(\vec{g})e^{-\frac{3}{4}i\pi l}$ in the equation (3.37) introduces no qualitative changes to $F_{\vec{g}}$. To summarize the conditions, the square amplitude of the WZ GaAs structure factor is expressed as:

$$|F_{\vec{g}}^{\mathrm{WZ\ GaAs}}|^2 = \left\{ \begin{matrix} 0 & l \text{ odd}, \ h-k=3n \\ 3(f_{\mathrm{Ga}}^2 \pm \sqrt{2}f_{\mathrm{Ga}}f_{\mathrm{As}} + f_{\mathrm{As}}^2) & l \text{ odd}, \ h-k \neq 3n \\ 4(f_{\mathrm{Ga}}^2 + f_{\mathrm{As}}^2) & l=4m+2, \ h-k=3n \\ (f_{\mathrm{Ga}}^2 + f_{\mathrm{As}}^2) & l=4m+2, \ h-k \neq 3n \\ 4(f_{\mathrm{Ga}} \pm f_{\mathrm{As}})^2 & l=4m, \ h-k=3n \\ (f_{\mathrm{Ga}} \pm f_{\mathrm{As}})^2 & l=4m, \ h-k \neq 3n \end{matrix} \right\} \tag{3.40}$$

where m and n are integers. The kinematically allowed reflections are for example $(1\bar{1}0)$, (002), $(1\bar{1}1)$. It is common to use the four-index system for hexagonal structures, where an additional direct lattice primitive vector is defined as $\vec{a}_3 = -\vec{a}_1 - \vec{a}_2$ and a zone axis becomes $(uv\bar{j}w)$, $j = u + v$. The reciprocal lattice vectors are thus expressed as $(hk\bar{i}l)$, $i = h+k$. These reflections become: $(1\bar{1}00)$, (0002), $(1\bar{1}01)$. WZ GaAs DP on $[11\bar{2}0]$ zone, obtained by all beams dynamical calculation for a 100 nm thick crystal, is shown in figure 3.5 without (a) and with (b) double diffraction. The forbidden reflections (see figure 3.5(b)) are commonly observed in the experimental DPs (figure 2.5(b)) due to double diffraction [70, 76].

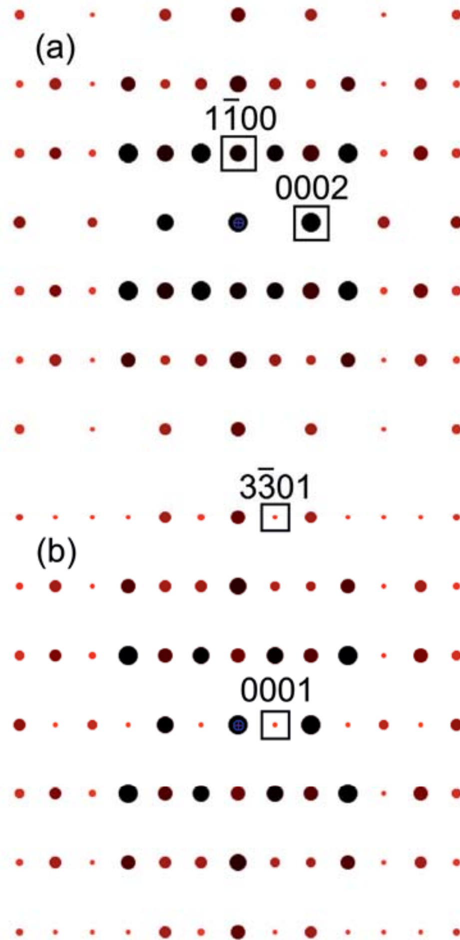

Figure 3.5: WZ GaAs DP on $[11\bar{2}0]$ zone made in JEMS software [61], for crystal thickness of 100 nm without (a) and with (b) double diffraction. The additional reflections in (b), for example (0001) and $(3\bar{3}01)$, are forbidden, but present due to double diffraction. The hue and size of the spots reflects the intensity of reflections. The intensities depend on the crystal thickness.

Chapter 4

Experimental Techniques

4.1 Molecular beam epitaxy

MBE is a non-equilibrium growth technique used for growing thin epitaxial films and wide variety of nano-structured materials [73]. The molecules or atoms, evaporated from the effusion cells, are deposited on the substrate in a chamber under ultra high vacuum (UHV). The temperature of an effusion cell determines the flux. Extremely low growth rates, down to 0.1 MLs^{-1}, can be achieved by changing the temperatures of the effusion cells. Deposition in UHV chamber results in a high purity of the materials.

The MBE system used for NW growth in this work was a Varian Gen II Modular system. Figure 4.1 shows a schematic diagram of this system. UHV vacuum (1×10^{-10} Torr) is achieved in the growth chamber by system of pumps and cooling of the inner chamber walls. The effusion cells lie on a sphere section, with the centre at the substrate. Thus, it is possible to create similar conditions for fluxes impinging from different effusion cell positions onto the substrate. The fluxes can be measured by bringing the ion gauge to the growth position. The effusion cells installed in the used MBE are: As valved cracker cell, Sb valved cracker cell, dual filament Ga cell, Al cell, In cell and three doping cells (Si, Te, Be). Fluxes of molecules or atoms can be abruptly released or stopped by controlling the shutters in front of the cells. Continuous azimuthal rotation (CAR) system provides the substrate rotation during the growth.

UHV allows installation of in-situ characterization techniques such as reflection high-energy electron diffraction (RHEED) and mass spectrometer. RHEED is used to determine the surface reconstruction of the substrate or to monitor the symmetry (arrangement) of the surface of the material as it grows. The electron gun emits electrons in energy range $5 - 50$ keV, and

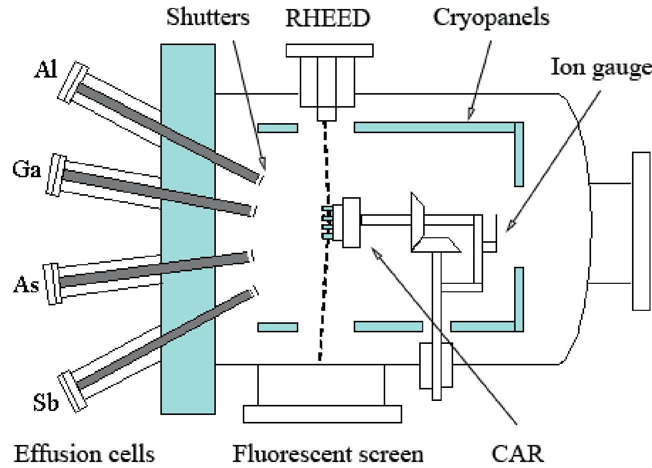

Figure 4.1: Simplified schematic diagram of the used MBE system [23]. Four effusion cells (Ga, As, Sb, Al) are included in the drawing.

the energy is usually set to 8 keV. The electron beam hits the substrate at a low grazing angle. The electrons diffracted from the substrate surface are recorded on the fluorescent screen. In case of NWs, RHEED can distinguish whether the symmetry is cubic or hexagonal during the growth.

4.2 Micro-photoluminescence

Micro-PL spectroscopy is a powerful tool for non-destructive characterization of bulk and nanostructured semiconductors. Various micro-PL techniques can be used to obtain information about bandgap and exciton binding energies, material purity, types of defects present, and band alignment in homo- and heterostructured materials [43]. Luminescence stands for all radiative recombination processes in matter. The types of luminescence are distinguished by the source of excitation, for example: light (photoluminescence), electric current (electro-), electron beam (cathodo-), a chemical reaction (chemi-). In photoluminescence, light absorption leads to generation of electron-hole pairs, which may form free or bound excitonic complexes, or get trapped at defect levels [43].

Light absorption can occur at any energy above the bandgap, whereas (free-carrier) luminescence, in the ideal case (defect free material), results in only one well-defined peak which indicates at the bandgap of the mate-

rial. This is because free carriers thermalize, i.e. relax non-radiatively, from higher excited states towards the edge of their band. Thermalization is a rapid process, where electrons and holes decay to the ground state, from which they can radiatively recombine. Interband luminescence is recombination between electrons at the bottom of the conduction band and holes at the top of the valence band. Interband luminescence is probable only in direct bandgap materials, such as GaAs, since both absorption and emission occur at the centre of the first Brillouin zone, i.e. vertically in $\vec{k}$-space [43,71]. For indirect bandgap materials, for example Si, the interband luminescence has to be phonon-assisted, which makes this process much less probable.

In direct bandgap semiconductors, formation of excitons is favoured over existence of free carriers under certain conditions [43]. An exciton is a quasi-particle consisting of an electron and a hole which are interacting electrostatically (Coulomb). Mott-Wannier type excitons [74], where electron-hole distance is larger than the lattice constants, are characteristic for inorganic semiconductors and insulators. Excitons are observed in bulk and nanostructured materials if the thermal energy of the carriers ($k_\mathrm{B}T$), or interaction energy between the carriers and an external field, does not exceed the exciton binding energy. In bulk ZB GaAs, the exciton binding energy is relatively small (4.2 meV) compared to the Boltzmann factor at room temperature (26 meV). Hence, excitons in ZB GaAs are observed at low temperatures ($\lesssim$ 50 K), whereas interband luminescence occurs at higher ($\gtrsim$ 50 K) temperatures. The excitonic luminescence is annihilation of an exciton accompanied by the emission of a photon. Thus, a free exciton peak is observed in the PL spectra instead of the interband luminescence. The difference between the bandgap and the free exciton energy, at the same temperature, is precisely the exciton binding energy.

PL is in general extremely sensitive to material purity, structural defects, surface states and strain, which may result in additional PL peaks or non-radiative recombination processes [43]. Dopants or defects, such as impurities, create additional energy levels within the bandgap which can trap free carriers or excitons, resulting in many additional routes for luminescent recombination. Native defects, such as vacancies and interstitials, can create deep levels, if they are highly localized in the lattice, and act as radiative or non-radiative recombination centres. The MBE grown GaAs-based heterostructured NWs used in this work, proved to be rather clean of impurities and carbon-related PL peaks were not observed. Inherent structural defects and composition variation, as well as complexity of a heterostructure, are expected to have the most dominant effects on the NW optical properties. The effect of surface states is also prominent on the NW optical properties,

so that any open GaAs surface promotes non-radiative recombination which in turn reduces the overall PL intensity.

Nanostructured materials can exhibit quantum confinement effects in the optical properties when the structure size becomes order of or smaller than the free exciton radius. The most prominent effect is that the bandgap increases as the size decreases. The density of states is modified for quantum-confined compared to bulk materials, such that several different sub-bands appear in quantum wells and wires, or several distinct levels in quantum dots [43,75], which replace the continuous density of states in bulk [71]. The exciton binding energy in a quantum confined material is larger than in the bulk, which means that excitons can be observed at higher temperatures. In case of semiconductor heterostructured NWs, with the core diameters of ~ 40 nm or larger, no quantum confinement is expected since NW diameter is about an order of size larger than the exciton Bohr radius (~ 6 nm for GaAs). The same can be said for the axial inserts in NWs, with lengths larger than ~ 20 nm. Thus, these NWs are still regarded as bulk materials. However, small segments ($1 - 10$ nm in length) of a different crystal phase can form unintentionally within NWs (see chapter **2.2**), and may act as quantum wells and disturb PL recombination in the surrounding dominant crystal phase. In addition, the length of smaller-bandgap inserts in axial NW heterostructures, can be, in principle, decreased enough to achieve a quantum confined volume. This would reflect in appearance of some excited states within the insert related PL emission in power-dependent PL spectra.

There are many different PL techniques such as power-dependent, polarization-resolved, temperature-dependent, time-resolved, magneto-PL, PL excitation [43]. The techniques used within this work are listed in the following:

1. Power-dependent PL is the simplest PL technique which most frequently is used. The intensity of excitation is varied and the dependence of different PL peaks on the excitation level is recorded. The power-dependent behaviour reflects the mechanisms of carrier recombination at different levels of excitation. In such a way, defect related PL and intrinsic PL can be distinguished. Namely, defects can trap a limited number of carriers and the related PL peak would saturate at a certain excitation power, whereas the intensity of the excitonic luminescence would keep increasing. However, there is a limit for the intensity of excitonic luminescence, i.e. when the excitation power becomes high enough to excite plasmons instead of excitons.

2. In polarization-resolved PL, the linear polarization of the excitation beam is varied and the polarization of the PL is analysed (see chapter **2.5.1**). This technique can be used to determine the recombination route of different PL peaks, especially in correlation with structural characterization, by

considering the optical selection rules and symmetries of the valence and conduction band states.

3. Temperature-dependent PL spectra give information about how PL energy, line-width and intensity evolve with temperature and at which temperature the excitonic luminescence becomes interband luminescence. The free exciton energy temperature dependence gives insight into the electronic properties of the material.

4. Time-resolved PL can be used to determine the lifetimes of carriers, which are relevant for estimating the internal quantum efficiency of a material. The main differences between time-resolved PL and the other PL techniques described here, are that the excitation is pulsed and detector is a streak camera. The streak camera is an ultrahigh-speed photodetector capable of detecting phenomena on picosecond timescale. Time-dependence of PL emission under pulsed excitation is measured, and by further processing and fitting of the experimental data, carrier lifetimes can be extracted.

The micro-PL setup used here is shown in figure 4.2. The sample is placed on a cold finger on a high-precision (10 nm) 3D piezoelectric positioning stage within a Janis ST-500 cryostat. The power-dependent micro-PL was performed at $\sim$ 15 K, using continuous wave Nd:YVO laser at the wavelength of 532 nm or continuous wave Ti:sapphire laser tuned to 780 nm, when it was needed to excite only the GaAs core. The power density at the specimen can be varied from $\sim$ 200 W/cm^2 to $\sim$ 10 kW/cm^2. The laser beam is reflected by a beam splitter towards a high-numerical aperture lens (0.65). The excitation beam is focused to a $\sim$ 1.5 μm laser spot by the lens.

The PL signal is collected by the same lens, transmitted through the beam splitter, guided towards the spectrometer and focused onto the entrance slit of the spectrometer (Single Grating Jobin Yvon iHR550 spectrometer, spectral resolution up to $\sim$ 0.5 nm). The laser beam, reflected from the specimen, goes back through the lens but is rejected by a filter. Inside the spectrometer, the PL signal is collected by a spherical mirror, collimated and reflected to the grating (300 grooves/mm), which disperses the light. The grating can be rotated and the angle of the grating defines the spectral range which falls onto the second spherical mirror. The second mirror collects and focuses the PL light onto the exit slit of the spectrometer where a charge-coupled device (CCD) camera is placed. The CCD matrix exactly coincides with the plane of the exit slit. The signal is processed digitally and plotted as PL intensity versus energy or wavelength. For power-dependent, polarization-resolved and temperature-dependent PL an electronically cooled Andor Newton Si electron multiplying CCD with a detection range of $\sim 200 - 1000$ nm was used. For time-resolved PL a pulsed

Spectra Physics Tsunami Ti:sapphire laser was used to provide $\sim$ 2 ps full-width-at-half-maximum pulses at 780 nm. Time-resolved measurements were carried out with a Princeton Optics Acton SP2500 spectrometer and an Optronis Optoscope SC-10 NIR enhanced streak camera.

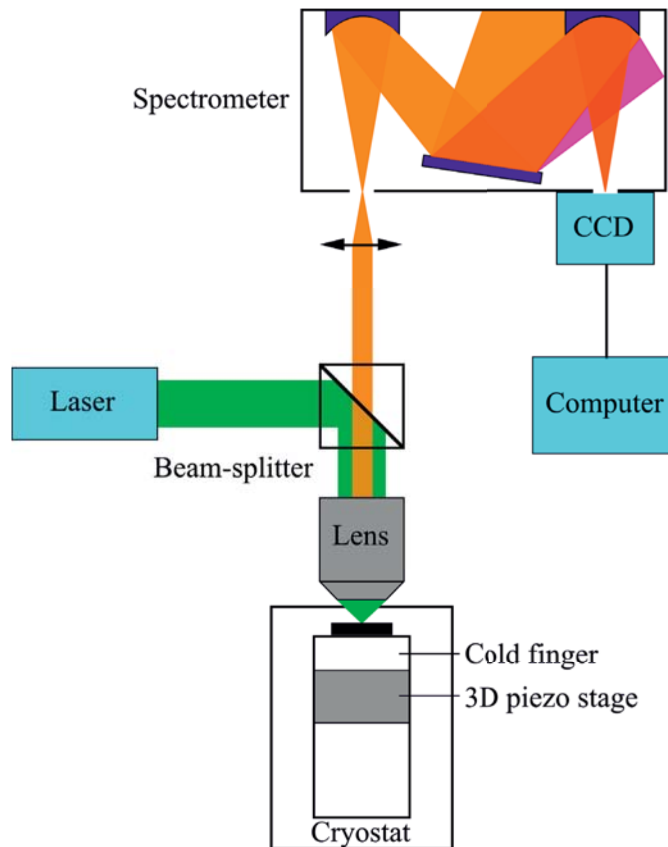

Figure 4.2: Simplified schematic diagram of a micro-PL setup. The laser beam is focused by the lens onto the sample in the cryostat. The PL is collected by the same lens and guided towards the spectrometer.

4.3 The Transmission Electron Microscope

4.3.1 Introduction to TEM

TEMs are powerful and versatile tools for the characterization of materials over wide spatial ranges: from the atomic scale, through nanoscale (< 1 nm to ~ 100 nm) up to micrometer size and above. The ultimate limit for the resolution in TEM should be the electron wavelength which is 0.00251 nm at 200 kV (equation (3.1)). However, the realistic point resolution limit is set by lens aberrations and stability issues. This value is about ~ 0.5 Å for the state-of-the-art machines today [76].

In the theory of electron diffraction in chapter **3.1**, only elastic scattering is considered, and such theoretical approach is much simpler than what actually happens in a TEM. High-energy electrons are ionizing radiation, which in general produces a wide range of secondary signals upon interaction with a material. The secondary signals, commonly detected in TEMs/SEMs, created upon the interaction of the high-energy electron beam with a thin specimen, are schematically presented in figure 4.3. In addition, there are other processes happening and other signals which are rarely detected in TEM, such as electron absorption, emission of light (cathodoluminescence), Auger electrons, etc.

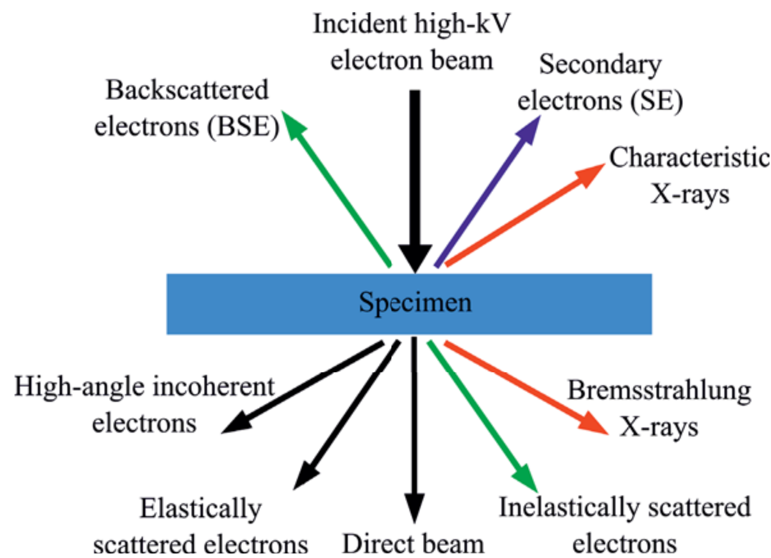

Figure 4.3: Simplified schematic diagram of the interaction of high-energy electron beam with a thin specimen: secondary signals detected in TEMs/SEMs. Adapted from reference [76].

The coherent elastically (forward) scattered electrons are used to form DPs, BF and DF TEM, and HRTEM images. The inelastically scattered electrons can loose energy in many different processes: absorbtion, excitation of plasmons, ionization of atoms, electron-hole pair creation, interaction with phonons i.e. thermal diffuse scattering (TDS), etc. The inelastically scattered electrons, which have ionized the atoms within the specimen, are analyzed by electron energy loss spectroscopy (EELS) or used to form energy filtered TEM images. The accompanying characteristic X-ray spectrum, together with bremmstrahlung X-ray background, is measured by EDX. EELS and EDX give information about the composition of the specimen. The incoherent electrons, scattered at high-angles, form HAADF STEM image. The secondary electrons (SE), emerging from the specimen due to ionization, or the backscattered electrons (BSE) can be detected as well to form SE or BSE image respectively (chapter **4.4**).

Here a Phillips CM30 (LaB_6) and a Jeol 2010F TEM/STEM (Schottky field emission gun), both operated at 200 kV, were used. Techniques used in the Phillips CM30 were BF, DF, SAED and HRTEM. Images were taken on a 1k CCD (Tietz) or on films (scanned in at 600 or 1200 dpi). The Jeol 2010F was used for lattice imaging (HRTEM), HAADF STEM and EDX in STEM mode. In HAADF STEM, the probe size was approximately 1 nm and the camera length was 15 cm for analytical work and lower magnification imaging. Double tilt holders were used for both microscopes. Single tilt holder was also used for Jeol 2010F in case when a double tilt holder was unavailable or unsuitable due to the Si/SiN grid thickness (see paper I).

4.3.2 Conventional TEM

The principles of the three most conventional TEM techniques, selected area electron diffraction (SAED), BF and DF imaging, are shown in figure 4.4. To form a DP, a SAED aperture is inserted in the first intermediate image plane (figure 4.4(a)), between the objective and the intermediate lens, and a region of the image is selected. This imposes a virtual aperture in the specimen plane, and acts as if approximately the same region of the specimen is selected. The spatial resolution of the selected area aperture is $\sim$ 100 nm [76], sufficient for analysing single NWs. In diffraction mode, strength of the intermediate lens is adjusted so that the DP forms on the fluorescent screen. SAED was used to identify the crystal phases and the growth direction of the NWs.

In BF mode, the objective aperture can be inserted in the back focal plane (BFP) of the objective lens, to select the direct beam and optionally some of the diffracted beams (figure 4.4(b)). The image is formed on

the screen by modifying the strength of the intermediate lens, whereas the strength of the projector lens remains the same. In DF mode, the incident beam is tilted with respect to the optical axis. Hence, the direct beam is shifted from the optical axis, i.e. whole DP is shifted in the BFP (figure 4.4(c)). The beam tilt can be adjusted by the deflectors within condensor-system lenses, to position a particular reflection onto the optical axis. Usually the smallest objective aperture is inserted and centred onto the optical axis to select only the desired reflection to form the DF image on the screen.

There are two main types of contrast in BF and DF images: diffraction contrast and mass-thickness contrast. Diffraction contrast includes bending and strain effects, and it is dominant type of contrast for thin crystalline specimens. Diffraction contrast in DF imaging is used to distinguish between different crystal phases or orientations, by selecting a reflection characteristic for a particular crystal phase or crystal orientation. This makes the regions of the sample with the selected phase bright in the image and regions with all other phases dark, in the ideal case. Hence, DF images have a high contrast, but require longer exposure due to the low signal.

In reality, the size of the objective aperture and distance between reflections from different phases can make it difficult to select only one reflection, which results in bright, dark and grey regions in the image. In addition, thickness fringes and specimen bending affect the contrast in DF images significantly. The formation of thickness fringes in DF images is explained in chapter **3.1.3**. Specimen bending in addition induces variation of the deviation parameter for the selected reflection across the specimen. As the NWs are slightly bent over their length this results in a gradual change of the image contrast. Diffraction contrast combined with bending effects is visible also in BF images, especially if the specimen is off-zone.

Strain in a single crystal phase region in the specimen can give rise to regions of different contrast in the image. Within the strained region, the crystal lattice is distorted (i.e. bent) with respect to the unstrained lattice. If the unstrained region satisfies the diffraction condition, then there is certain deviation from the diffraction condition for the strained region, which may induce a change in the image contrast (also varying with thickness) [76]. However, by conventional BF or DF technique, it is only possible to qualitatively observe, but not to quantify the strain.

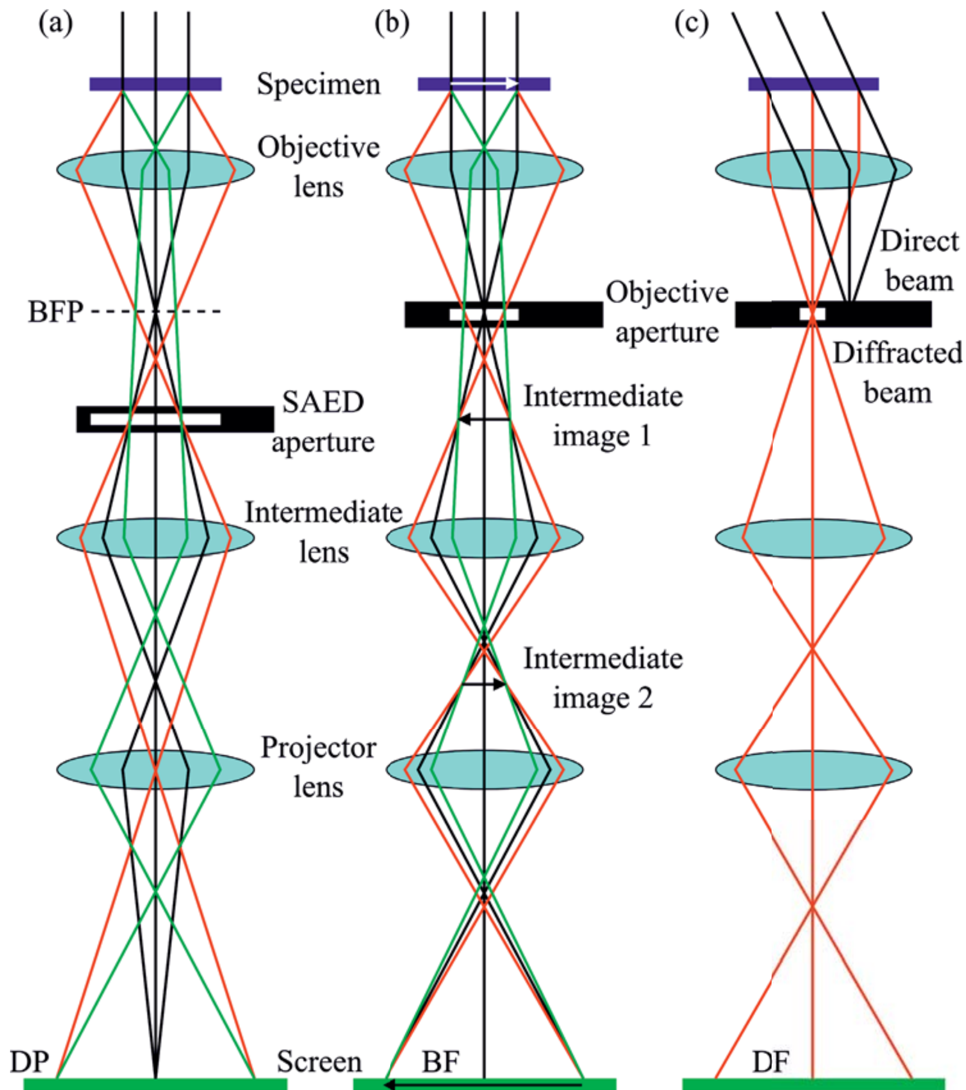

Figure 4.4: Simplified schematic diagram, adapted from reference [76], explaining the basic principles of: (a) SAED formation, (b) BF imaging, (c) DF imaging. Note that a real TEM is much more complex.

4.3.3 High resolution TEM

HRTEM images are formed by interference of the direct and the diffracted beams, and this is called phase-contrast imaging. HRTEM can be in principle explained by describing how a point within a specimen spreads into an extended region in the image due to imperfection of the objective lens [76]. Each point in the specimen is transformed into an extended region or disk in the final image. Each point in the final image contains contribution from many points in the specimen, which can be mathematically described by:

$$g(\vec{r}) = \int f(\vec{r'})h(\vec{r} - \vec{r'})d\vec{r'} \tag{4.1}$$

where $f(\vec{r}) = f(x, y)$ is specimen function, $h(\vec{r})$ point-spread function and $g(\vec{r}) = g(x, y)$ image function, which is convolution of $f(\vec{r})$ and $h(\vec{r})$. These functions can be expressed as Fourier transforms over the reciprocal space, which results in the following relation between their Fourier coefficients:

$$G(\vec{u}) = F(\vec{u})H(\vec{u}) \tag{4.2}$$

where $\vec{u}$ is a reciprocal lattice vector and $H(\vec{u})$ is called contrast transfer function. The contrast transfer function contains contributions related to apertures $A(\vec{u})$, attenuation of the wave or envelope function $E(\vec{u})$, and aberrations of the objective lens $B(\vec{u})$:

$$H(\vec{u}) = A(\vec{u})E(\vec{u})B(\vec{u}). \tag{4.3}$$

The aberration function can be expressed as:

$$B(\vec{u}) = e^{i\chi(\vec{u})},\ \chi(\vec{u}) = \pi \triangle f \lambda u^2 + \frac{1}{2}\pi C_s \lambda^3 u^4 \tag{4.4}$$

where $\triangle f$ is underfocus and C_s spherical aberration. The objective aperture cuts off all $\vec{u}$-s greater than the value defined by its radius. High spatial frequencies, i.e. high $\vec{u}$-s in the DP are scattered under a larger angle by the objective lens, which means that due to the spherical aberration these beams are not focused by the lens at the same point in the image. This is what spreading of a point in the image means.

What we actually observe in the HRTEM images is the contrast. To describe contrast, we define another contrast function:

$$T(\vec{u}) = A(\vec{u})E(\vec{u})2\sin\chi(\vec{u}) \tag{4.5}$$

which is called the intensity or objective lens transfer function. As the spherical aberration is positive for electromagnetic lenses, for $T(\vec{u}) < 0$ we get

dark atoms on a bright background, for $T(\vec{u}) > 0$ the reversed, and for $T(\vec{u}) = 0$ no contrast at all.

The contrast transfer function can be optimized by balancing the effect of spherical aberration with a particular value of underfocus, which is called Scherzer defocus. Figure 4.5 shows a series of $\sin\chi(\vec{u})$ curves for varying spherical aberration (a) and varying underfocus (b). The aim is to have as many beams as possible (as large u as possible) transferred through the optical system with identical phase, i.e. within the flat response regime. The first crossover point is defined as the instrumental point resolution limit, i.e. direct image interpretation limit. As C_s increases, the resolution limit decreases, whereas the opposite occurs as $\triangle f$ increases. However, for a certain value of $\triangle f$ a local maximum creates a new crossover point which decreases the resolution limit.

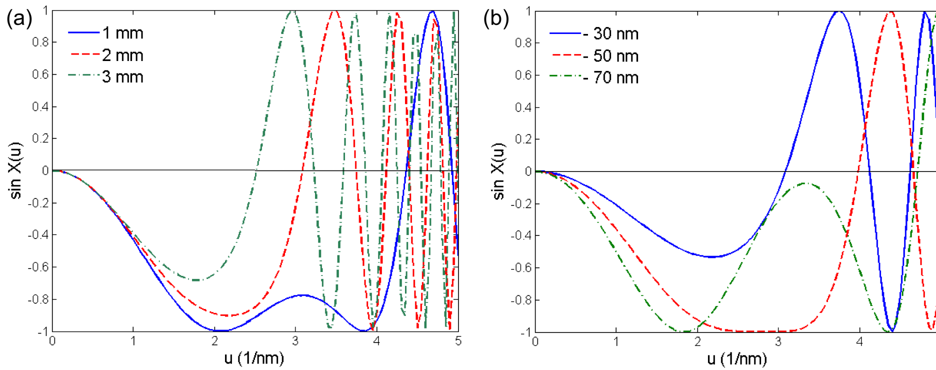

Figure 4.5: $\sin\chi(\vec{u})$ for variation of (a) C_s at $\triangle f = -60$ nm, (b) $\triangle f$ at $C_s = 1$ mm. The functions were plotted in MATLAB using the parameters from reference [76].

The resolution is also limited by the spatial coherence of the source and by chromatic effects. These are included in the envelope function, which damps out higher spatial frequences. Hence the higher order pass-bands become inaccessible, and the information limit is reached for $T(\vec{u}) = 0$. The envelope functions effectively impose a virtual aperture. Thus, the objective aperture should be smaller than this virtual aperture in order to cut off the spatial frequencies beyond the information limit.

To conclude, the principle of phase contrast imaging in HRTEM is that the images are directly interpretable up to the instrumental resolution limit. This limit is determined by the crossover for Scherzer defocus or by the envelope function, whichever equals zero first. If the information limit is

beyond the point resolution limit, we can use image simulations to interpret the details beyond the Scherzer crossover. In this work, HRTEM was used in a straightforward manner: to image interfaces and the structural defects, and to distinguish crystal phases present in a NW.

4.3.4 Scanning TEM

In STEM the image is formed by scanning a focused beam (probe) in a raster over the specimen and collecting the transmitted electrons at each probe position with a certain type of detector. The intensity of a certain pixel in the image is integrated signal received from the detector area for the corresponding probe position at the specimen. On the contrary, in TEM the whole image is generated at a time by direct illumination of the specimen with a fixed parallel beam. The magnification in STEM is increased by scanning a smaller area, whereas in TEM the magnification is altered by the lens strength. The image resolution is determined by the size of the probe, which mainly depends on the spherical aberration of the probe forming lens system.

The detector in STEM is a semiconductor device or a scintillator photomultiplier, which are both very sensitive to the number of incoming electrons. An advantage of STEM over TEM is that many detectors can be used simultaneously to detect different kinds of signals, see figure 4.6. In STEM mode, no lenses are required between the specimen and the detectors, which are inserted in a diffraction plane. At each probe position, a convergent-beam electron diffraction (CBED) pattern is formed onto this plane. In BF STEM mode, a circular detector is used, of such size that it selects only the direct beam (i.e. central disk of the CBED pattern). Contrast in BF STEM is equivalent to BF TEM contrast, both mass-thickness and diffraction contrast are present in the images. In HAADF STEM mode, an annular detector with big inner (> 50 mrad) and outer radius is used in order to detect the electrons scattered at high angles. The size of the detector and the distance between specimen exit plane and the detector, determine the angular range of the collected scattered electrons. In Jeol 2010F used here, this distance is controlled by setting the camera length with the intermediate lenses.

The high angle annular detector collects the incoherent quasi-elastically scattered electrons [77]. The intensity reaching the detector is dominated by TDS. The effects of diffraction contrast are minimized and the image is incoherent, with intensity dependent on the atomic number Z. The image intensity also depends on the specimen thickness. This can be observed for example in NW tips, see figure 2.4. In contrast to HRTEM, there are no

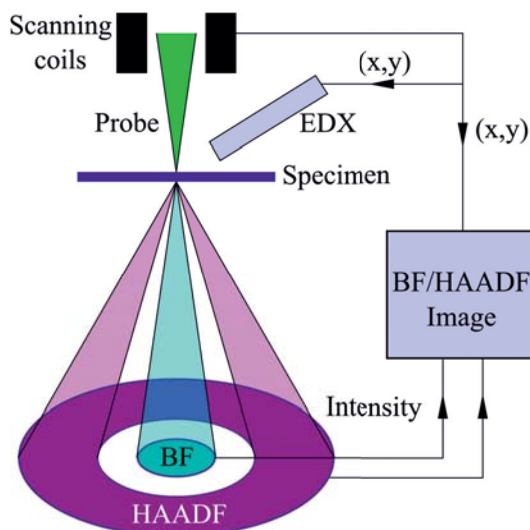

Figure 4.6: Simplified schematic diagram of STEM imaging system with BF, HAADF and EDX detectors.

contrast reversals in HAADF STEM images as the contrast transfer function is monotonously positive. This together with the Z-contrast makes HAADF STEM image interpretation simpler than in conventional TEM.

Here, HAADF STEM was used for analytical work, to image NW core-shell heterostructures or axial inserts, and as the background mode for the EDX point and line scan analysis. High resolution and quantitative HAADF STEM (by H. Kauko) was also part of the work, but the details (see reference [51]) are beyond the scope of this introduction.

4.3.5 Energy dispersive X-ray spectroscopy

EDX is an electron microscopy technique for qualitative and quantitative composition analysis with nanometer resolution [76]. The high-keV electrons ionize the atoms within the specimen (inelastic scattering) and the characteristic X-rays can be emitted. The emerging X-ray spectrum, containing peaks characteristic for the atomic species present in the specimen, is recorded. In addition, there is a continuum X-ray (bremsstrahlung) background in the spectrum, due to deacceleration of the incident electrons within the specimen.

The amounts of constituent atoms can be estimated from the relative X-ray peak intensities. However, detection and quantification of light elements is difficult, due to inherent poor efficiency of the detectors, low energy

resolution, higher background, smaller number of emitted X-rays and their absorption. Detecting small quantities of an element is rather challenging, especially for thin TEM specimens, due to the low signal. The detection limit (few atomic %) is also poor due to the low collection efficiency. This means that from all X-rays emitted from the specimen into a sphere, only $0.1 - 0.2$ sr are collected by the detector.

The EDX detector is situated in between the upper and the lower objective pole piece. The traditional EDX detector, Si(Li)-type, is shown in figure 4.7. Si(Li) is a reverse-biased p-i-n diode operating at liquid nitrogen temperature [76]. Since Si contains acceptor impurities, it has to be doped with Li to achieve intrinsic Si, which is the active region of the detector. The energy required to create an electron-hole pair in Si is ~ 3.8 eV at about 77 K. The number of created electrons (holes) is directly proportional to the energy of the X-ray photon. When a reverse bias ($0.5 - 1$ keV) is applied, the electrons and holes are separated and a charge (electron) pulse is measured at the rear contact. Recently another type of EDX detector has become commercially available: Si-drift detector (SDD). It has completely different design than Si(Li) and operates with Peltier cooling (no liquid nitrogen needed), works at lower voltage and has no Li-doping. SDDs can be designed in special shapes to significantly increase the collection angle.

The main components of an EDX system are the detector, electronics and the software. The incoming X-ray photons are processed individually, one at the time. The detector is switched off when an X-ray is detected and switched on again after that signal is processed. This is a fast process and for the operator it appears as if the whole spectrum is recorded simultaneously. The electronics attached to the detector, controlled by the software, convert the charge pulse created by the incoming X-ray into a voltage pulse. The voltage is assigned to the appropriate energy channel which is identified electronically as a specific X-ray energy. A signal, meaning one count, is stored in the energy channel for the detected X-ray. The user-friendly software calibrates the spectrum, saves the conditions under which the spectrum was acquired, identifies the peaks and gives the number of counts per channel.

The two most common artefacts in the EDX spectra, detected by a Si(Li) and SDD, are Si K_α escape peak, escaping from the detector, and sum-peaks, which appear when more than one X-ray is processed at the same time (high input count rate). These artefacts can be filtered out by the software. Stray X-ray radiation, originating from other regions than the probed specimen area, should be identified by the operator. The spectrum has normally 2048 channels and various energy ranges can be assigned to these channels. A typical energy range selected for a Si(Li) and SDD detector is 10 or 20 keV

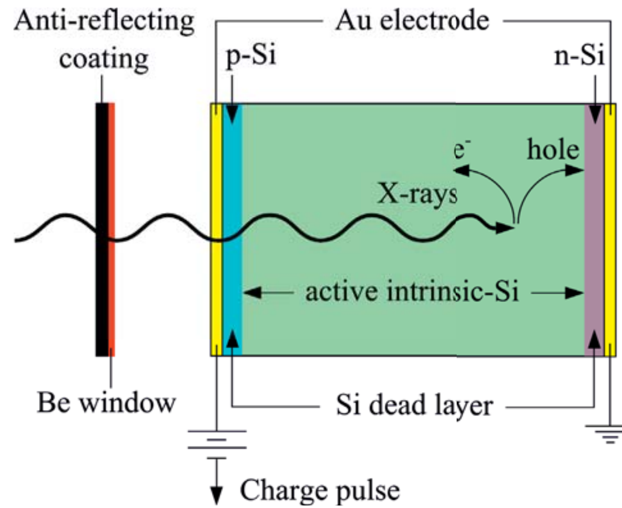

Figure 4.7: Simplified schematic diagram of a Si(Li) detector adapted from reference [76]. The X-rays pass through the berilium window and Au electrode into the intrinsic-Si active region, where they excite electron-hole pairs. The doped Si regions are called dead layers since the electron-hole pairs generated there recombine and do not contribute to the pulse.

and in 2048 channels, this results in a display resolution of 5 or 10 eV per channel, and a spectral resolution of $\sim$ 130 eV [76].

EDX can be performed both in TEM and STEM modes. In TEM mode, the beam needs to be condensed manually onto the specimen to appropriate size (limited) for EDX analysis. In such way, only an integrated EDX spectrum can be obtained from the region of interest illuminated by the condensed beam. STEM mode is preferred for EDX since the probe can be better controlled. First the image of an area in the specimen is formed. Then the scanning probe is stopped and positioned on a region of interest within that image. Point spectra, line profiles and two-dimensional composition maps can be obtained in STEM mode. EDX has higher resolution in STEM mode, due to smaller probe and since the region of interest can be defined more precisely. The spatial resolution of the point analysis is approximately the size of the probe. However, beam-broadening within the specimen is always present and this effectively increases the excited volume of the specimen.

Quantitative EDX analysis can be performed by a software or manually. Before quantifying the spectrum, artefacts such as stray radiation and sum peaks have to be identified. The software subtracts the background, inte-

grates the peaks and uses the calculated k-factors for certain crystal phase and specimen geometry [76]. The k-factors depend on the crystal lattice, illumination conditions and detector characteristics (efficiency), and these factors can induce errors in the quantification.

The Cliff-Lorimer ratio technique is used to quantify an EDX spectrum. The correlation factor k relates the concentration ratio of two elements to the ratio of counts in the obtained spectrum for those two elements [76]. The k-factor can be a calculated one, as most often is used, or experimentally determined using a calibration specimen of a known composition. Manual quantification can be applied to a combination of a binary and a ternary system with the same crystal phase, for example ZB GaAs and ZB $Ga_{0.5}As_{0.5-x}Sb_x$. ZB GaAs is used as a reference to calculate the k_{GaAs}. In case of a NW, the referent ZB GaAs NW segment has to have the same diameter and orientation as the ZB GaAsSb segment, and the EDX point analysis needs to be performed at the uniformly thick central region of the NW. Also, it is important that the NW is tilted off a major zone to avoid the channelling effects and crystal dependent variation in absorption [70,76]. Then, the As concentration, $0.5 - x$, in GaAsSb is determined using:

$$\frac{0.5}{0.5 - x} = k_{\mathrm{GaAs}} \frac{I_{\mathrm{Ga}}}{I_{\mathrm{As}}} \tag{4.6}$$

where I_{Ga} and I_{As} are number of counts for the ZB GaAsSb segment. The Sb concentration x is obtained straightforwardly. The X-ray counts obey Gaussian statistics and standard deviations and absolute errors can be calculated with this technique.

The most important factor for reliable qualitative and quantitative EDX analysis is collecting a large number of counts (order of 10^7 or higher). However, a small volume of the specimen is excited by the electron beam, and thus small number of X-rays is created, and even smaller number detected due to poor collection efficiency. Therefore, to obtain a large number of counts, the scanning has to be performed for a long period of time, which can induce damage in the specimen and build-up of carbon contamination as well as specimen drift can occur.

4.4 The Scanning Electron Microscope

A SEM operates in principle like a STEM: a probe is formed and scanned over the specimen. The image is formed by integrating the signal for each probe position (pixel). The electron beam energy is much lower than in a TEM, normally in the range of $1 - 30$ keV. The typical signals collected in a SEM (see figure 4.3) are SE, BSE, characteristic and bremmstrahlung X-rays, light (cathodoluminescence). However, a single machine rarely has optimized detectors for all possible signals.

A standard SEM can study bulk samples in SE and BSE mode, and there is no need for electron transparent specimens. In SE mode, secondary electrons created upon de-acceleration of primary electrons, are detected. The SE signal comes from within few tens of nm-s below the surface, because the secondary electrons have low energies and get absorbed by the specimen over a short distance [76]. The SE images are extremely surface sensitive and have a large depth of field, resulting in three-dimensional like, topological appearance. Lowering the voltage or selecting a certain range of SE energies enhances this topological surface contrast. For example, SE imaging is useful to observe NW facets (figure 4.8(a)) and morphology (figure 4.8(b)).

In BSE mode, the elastically backscattered incident electrons form the image. The intensity of the BSE signal depends on the atomic number of the elements present in the specimen [76]. Namely, the higher the atomic number the stronger the backscattering, and thus regions with higher average atomic number appear brighter in the image. BSE imaging in combination with characteristic X-rays, can provide information about the composition and distribution of different elements within the specimen. However, BSE mode is not particularly useful for III-V NWs, due to small difference between the atomic numbers of the constituent elements and somewhat due to small size. The third most important signal are characteristic X-rays and the set-up is similar as described in chapter **4.3.5**. However, as the primary electron energy is much lower in SEM than in TEM, not all possible characteristic X-rays will be excited.

A Hitachi S-5500 S(T)EM (30kV, cold field emission gun) was used in this work. The special feature of this machine is that it can operate in BF and DF STEM mode, and TEM specimens can be used. The collection angle is selected by the height of the detector relative to the specimen since there are no lenses between the specimen and the detector as in a TEM/STEM (see chapter **4.3.4**). 30 kV BF STEM proved to be extremely practical for finding and selecting single NWs for correlated PL-TEM studies. The reasons are many: quick and easy to use, induces no damage to the NWs, has

good resolution and a strong contrast. In addition, for some NW orientations it is possible to distinguish different crystal phases in NWs, for example ZB inserts or SFs in WZ NWs, see figure 4.8(c).

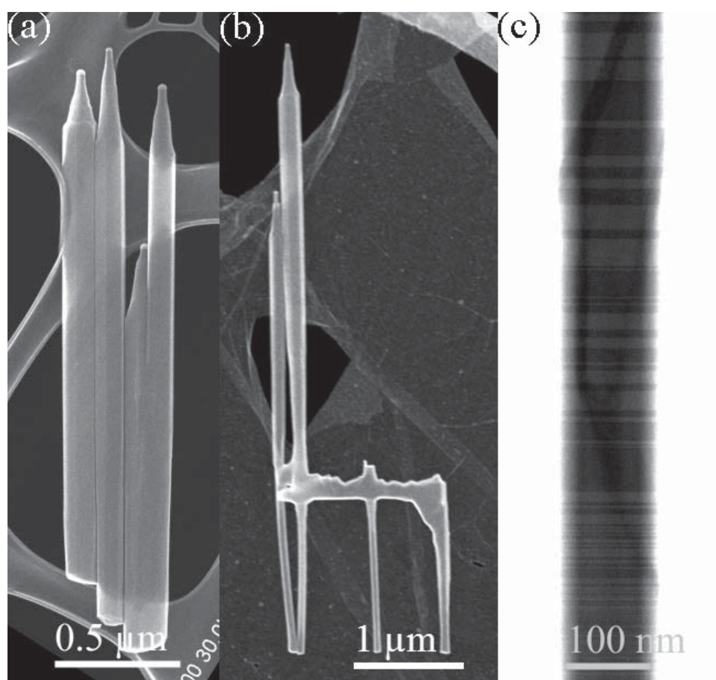

Figure 4.8: WZ GaAs/AlGaAs core-shell NWs: 30 kV SE image of (a) cluster four NWs showing facets (topological contrast) on a holey carbon support; (b) misformed NWs with ”two-headed giraffe” morphology on graphene support; (c) 30 kV BF STEM image of ZB segments and SFs (diffraction contrast) in a WZ NW on a holey carbon support.

Chapter 5

Conclusions and Outlook

5.1 Summary and Conclusions

In this work, a correlated PL-TEM method was developed in order to efficiently study single GaAs-based heterostructured semiconductor NWs and directly correlate their optical and structural properties (paper I). As the selection of single NWs proved to be a challenge for the optical microscopy, the effects of $5-30$ kV S(T)EM on the optical properties were investigated. The PL spectra before and after S(T)EM ($5-30$ kV), and the referent PL spectra of the NWs non-exposed to the electron beam, were compared. The differences between these PL spectra were attributed to slightly different experimental conditions between the PL measurements, such as temperature and orientation of the specimen and the NWs on the sample stage. The $5-30$ keV electrons used for S(T)EM imaging do not alter the optical properties. Therefore, selection of single clean NWs by low voltage S(T)EM, can be carried out before PL. In contrast, the high energy electrons in TEM (200 kV) create defects in the NWs, which cause non-radiative recombinations and deteriorate the optical properties. Hence, TEM must be performed as the last step in a correlated PL-TEM study. Preselection by STEM and TEM characterization after PL, ensure that the NWs with desired structural characteristics have been studied. In general, due to diversity of the NWs within each growth batch, a large number of NWs needs to be examined or studied in detail, to achieve a conclusive correlation between the optical and the structural properties.

The Si grids with a 50 nm thick amorphous SiN support film proved to be practical for a routine PL-TEM characterization. These grids were used throughout this work, and secured in a thin metal holder for safe handling during PL measurements. The drawbacks of Si/SiN grids are their

fragility and the relatively thick support. For example, the thickness of the SiN support reduces the quality of HRTEM imaging for thick NWs (order of 100 nm) and quantitative HAADF STEM study proves to be impossible. On the other hand, an important advantage is that the NWs are easily mapped by SEM/STEM on the nine windows and can be quickly traced both in PL and TEM.

Using the initial correlated PL-TEM results, the optical and structural properties of WZ GaAs/AlGaAs core-shell NWs with axial ZB GaAsSb inserts were directly connected. A qualitative assessment of the NWs based on the number of PL bands in the PL spectra, and the specific structural characteristics, was carried out at first. Depending on which fragment of a NW is sampled, the PL spectra contain bands related to ZB GaAsSb, GaAs and WZ AlGaAs. The AlGaAs PL emission in the $\sim 1.60 - 1.65$ eV range, was found to originate from the axial AlGaAs segment and not from the AlGaAs radial shell. The AlGaAs PL emission has no significance for NW application in general, and is considered as a growth artefact of the heterostructure itself.

The GaAs related PL emission, centred at $\sim$ 1.515 eV, was at first believed to originate from recombinations between the SFs and the surrounding WZ phase, which form type II band alignment (papers I and II). However, the variation in the number of GaAs-related PL peaks and in their energies, observed among WZ GaAs/ZB GaAsSb axially heterostructured NWs in the initial PL-TEM study, was suspicious and needed further investigation. This led into a dedicated study of WZ GaAs/AlGaAs core-shell NWs, which was successful in finding NWs of pure WZ phase and characterizing them with advanced PL and conventional TEM techniques. The WZ GaAs free exciton emission was observed at 1.516 eV at low temperature (15 K). This value is almost coinciding with the ZB free exciton emission energy at 1.515 eV. On the other hand, the room temperature bandgap of WZ GaAs is 1.444 eV $\pm$ 1 meV, which is $\sim$ 20 meV larger than the room temperature bandgap of ZB GaAs. The divergence of the emission energies of WZ and ZB GaAs as temperature is increased, is supported by the unusually long free exciton recombination lifetimes at low temperature. This suggests that the conduction band symmetry in WZ GaAs is Γ_8. In addition, it was found that Au-assisted WZ GaAs NWs can have a high optical quality and PL brightness.

The ZB GaAsSb inserts exhibit type I PL emission for most of the studied NWs (papers I and II). Already at that stage, a large variation in the GaAsSb optical properties was observed in randomly sampled NWs. The question why the variation in GaAsSb PL energy occurs became a sub-

ject of a more detailed study. The Sb concentration, its distribution within and variation among the ZB GaAsSb inserts, were investigated using different methods: EDX analysis, quantitative HAADF STEM and correlated PL-TEM. The large variation of the GaAsSb insert lengths and the Sb concentrations, observed for the same growth conditions in WZ GaAs bare-core and WZ GaAs/AlGaAs core-shell NWs, is thought to be due to a distribution of sizes of Au droplets. The higher the NW growth rate, the longer the GaAsSb insert and the more Sb is incorporated into the insert. This was evidenced by a clear trend of increasing insert length with increasing Sb concentration. The EDX analysis and the quantitative HAADF STEM confirmed that there is a decreasing Sb concentration gradient along the insert towards both insert interfaces. This is probably caused by competition between Sb and As to incorporate into the insert at the beginning of the insert growth, and due to As-Sb exchange at the upper insert interface after the insert growth. In addition, a decreasing radial gradient of the Sb concentration towards the outer surfaces was observed by quantitative HAADF STEM.

The quantitative HAADF STEM provided systematically higher Sb concentrations (by $5 - 8$ %) compared to the EDX results. On the other hand, the results from quantitative HAADF STEM were in agreement with the Sb concentrations calculated from the insert PL emission energies using an empirical model for unstrained bulk GaAsSb. To conclude, the Sb concentrations obtained with these two methods are more reliable than the EDX results. The automatic EDX quantification clearly underestimates the Sb concentrations in ZB GaAsSb inserts in WZ GaAs NWs.

The ground state energy of the GaAsSb PL emission was found to decrease with the increase of the Sb concentration. The structural defects in the WZ GaAs core and the strain within the insert appear to have negligible effect on the GaAsSb PL emission. On the other hand, the Sb concentration gradient has an effect on the GaAsSb related PL emission, inducing both type I and type II transitions within the ZB GaAsSb insert. The type II transitions originate from recombinations of holes in the valence band of the central region of the insert (ZB GaAsSb), and electrons in the conduction band in the regions close to the insert interfaces (ZB GaAs), due to the decreasing Sb concentration towards the interfaces. The type I transitions within the central Sb-richest region of insert dominate in the insert related PL emission.

At the end, it is worth mentioning that not all correlated PL-TEM studies carried out in the course of this work, resulted in a conclusive correlation between the optical and the structural properties of the NWs. The basic PL

and TEM characterization proved to be insufficient for a better understanding of the inherently complex heterostructured NWs and consequently their complex optical properties. Examples of such studies are WZ GaAs inserts in WZ AlGaAs NWs or WZ GaAs/GaAsSb core-shell NWs. In both cases, understanding how these NW heterostructures actually grow and further growth optimisation are necessary before any fundamental questions can be studied. Once a homogeneous batch with desired optical and structural characteristics is achieved, the correlated PL-TEM becomes useful. Of course, the other approach is to hunt for a NW with wanted optical properties and discard many NWs to find one such. To conclude, to study fundamental questions related to a complex NW heterostructure, a combination of different advanced PL and (S)TEM techniques as well as good growth quality are required.

To summarize, the main conclusions of the entire work are:

- An efficient correlated PL-TEM method was developed.
- Conventional TEM studies provided a deeper insight into the structural characteristics of GaAs-based heterostructured semiconductor NWs.
- Fundamental optical properties of WZ GaAs were investigated on a single NW level, and the values for low temperature free exciton energy and room temperature bandgap were obtained.
- ZB GaAsSb inserts in WZ GaAs NWs proved to be more complex than expected: the Sb concentration variation among the inserts, and a decreasing Sb concentration gradient towards the insert interfaces were observed, and this was correlated with the insert lengths and the PL emission energies.

5.2 Outlook

Further development of the PL-TEM method with thinner support films and less fragile TEM grids is an important step for future research. The choice of the TEM grid determines the possibilities and limitations for a correlated PL-TEM study. Utilizing the advanced (S)TEM techniques available on the state-of-the-art electron microscopes works best for extremely thin supports (specimens). To achieve good image quality for NWs which are relatively thick themselves (in the order of 100 nm), the support film has to be as thin as possible. Hence, the Cu/graphene grids (2000 mesh) are next to be tested

for this method. The advantages of these grids are the thinnest possible support, flexibility and easy handling. Moreover, the graphene enables the best possible quality of (S)TEM characterization. The challenge in this case is to map the single NWs by low voltage STEM and trace them back in PL and TEM. This is ongoing work and some progress into this direction has already been achieved. The graphene grids prove to be promising for the future PL-TEM studies within NW projects and in a broader perspective of nanostructured opto-electronic materials.

Another aspect of a correlated PL-TEM study is how efficiently the experimental work is divided between the participants within the project. A possible approach is that one person performs the complete study, which is advantage when a well defined problem needs to be studied on a homogeneously grown NW heterostructure. However, this might not be quick, given the time needed to analyse both PL and TEM results. A more suitable approach is one PL and one TEM person with possibility of more support on the experimental side which is the focus of the work. What needs to be emphasized is that for a successful correlated study, good communication and cooperation are as crucial factors as defining the project and planning the experiments systematically.

Correlated PL-TEM can become a basis for an extended study of NWs or in general, a nanostructured opto-electronic material. For profound understanding of the optical properties of structurally or compositionally more complex heterostructured NWs, advanced (S)TEM techniques need to be included into the basic PL-TEM method. This can include for example: quantitative HAADF STEM (on Cu/graphene grids), strain analysis which is possible on aberration corrected TEMs, electron energy loss spectroscopy, energy filtered TEM, and EDX with a more advanced detection system. In addition, it would be useful to begin a correlated study with a low voltage TEM. In this case, the exact threshold voltage for the irreversible NW damage by electron beam needs to be determined. In such a way, the NWs would remain optically active, but can be preselected based on the desired crystal phases or defect configuration.

On the PL side, combining different techniques, such as polarization-resolved, time-resolved and magneto-PL, is useful for a meaningful study. Depending on the focus of the study, other experimental techniques where TEM specimens are suitable, can be included in the method, for example micro-Raman scattering spectroscopy, cathodoluminescence, photocurrent characterization, scanning near-field optical microscopy, atomic force microscopy, scanning tunneling microscopy.

Quantum confined or strained axial inserts, axial heterostructures with sharp interfaces between different segments, and multiple core-shell NWs, for example, could become important in the future work, both from fundamental and applications perspectives. Assuming that a more precise control of the Sb concentration is achieved, ZB GaAsSb inserts in WZ or ZB GaAs NWs would remain a fundamentally interesting topic. For example, the effect of the Sb concentration ($0-100$ %) on the optical transitions within the insert, and between the insert and the surrounding core could be studied. In this case, strain analysis within the inserts would be extremely useful to understand how the insert PL emission and the band alignments are affected by the Sb concentration throughout the whole range of concentrations. Here, GaAs crystal phase could be WZ or ZB on either side of the insert, which can be achieved with self-catalyzed NW growth. Different combinations of crystal phases and systematically varied Sb concentration would provide a better insight into the optical behaviour of such NW heterostructures.

Quantum confined WZ GaAs inserts in WZ AlGaAs NWs are an intriguing topic to return to. Once the growth is optimized to such degree that insert size and crystal phase can be precisely controlled, and the interfaces are compositionally sharp, studying the insert size effect on WZ GaAs optical properties by advanced correlated PL-TEM would be possible. In this case, quantitative HAADF STEM would be the dominant technique on the TEM side, to determine the insert size and the Al concentration in the surrounding AlGaAs. In addition, some numerical work would be necessary to determine the energies and the number of possible PL transitions within the insert as a function of the insert size. Similar study could be carried out for the ZB GaAsSb inserts in GaAs NWs.

For solar cell application, the growth of GaAs-based heterostructured NWs has evolved towards self-catalysed growth. Growth optimisation of self-catalysed GaAs-based NWs on Si, patterned Si or graphene substrates, will be significant part of the future work within the NW project. Doped multiple core-shell NWs will play the main role in a solar cell. Thorough investigation of the fundamental properties of these novel heterostructured NWs will be highly demanded when the realization of a solar cell becomes in sight. Thus, the correlated PL-TEM method, basic or advanced, remains of crucial importance to realize a NW-based solar cell.

References

[1] A. I. Hochbaum and P. Yang. Semiconductor Nanowires for Energy Conversion. *Chemical Reviews*, 110(1):527–546, 2010.

[2] P. Yang, R. Yan, and M. Fardy. Semiconductor nanowire: What's next? *Nano Letters*, 10(5):1529–1536, 2010.

[3] B. Tian, X. Zheng, T. J. Kempa, Y. Fang, N. Yu, G. Yu, J. Huang, and C. M. Lieber. Coaxial silicon nanowires as solar cells and nano-electronic power sources. *Nature Letters*, 449:885–890, 2007.

[4] L. Tsakalakos, J. Balch, J. Fronheiser, B. A. Korevaar, O. Sulima, and J. Rand. Silicon nanowire solar cells. *Applied Physics Letters*, 91(23):233117, 2007.

[5] E. Garnett and P. Yang. Light Trapping in Silicon Nanowire Solar Cells. *Nano Letters*, 10(3):1082–1087, 2010.

[6] J. C. Johnson, H. -J. Choi, K. P. Knutsen, R. D. Schaller, P. Yang, and R. J. Saykally. Single gallium nitride nanowire lasers. *Nature Materials*, 1:106–110, 2002.

[7] X. Duan, Y. Huang, R. Agarwal, and C. M. Lieber. Single-nanowire electrically driven lasers. *Nature*, 421:241–245, 2003.

[8] B. Hua, J. Motohisa, Y. Kobayashi, S. Hara, and T. Fukui. Single GaAs/GaAsP Coaxial Core-Shell Nanowire Lasers. *Nano Letters*, 9(1):112–116, 2009.

[9] M. A. Zimmler, F. Capasso, S. Müler, and C. Ronning. Optically pumped nanowire lasers: invited review. *Semiconductor Science and Technology*, 25:024001, 2010.

[10] Y. Cui, X. Duan, J. Hu, and C. M. Lieber. Doping and Electrical Transport in Silicon Nanowires. *Journal of Physical Chemistry B*, 104(22):5213–5216, 2000.

[11] Y. Huang, X. Duan, and C. M. Lieber. Nanowires for Integrated Multicolor Nanophotonics. *Small*, 1(1):142–147, 2005.

[12] M. Yu, Y. -Z. Long, B. Sun, and Z. Fan. Recent advances in solar cells based on one-dimensional nanostructure arrays. *Nanoscale*, 4:2783–2796, 2012.

[13] B. Bauer, A. Rudolph, M. Soda, A. Fontcuberta i Morral, J. Zweck, D. Schuh, and E. Reiger. Position controlled self-catalyzed growth of GaAs nanowires by molecular beam epitaxy. *Nanotechnology*, 21(43):435601, 2010.

[14] A. M. Munshi, D. L. Dheeraj, V. T. Fauske, D. C. Kim, A. T. J. van Helvoort, B. O. Fimland, and H. Weman. Vertically Aligned GaAs Nanowires on Graphite and Few-Layer Graphene: Generic Model and Epitaxial Growth. *Nano Letters*, 12(9):4570–4576, 2012.

[15] B. M. Kayes, H. A. Atwater, and N. S. Lewis. Comparison of the device physics principles of planar and radial p-n junction nanorod solar cells. *Journal of Applied Physics*, 97(11):114302, 2005.

[16] H. J. Fan, P. Werner, and M. Zacharias. Semiconductor Nanowires: From Self-Organization to Patterned Growth. *Small*, 2(6):700–717, 2006.

[17] I. Vurgaftman, J. R. Meyer, and L. R. Ram-Mohan. Band parameters for III-V compound semiconductors and their alloys. *Journal of Applied Physics*, 89(11):5815–5875, 2001.

[18] A. De and C. E. Pryor. Predicted band structures of III-V semiconductors in the wurtzite phase. *Physical Review B*, 81(15):155210, 2010.

[19] D. L. Dheeraj, G. Patriarche, L. Largeau, H. L. Zhou, A. T. J. van Helvoort, F. Glas, J. C. Harmand, B. O. Fimland, and H. Weman. Zinc blende GaAsSb nanowires grown by molecular beam epitaxy. *Nanotechnology*, 19(27):275605, 2008.

[20] D. L. Dheeraj, G. Patriarche, H. Zhou, T. B. Hoang, A. F. Moses, S. Grønsberg, A. T. J. van Helvoort, B. O. Fimland, and H. Weman. Growth and Characterization of Wurtzite GaAs Nanowires with Defect-free Zinc Blende GaAsSb Inserts. *Nano Letters*, 8(12):4459–4463, 2008.

[21] H. J. Joyce, J. Wong-Leung, Q. Gao, H. Hoe Tan, and C. Jagadish. Phase Perfection in Zinc Blende and Wurtzite III-V Nanowires Using Basic Growth Parameters. *Nano Letters*, 10(3):908–915, 2010.

[22] K. A. Dick, P. Caroff, J. Bolinsson, M. E. Messing, J. Johansson, K. Deppert, L. R. Wallenberg, and L. Samuelson. Control of III-V nanowire crystal structure by growth parameter tuning. *Semiconductor Science and Technology*, 25:024009, 2010.

[23] D. L. Dheeraj. Growth and structural characterization of III-V nanowires grown by molecular beam epitaxy. *Doctoral theses at NTNU, 2010:190, NTNU-trykk*, 2010.

[24] H. J. Joyce, Q. Gao, H. Hoe Tan, C. Jagadish, Y. Kim, J. Zou, L. M. Smith, H. E. Jackson, J. M. Yarrison-Rice, P. Parkinson, and M. B. Johnston. III-V semiconductor nanowires for optoelectronic device applications. *Progress in Quantum Electronics*, 35:23–75, 2011.

[25] R. E. Algra, M. A. Verheijen, M. T. Borgström, L. F. Feiner, G. Immink, W. J. P. van Enckevort, E. Vlieg, and E. P. A. M. Bakkers. Twinning superlattices in indium phosphide nanowires. *Nature Letters*, 456:369–372, 2008.

[26] P. Caroff, K. A. Dick, J. Johansson, M. E. Messing, K. Deppert, and L. Samuelson. Controlled polytypic and twin-plane superlattices in III-V nanowires. *Nature Nanotechnology*, 4:50–55, 2009.

[27] K. A. Dick, C. Thelander, L. Samuelson, and P. Caroff. Crystal Phase Engineering in Single InAs Nanowires. *Nano Letters*, 10(9):3494–3499, 2010.

[28] D. L. Dheeraj, A. M. Munshi, M. Scheffler, A. T. J. van Helvoort, H. Weman, and B. O. Fimland. Controlling Crystal Phases in GaAs Nanowires Grown by Au-Assisted Molecular Beam Epitaxy. *Submitted to Nanotechnology*, 06/07/2012.

[29] F. Jabeen, G. Patriarche, F. Glas, and J. C. Harmand. $GaP/GaAs_{1-x}P_x$ nanowires fabricated with modulated fluxes: A step towards the realization of superlattices in a single nanowire. *Journal of Crystal Growth*, 323:293–296, 2011.

[30] M. C. Plante and R. R. LaPierre. Au-assisted growth of GaAs nanowires by gas source molecular beam epitaxy: Tapering, sidewall

faceting and crystal structure. *Journal of Crystal Growth*, 310:356–363, 2008.

[31] X. Tao, K. A. Dick, S. Plissard, T. H. Nguyen, Y. Makoudi, M. Berthe, J. P. Nys, X. Wallart, B. Grandidier, and P. Caroff. Faceting, composition and crystal phase evolution in III-V antimonide nanowire heterostructures revealed by combining microscopy techniques. *Nanotechnology*, 23(9):095702, 2012.

[32] S. Lehmann, D. Jacobsson, K. Deppert, and K. A. Dick. High crystal quality wurtzite-zinc blende heterostructures in metal-organic vapor phase epitaxy-grown GaAs nanowires. *Nano Research*, 5(7):470–476, 2012.

[33] A. D. Prins, D. J. Dunstan, J. D. Lambkin, E. P. O'Reilly, A. R. Adams, R. Pritchard, W. S. Truscott, and K. E. Singer. Evidence of type-I band offsets in strained $GaAs_{1-x}Sb_x$/GaAs quantum wells from high-pressure photoluminescence. *Physical Review B*, 47(4):2191–2196, 1993.

[34] G. Liu, S. L. Chuang, and S. H. Park. Optical gain of strained GaAsSb/GaAs quantum-well lasers: A self-consistent approach. *Journal of Applied Physics*, 88(10):5554–5561, 2000.

[35] R. Teissier, D. Sicault, J. C. Harmand, G. Ungaro, G. Le Roux, and L. Largeau. Temperature-dependent valence band offset and bandgap energies of pseudomorphic GaAsSb on GaAs. *Journal of Applied Physics*, 89(10):5473–5477, 2001.

[36] J. B. Wang, S. R. Johnson, S. A. Chaparro, D. Ding, Y. Cao, Y. G. Sadofyev, Y. H. Zhang, J. A. Gupta, and C. Z. Guo. Band edge alignment of pseudomorphic $GaAs_{1-y}Sb_y$ on GaAs. *Physical Review B*, 70(19):195339, 2004.

[37] Y. G. Sadofyev and N. Samal. Photoluminescence and Band Alignment of Strained GaAsSb/GaAs QW Structures Grown by MBE on GaAs. *Materials*, 3:1497-1508, 2010.

[38] M. Baranowski, M. Syperek, R. Kudrawiec, J. Misiewicz, J. A. Gupta, X. Wu, and R. Wang. Carrier dynamics between delocalized and localized states in type-II GaAsSb/GaAs quantum wells. Applied Physics Letters, 98(6):061910, 2011.

[39] J. Bao, D. C. Bell, F. Capasso, J. B. Wagner, T. Mårtensson, J. Trägårdh, and L. Samuelson. Optical Properties of Rotationally Twinned InP Nanowire Heterostructures. *Nano Letters*, 8(3):836–841, 2008.

[40] V. Zwiller, N. Akopian, M. van Weert, M. van Kouwen, U. Perinetti, L. Kouwenhoven, R. Algra, J. Gómez Rivas, E. Bakkers, G. Patriarche, L. Liu, J. -C. Harmand, Y. Kobayashi, and J. Motohisa. Optics with single nanowires. *Comptes Rendus Physique*, 9:804–815, 2008.

[41] M. Heiss, S. Conesa-Boj, J. Ren, H. -H. Tseng, A. Gali, A. Rudolph, E. Uccelli, F. Peiró, J. R. Morante, D. Schuh, E. Reiger, E. Kaxiras, J. Arbiol, and A. Fontcuberta i Morral. Direct correlation of crystal structure and optical properties in wurtzite/zinc-blende GaAs nanowire heterostructures. *Physical Review B*, 83(4):045303, 2011.

[42] M. Murayama and T. Nakayama. Chemical trend of band offsets at wurtzite/zinc-blende heterocrystalline semiconductor interfaces. *Physical Review B*, 49(7):4710–4724, 1994.

[43] G. D. Gilliland. Photoluminescence spectroscopy of crystalline semiconductors. *Materials Science and Engineering: Reports*, 18:99–400, 1997.

[44] T. B. Hoang, A. F. Moses, H. L. Zhou, D. L. Dheeraj, B. O. Fimland, and H. Weman. Observation of free exciton photoluminescence emission from single wurtzite GaAs nanowires. *Applied Physics Letters*, 94(13):133105, 2009.

[45] U. Jahn, J. Lähnemann, C. Pfüller, O. Brandt, S. Breuer, B. Jenichen, M. Ramsteiner, L. Geelhaar, and H. Riechert. Luminescence of GaAs nanowires consisting of wurtzite and zinc-blende segments. *Physical Review B*, 85(4):045323, 2012.

[46] B. Ketterer, M. Heiss, M. J. Livrozet, A. Rudolph, E. Reiger, and A. Fontcuberta i Morral. Determination of the band gap and the split-off band in wurtzite GaAs using Raman and photoluminescence excitation spectroscopy. *Physical Review B*, 83(12):125307, 2011.

[47] S. Breuer, C. Pfüller, T. Flissikowski, O. Brandt, H. T. Grahn, L. Geelhaar, and H. Riechert. Suitability of Au- and Self-Assisted GaAs Nanowires for Optoelectronic Applications. *Nano Letters*, 11(3):1276-1279, 2011.

[48] B. Ketterer, M. Heiss, E. Uccelli, J. Arbiol, and A. Fontcuberta i Morral. Untangling the Electronic Band Structure of Wurtzite GaAs Nanowires by Resonant Raman Spectroscopy. *ACS Nano*, 5(9):7585–7592, 2011.

[49] D. L. Dheeraj, G. Patriarche, H. Zhou, J. C. Harmand, H. Weman, and B. O. Fimland. Growth and structural characterization of GaAs/GaAsSb axial heterostructured nanowires. *Journal of Crystal Growth*, 311:1847–1850, 2009.

[50] T. B. Hoang, A. F. Moses, L. Ahtapodov, H. Zhou, D. L. Dheeraj, A. T. J. van Helvoort, B. O. Fimland, and H. Weman. Engineering Parallel and Perpendicular Polarized Photoluminescence from a Single Semiconductor Nanowire by Crystal Phase Control. *Nano Letters*, 10(8):2927–2933, 2010.

[51] H. Kauko, T. Grieb, R. Bjørge, M. Schowalter, A. M. Munshi, H. Weman, A. Rosenauer, and A. T. J. van Helvoort. Compositional characterization of GaAs/GaAsSb nanowires by quantitative HAADF-STEM. *Micron*, dx.doi.org/10.1016/j.micron.2012.07.002, 2012.

[52] R. S. Wagner and W. C. Ellis. Vapor-liquid-solid mechanism of single crystal growth. *Applied Physics Letters*, 4(5):89–90, 1964.

[53] H. L. Zhou, T. B. Hoang, D. L. Dheeraj, A. T. J. van Helvoort, L. Liu, J. C. Harmand, B. O. Fimland, and H. Weman. Wurtzite GaAs/AlGaAs core-shell nanowires grown by molecular beam epitaxy. *Nanotechnology*, 20(41):415701, 2009.

[54] J. C. Harmand, G. Patriarche, N. Péré-Laperne, M. N. Mérat-Combes, L. Travers, and F. Glas. Analysis of vapor-liquid-solid mechanism in Au-assisted GaAs nanowire growth. *Applied Physics Letters*, 87(20):203101, 2005.

[55] F. Glas, J. C. Harmand, and G. Patriarche. Why does wurtzite form in nanowires of III-V zinc blende semiconductors? *Physical Review Letters*, 99(14):146101, 2007.

[56] V. G. Dubrovskii and N. V. Sibirev. General form of the dependences of nanowire growth rate on the nanowire radius. *Journal of Crystal Growth*, 304:504–513, 2007.

[57] A. T. J. van Helvoort, D. L. Dheeraj, H. Zhou, S. Grønsberg, G. Patriarche, B. O. Fimland, and H. Weman. Dark field transmission electron

microscopy techniques for structural characterization of semiconductor nanowire heterostructures. *Journal of Physics: Conference Series*, 241:012084, 2010.

[58] L. J. Lauhon, M. S. Gudiksen, and C. M. Lieber. Semiconductor nanowire heterostructures. *Philosophical Transactions of the Royal Society A: Mathematical, physical and engineering sciences*, 362:1247–1260, 2004.

[59] C. C. Chang, C. Y. Chi, M. Yao, N. Huang, C. C. Chen, J. Theiss, A. W. Bushmaker, S. LaLumondiere, T. W. Yeh, M. L. Povinelli, C. Zhou, P. D. Dapkus, and S. B. Cronin. Electrical and Optical Characterization of Surface Passivation in GaAs Nanowires. *Nano Letters*, 12(9):4484-4489, 2012.

[60] C. Y. Yeh, Z. W. Lu, S. Froyen, and A. Zunger. Zinc-blende – wurtzite polytypism in semiconductors. *Physical Review B*, 46(16):10086–10097, 1992.

[61] P. Stadelmann. Simulation of diffraction patterns and high resolution images using jems. *CIME-EPFL, Station 12, CH-1015 Lausanne, Switzerland*, June 17, 2008.

[62] A. Kelly and K. M. Knowles. Crystallography and Crystal defects. *A John Wiley and Sons, Ltd., Publication*, 2nd, 2012.

[63] J. P. Boulanger and R. R. LaPierre. Polytype formation in GaAs/GaP axial nanowire heterostructures. *Journal of Crystal Growth*, 332:21–26, 2011.

[64] J. Johansson, J. Bolinsson, M. Ek, P. Caroff, and K. A. Dick. Combinatorial Approaches to Understanding Polytypism in III-V Nanowires. *ACS Nano*, 6(7):6142–6149, 2012.

[65] H. E. Ruda and A. Shik. Polarization-sensitive optical phenomena in semiconducting and metallic nanowires. *Physical Review B*, 72(11):115308, 2005.

[66] G. Dresselhaus. Optical Absorption Band Edge in Anisotropic Crystals. *Physical Review*, 105(1):135–138, 1957.

[67] J. L. Birman. Some Selection Rules for Band-Band Transitions in Wurtzite Structure. *Physical Review*, 114(6):1490–1492, 1959.

[68] K. A. Dick, J. Bolinsson, B. M. Borg, and J. Johansson. Controlling the Abruptness of Axial Heterojunctions in III-V Nanowires: Beyond the Reservoir Effect. *Nano Letters*, 12(6):3200–3206, 2012.

[69] P. Hirsh, A. Howie, R. Nicholson, D. W. Pashley, and M. J. Whelan. Electron Microscopy of Thin Crystals. *Robert E. Krieger Publishing CO., INC.* 2nd revised edition, 1977.

[70] C. J. Humphreys. The scattering of fast electrons by crystals. *Reports on Progress in Physics*, 42(11):1825–1887, 1979.

[71] N. W. Ashcroft and N. D. Mermin. Solid State Physics. *Harcourt Brace College Publishers*, 1975.

[72] M. I. McMahon and R. J. Nelmes. Observation of a wurtzite form of gallium arsenide. *Physical Review Letters*, 95(21):215505, 2005.

[73] J. R. Arthur. Molecular beam epitaxy. *Surface Science*, 500:189–217, 2002.

[74] W. Y. Liang. Excitons. *Physics Education*, 5(4):226–228, 1970.

[75] P. N. Prasad. Nanophotonics. *John Wiley and Sons, INC.*, 2004.

[76] D. B. Williams and C. B. Carter. Transmission Electron Microscopy: A Textbook for Materials Science. *Springer*, 2nd edition, 2009.

[77] S. J. Pennycook. Structure Determination Through Z-Contrast Microscopy. *Oak Ridge National Laboratory*, PO Box 2008, Oak Ridge TN 37830-6030 USA.

Part II

Papers

Chapter 6

Correlated micro-photoluminescence and electron microscopy studies of the same individual heterostructured semiconductor NWs

Nanotechnology **22**(32) (2011) 325707

Nanotechnology **22** (2011) 325707 (9pp) doi:10.1088/0957-4484/22/32/325707

Correlated micro-photoluminescence and electron microscopy studies of the same individual heterostructured semiconductor nanowires

J Todorovic[1], A F Moses[2], T Karlberg[2], P Olk[2], D L Dheeraj[2], B O Fimland[2], H Weman[2] and A T J van Helvoort[1]

[1] Department of Physics, Norwegian University of Science and Technology, NO-7491, Trondheim, Norway
[2] Department of Electronics and Telecommunications, Norwegian University of Science and Technology, NO-7491, Trondheim, Norway

E-mail: a.helvoort@ntnu.no

Received 18 February 2011, in final form 10 June 2011
Published 20 July 2011
Online at stacks.iop.org/Nano/22/325707

Abstract
To correlate optical properties to structural characteristics, we developed a robust strategy for characterizing the same individual heterostructured semiconductor nanowires (NWs) by alternating low temperature micro-photoluminescence (μ-PL), low voltage scanning (transmission) electron microscopy and conventional transmission electron microscopy. The NWs used in this work were wurtzite GaAs core with zinc blende GaAsSb axial insert and AlGaAs radial shell grown by molecular beam epitaxy. The series of experiments demonstrated that high energy (200 kV) electrons are detrimental for the optical properties, whereas medium energy (5–30 kV) electrons do not affect the PL response. Thus, such medium energy electrons can be used to select NWs for correlated optical–structural studies prior to μ-PL or in NW device processing. The correlation between the three main μ-PL bands and crystal phases of different compositions, present in this heterostructure, is demonstrated for selected NWs. The positions where a NW fractures during specimen preparation can considerably affect the PL spectra of the NW. The effects of crystal-phase variations and lattice defects on the optical properties are discussed. The established strategy can be applied to other nanosized electro-optical materials, and other characterization tools can be incorporated into this routine.

(Some figures in this article are in colour only in the electronic version)

1. Introduction

The current interest in the synthesis and properties of semiconductor heterostructured nanowires (NWs) is staggering [1]. NWs have promising properties and offer vast freedom of design for nanodevice applications such as solar cells [2, 3] and lasers [4, 5]. For successful implementation, the quality and uniformity of the NWs should be high. Therefore, optimization of synthesis and accurate and complete characterization of the physical properties and structure of the NWs are required.

The electro-optical properties of NWs are intricately connected with the heterostructure design of NWs, composition variation, crystal structure and lattice defects. Moreover, NWs from the same batch may have different lengths and diameters, as well as variations in crystal phases, distribution of defects and composition along their length [6]. Such variations might affect the overall optical properties [7, 8]. Because of possible differences between NWs from the same batch, a large number of individual NWs have to be studied to gain reliable insight in the property–structure relation. For heterostructured III–V NWs, micro-photoluminescence (μ-PL) is one of the

 © 2011 IOP Publishing Ltd Printed in the UK & the USA

most applied optical characterization tools [9, 10]. Supporting detailed structural characterization of other single NWs from the same batch is often obtained by transmission electron microscopy (TEM) (see for example [7, 10–12]). Due to the possible variations between NWs within one batch, uncorrelated characterization gives at best information about average optical and structural properties of a NW batch.

A necessary step towards accurate characterization of NWs is correlation of the μ-PL spectra of particular NWs with their individual structural characteristics. To draw meaningful conclusions about the band gaps, valence and conduction band alignments, quantum confinement effects, and allowed carrier recombinations for a particular NW heterostructure, the optical and structural characterization have to be performed on the same single NW. To the best of our knowledge, there are just a few studies reported that have achieved PL and TEM characterization of the very same single NW [8, 13, 14]. Correlated PL–TEM experiments are not routinely applied on NWs or other nanostructured materials. Optical characterization combined with scanning electron microscopy (SEM) has recently been reported for CdSe/CdS nanocrystals [15]. Such correlated PL–SEM provides useful information on how the morphology of a nanostructured material affects the optical properties. In that particular study, correlated PL–TEM failed due to poor thermal contact resulting in insufficient cooling of the nanorods. *In situ* optical studies of III–V NWs in electron microscopes have been demonstrated by cathodoluminescence (CL) in an SEM [16, 17] and a dedicated scanning TEM (STEM) [18].

In the μ-PL setup, due to the limited spatial resolution of light imaging, it is uncertain whether or not the nano-objects selected for the measurements are single NWs. This initial uncertainty has implications on the interpretation of the μ-PL spectra. Performing SEM or transmission electron microscopy (TEM, STEM) before μ-PL would allow the selection of single (i.e. no agglomerates of NWs) and uncontaminated (i.e. without any other potential luminescing source within the probe diameter of μ-PL) NWs. However, the medium (1–30 kV) to high (100–300 kV) energy electrons used in electron microscopy might alter the material and hence affect the μ-PL response. For bulk zinc blende (ZB) GaAs, there are studies, for example [19], analysing 0.1–1 MeV electron irradiation-induced defects in the crystal lattice. In contrast, no such studies have been reported for semiconductor NWs.

In this work, we present a robust measurement procedure for studying both the optical properties by μ-PL and the structural characteristics by electron microscopy of the same NW for a significant number of individual single NWs per batch. The NWs used as test objects had a wurtzite (WZ) GaAs core with a ZB GaAsSb insert for the first batch, with the addition of an AlGaAs radial shell for the second batch [6, 20, 21]. TEM (200 kV) and S(T)EM (5–30 kV), under different illumination conditions, were systematically used to give insight into whether accelerated electrons can affect the optical properties. An efficient procedure for selecting and tracing single NWs has been established. Several NWs from the obtained data set were selected and their optical properties were compared and correlated with unique structural characteristics.

2. Experimental details

To develop and test a correlated PL–TEM strategy for characterization of single NWs, axially and radially heterostructured GaAs-based NWs were used. These NWs were grown on GaAs(111)B substrates by Au-assisted molecular beam epitaxy (MBE). The complete growth procedure is described elsewhere [21, 22]. The NWs consisted of WZ GaAs core with ZB GaAsSb insert, with growth interruption performed after the insert [20], in the first batch (specimen C1, core only). For the GaAsSb insert growth, the fluxes of As_4 and Sb_2 were 6×10^{-6} and 6×10^{-7} Torr respectively. In the second batch (specimens CS1 and CS2, core–shell) the NWs had in addition an $Al_{0.3}Ga_{0.7}As$ radial shell and a thin GaAs capping layer, both with the same crystal structure as the core [21].

The TEM specimens were prepared by dispersing the as-grown substrates in isopropanol using an ultrasonic bath. A few drops of the dispersions were transferred onto the TEM grids. The grids were 200 μm thick Si frames with nine windows of 100 μm $\times$ 100 μm, entirely covered by a 50 nm thick amorphous silicon nitride film (ThinWindows Inc.). For μ-PL measurements, each grid was secured in between two molybdenum washers which were sealed by silver paint. This construction is called the 'holder' hereafter. The washers, each with a central hole (2 mm in diameter), were suitable for the cold finger in the μ-PL setup. By conventional optical microscopy, in transmission or reflection mode, three candidate NWs were selected in each window. The term 'candidate NW' designates an object, desirably a single NW, selected by optical microscopy for PL–TEM study. The grids were taken out from the holders prior to each electron microscopy experiment.

μ-PL was performed in a Janis ST-500 cryostat with a cold finger at $\sim$10 K, using continuous laser excitation at the wavelength of 532 nm. The power density at the specimen was varied from 0.25 to about 50 W cm^{-2}. The focal diameter of the PL excitation beam was estimated to be 5 μm. A Horiba Jobin Yvon iHR500 spectrometer with a 300 grooves mm^{-1} grating and an Andor Newton^{EM} Si electron multiplying charge coupled device (EMCCD) was used for detection. The spectral resolution of the system is about 200 μeV. All the μ-PL experiments were carried out under similar conditions.

Scanning (transmission) electron microscopy (S(T)EM) imaging was performed on a Hitachi S-5500. A single tilt holder was used. For specimen CS2, all candidate NWs within each of the six selected windows were illuminated with electrons of one specific acceleration voltage, which was varied in steps of 5 kV from 5 to 30 kV. For 5–10–15 kV, secondary electron imaging was used, whereas for 20–25–30 kV, bright field (BF) STEM imaging was used. In S(T)EM two NWs per window received a dose of approximately 10^8 e^- nm^{-2} and one NW a dose of approximately 5×10^8 e^- nm^{-2}. The three remaining windows were not illuminated by electrons in S(T)EM or TEM and served for referent μ-PL measurements. The unexposed NWs within these three windows are designated as referent NWs in the rest of the text.

The crystal structure and defects of the NWs were analysed on a Philips CM30 (LaB_6) TEM operating at 200 kV.

Table 1. Overview of all experimental procedures for the three specimens.

Specimen	Experimental procedure	Number of studied candidate NWs	Single NWs
C1	PL–TEM–PL	7	0
CS1	PL–TEM–PL	7	5
CS2	PL–S(T)EM–PL–TEM–PL[a]	18	11
	PL–PL–PL–30 kV STEM[b]	9	8

[a] Six windows were illuminated in S(T)EM as described above.

[b] The remaining three windows were not illuminated (either in S(T)EM or TEM) and the corresponding candidate NWs are called referent NWs. The referent NWs were imaged in the final STEM experiment at 30 kV.

A double tilt holder was used. The techniques used were bright field (BF), dark field (DF), selected area electron diffraction (SAED) and lattice imaging (HREM). Images were taken on a 1k CCD (Tietz) or on film (scanned in at 600 or 1200 dpi).

μ-PL measurements were performed before and after each electron microscopy study for all three specimens. The experimental sequences are summarized in table 1. For the specimens C1 and CS1, all candidate NWs initially studied by μ-PL were directly examined by TEM (PL–TEM–PL series). For the specimen CS2, 18 NWs (within 6 of 9 windows) were studied in low voltage (5–30 kV) S(T)EM, as described above, after the initial μ-PL, and only these NWs were examined by TEM (PL–S(T)EM–PL–TEM–PL series). All candidate NWs (27) were studied by μ-PL in each experimental session. Finally, the referent NWs were imaged by 30 kV STEM after the last μ-PL in the series.

3. Results

In total, we analysed 32 candidate NWs by μ-PL and TEM (see table 1). TEM and S(T)EM showed that 16 candidate NWs were actually single NWs and had no other possible PL sources within a diameter of at least 5 μm. The other candidate NWs in the PL–TEM data set (specimens C1, CS1 and CS2) were actually clusters of two, three or more NWs. In addition, TEM studies showed that there were suitable single NWs dispersed throughout all three specimens, which were either not observed or selected by optical microscopy. The NWs from the specimen C1 exhibited weak PL response as they had no passivating AlGaAs shell. The core–shell NWs exhibited much stronger PL response. The success rate of single NW selection was higher for the specimens CS1 and CS2 (table 1).

3.1. Optical, low voltage S(T)EM and TEM imaging

As an example of specimen mapping by optical microscopy, a part of the central window in specimen CS2 with a candidate NW, marked by the black arrow, is shown in figure 1(a). For the batch studied here, this NW has representative properties, such as PL response and dimensions, morphology and crystal phases as determined by TEM. The large spots are drying stains containing agglomerated NWs and debris from the substrate, as confirmed by S(T)EM and TEM afterwards. This NW was imaged by BF STEM (25 kV, figure 1(b)), revealing the overall morphology of the NW. In addition, the image shows that there is a small NW (a tip with a gold nanoparticle is marked by the white arrow) protruding from the contamination around the candidate NW. Figure 1(c) is the BF TEM image of the candidate NW tilted on a $\langle 110 \rangle$ zone. The growth direction of the NWs is $[111]_{ZB}/[0001]_{WZ}$. The 'up' direction for a NW is defined as from the substrate towards the tip with the gold particle. The diameter of this 1.98 μm long NW is 114 nm around the GaAsSb insert (marked by black arrows) and it reaches its maximum value of 122 nm approximately 600 nm above the insert. The existence of the small NW, indicated by STEM (figure 1(b)), was confirmed by TEM (figure 1(c)). Furthermore, the BF TEM image suggests that the candidate NW is damaged on the right side at the position where the small NW crosses it (white arrow). As the small NW was almost completely covered by the on-zone candidate NW, its crystal phase could not be determined. Out of 18 candidate NWs in specimen CS2 inspected by S(T)EM, 11 were observed as single NWs with the expected morphology. The TEM images were consistent with the initial observations based on S(T)EM

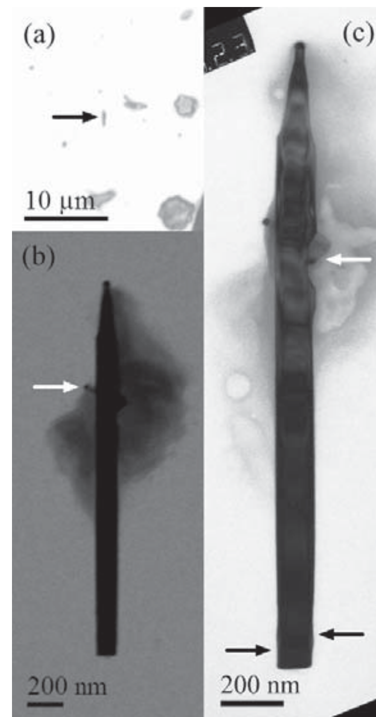

Figure 1. (a) Optical image of an area in the central window of specimen CS2 in which a candidate NW was selected (black arrow). (b) BF STEM image at 25 kV revealing some contamination and a small NW (white arrow) crossing the candidate NW. (c) BF TEM image on a $\langle 110 \rangle$ zone. The lower interface and upper interface of the ZB GaAsSb insert are marked by black arrows. The white arrow in (c) marks the position where the shell is damaged.

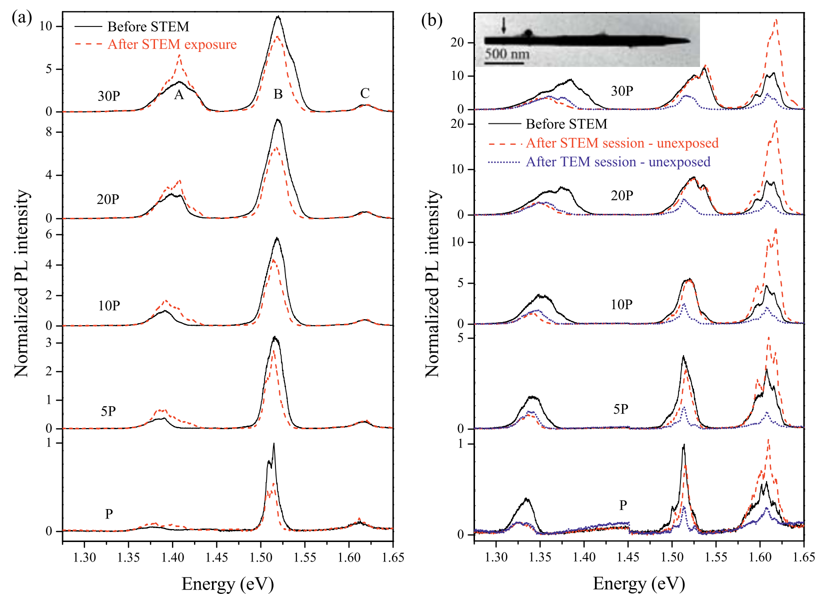

Figure 2. Low temperature (10 K), power dependent PL spectra ($P = 0.5$ W cm^{-2}) of (a) the NW presented in figure 1 before (full black) and after 25 kV STEM (dashed red), (b) a referent NW acquired before (full black), after S(T)EM (dashed red) and after TEM (dotted blue) sessions, during which the NW remained unexposed to electron beams. Inset: 30 kV STEM image taken after the third and final μ-PL experiment. The black arrow marks the position of the GaAsSb insert as determined by diameter variations.

with one exception: a small branching NW was not detected by secondary electron imaging at 15 kV.

3.2. Comparison of initial PL spectra with PL spectra after STEM and TEM studies for exposed and referent NWs

The power dependent PL spectra of the candidate NW shown in figure 1, recorded before and after 25 kV STEM, are presented in figure 2(a). Three characteristic PL bands for this core–shell NW heterostructure (specimens CS1 and CS2) occur in the energy ranges 1.30–1.45 eV, 1.47–1.55 eV and 1.58–1.65 eV and will be referred to as bands A, B and C, respectively. The PL spectra (figure 2(a)) of the candidate NW (figure 1) contain all the three bands. All bands show broadening with increasing excitation power.

For the candidate NW in figure 1, band A is stronger, B weaker, whereas C remains similar, in the PL spectra after STEM compared to the corresponding bands before STEM. As opposed to this, no PL emission could be detected from the candidate NW (figure 1) in the range of 1.25–1.65 eV, even at 150 W cm^{-2}, after the TEM study. After the S(T)EM study, all candidate NWs (exposed and referent) remained optically active (i.e. all initially observed PL bands remained in the spectra) and the PL response was comparable to the PL response before S(T)EM. After the TEM study, very weak or no PL emission in the same range (1.25–1.65 eV) was observed for all the exposed NWs studied here, both with and without AlGaAs shells.

For comparison, figure 2(b) shows all three series of PL spectra for a referent NW, representative by morphology (i.e. length, diameter and tip shape) as determined by STEM. BF STEM at 30 kV (inset of figure 2(b)), performed after the last μ-PL (see table 1), showed that the referent NW was indeed single. The diameter of the NW was 110 nm around the GaAsSb insert and reached a maximum of 130 nm in the upper half of the NW. The NW was 2.6 μm long, hence of similar dimensions and morphology to the representative NW in figure 1. In this case, the PL response after the TEM session was detected and the PL bands were of comparable or lower intensities to before and after STEM. It is seen that band A was stronger in the initial PL spectra than after the STEM and TEM sessions, whereas band C was stronger after the STEM session. For each of the nine referent NWs, the characteristic PL bands, present in the initial PL spectra, were detected in the subsequent two μ-PL experiments as well.

Differences in intensities were observed between the PL spectra before and after S(T)EM for all the candidate NWs (whether exposed to accelerated electrons or not). The energies of the three characteristic A, B, and C bands were nearly identical in the PL spectra before and after S(T)EM at each applied power and for each of the 27 candidate NWs. Random redistribution of intensities of the characteristic bands and small fluctuations within these bands occurred in the PL spectra of all 27 candidate NWs (including the referent NWs). No additional bands appeared, nor did any of the initially observed bands disappear in the PL spectra of the exposed NWs, or the referent NWs, after S(T)EM. No obvious trend in variation of PL intensities with respect to the different S(T)EM illumination conditions (acceleration voltage or electron dose) can be observed. The PL intensities after TEM are generally

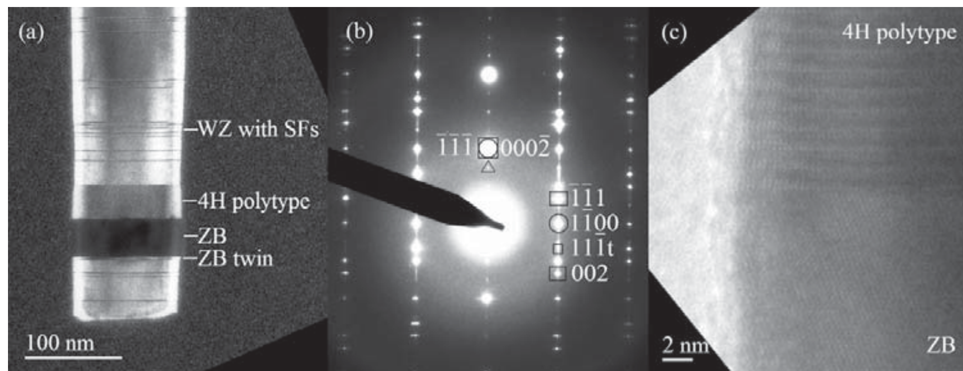

Figure 3. Detailed TEM of the GaAsSb insert area of the NW shown in figure 1: (a) DF TEM and (b) SAED pattern of the insert area where WZ, ZB and 4H polytype reflections are marked by circles, rectangles and a triangle, respectively. The notation 't' refers to the ZB twin section. (c) HREM of the interface between the ZB GaAsSb insert and the 4H GaAs region.

weaker than in the initial PL spectra for the referent NWs. This reduction in PL intensities differs for the different bands within the spectra. For some referent NWs, the intensities of some bands are essentially the same after S(T)EM and after TEM (e.g. band A in figure 2(b)).

3.3. Detailed TEM characterization

TEM characterization revealed the crystal structure and the presence of the lattice defects, such as stacking faults (SFs) in the GaAs WZ segments, in all the 32 NWs. As an example, detailed TEM characterization of the GaAsSb insert area of the candidate NW used in figure 1 is shown in figure 3. With the DF TEM image (figure 3(a)) and SAED pattern (figure 3(b)) of the insert area, and HREM of the upper insert interface (figure 3(c)), it was proven that the NW contains a ZB GaAsSb insert (40 nm long). Between the bottom part of the WZ GaAs core and the ZB GaAsSb insert, there is a 3 nm long ZB section, twinned with respect to the insert. Adjacent to the upper insert interface, there is a 4H polytype section (35 nm long) before the WZ GaAs core continues. The DF image (figure 3(a)) shows that there is a density of less than ten SFs per 100 nm in the WZ GaAs core, for about 200 nm above the 4H polytype section. For the next 400 nm up, the SF density is higher (10–15 SFs per 100 nm, including several unit cell long ZB segments), followed by an SF-free WZ region and thereafter a low density of SFs in the upper half of the NW (not shown).

In most cases, direct transitions between the WZ GaAs core and ZB GaAsSb insert were observed among the NWs studied here. Crystal-phase variation, including twinning and/or 4H polytype section (one such combination is depicted in figure 3(a)), in the GaAsSb insert area is less common for this batch. The SF density and distribution along the whole length varied in all studied NWs. Most of the NWs with a ZB GaAsSb insert had some SFs in the WZ GaAs core below and/or above the insert. The SF density in the upper halves was low (less than ten SF per 100 nm) for most of the NWs.

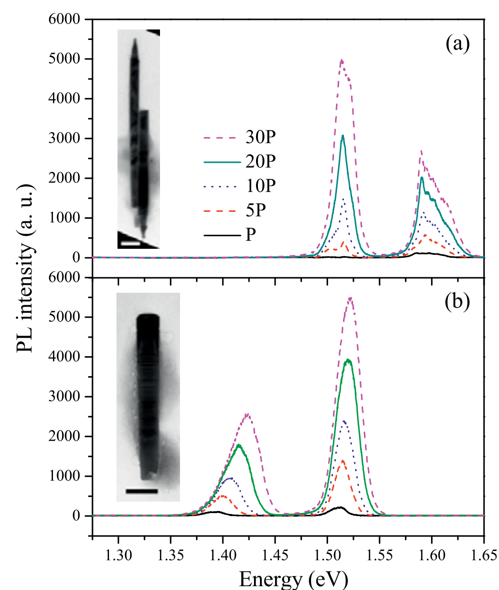

Figure 4. Low temperature (10 K), power dependent PL spectra ($P = 0.5$ W cm^{-2}) of (a) a candidate NW (from specimen CS2) which is a cluster of two NWs and the corresponding BF TEM image in the inset, (b) a candidate NW (from specimen CS1) which is a piece of a NW that fractured above and below the GaAsSb insert region and the corresponding BF TEM image in the inset. The scale bar in each inset is 200 nm.

3.4. Other examples of NWs studied by μ-PL and TEM

The two examples of candidate NWs given in figure 4 highlight that both random sampling of NWs and their individual structural characteristics are reflected in the variations of the measured optical properties. NWs fracture randomly at different positions along their length during sonication. Furthermore, NWs can cluster together and align along the

growth axis in the drying step of specimen preparation. The PL response of a cluster of two NWs and their BF TEM image (inset) are shown in figure 4(a). TEM revealed that the left NW (95 nm in diameter, pointing up) had a ZB GaAsSb insert and that fracture of the NW occurred within the insert. Above the ZB GaAsSb insert, the NW is SF-free for more than 0.8 μm. The right NW (105 nm in diameter, pointing down) is only an upper WZ part of a NW broken above the GaAsSb insert, starting with three SFs within the first 30 nm at the bottom and continuing with SF-free WZ for about 0.5 μm. The SFs are mostly concentrated and unevenly distributed (on average less than ten SFs per 100 nm) in the upper halves of these two NWs. The peaks in the 1.275–1.45 eV region are extremely weak compared to the B and C bands of the same NW (figure 4(a)) and the corresponding band A (figure 2(a)) of the candidate NW depicted in figure 1. Several distinct peaks are observable within bands B and C in figure 4(a) at low excitation powers and broadening of both bands can be observed as the excitation power increases.

The second example (figure 4(b)) is a piece of a NW, 132 nm in diameter, that fractured 0.25 μm below and 0.77 μm above the GaAsSb insert, hence the upper part with the gold particle is missing. Similarly to the candidate NW depicted in figures 1 and 3, this NW contained a ZB GaAsSb insert (40 nm long) followed by a 5 nm long ZB twin segment, and subsequently a 4H polytype section (37 nm long), as proven by HREM and SAED (not shown). However, the NW depicted in figure 4(b) has a higher SF density (about twenty SFs per 100 nm, including several unit cell long ZB segments) in the WZ sections all the way below and for 0.57 μm above the insert (followed by 0.2 μm of SF-free WZ section ending with four SFs near the upper free surface). In the corresponding PL spectra, the PL peaks of bands A and B are blue-shifted by about 35 meV (from 1.388 eV) and 11 meV (from 1.510 eV), respectively, as the excitation power increases from 0.5 to 15 W cm^{-2}. No distinct peaks are present within bands A and B for this NW at excitation powers higher than 0.5 W cm^{-2}. Compared to the A and B bands, an extremely weak C band is observed only at power densities above 3 W cm^{-2}.

4. Discussion

We first discuss the experimental challenges that we overcame in the course of developing an efficient correlated PL–TEM strategy. Subsequently, we discuss whether and how the electron beams used in this procedure might affect the PL response of NWs. Finally, we correlate the optical properties with the structural characteristics of the here presented NWs.

4.1. Technical aspects

From a practical point of view, proper handling of the fragile silicon/silicon nitride TEM grid is crucial throughout the total procedure. The holder construction as used here allows safer transfer of a TEM grid between different experimental setups. Selecting candidate NWs in all nine windows increases the success rate for a correlated PL–TEM study. The electron transparent support, 50 nm thick amorphous silicon nitride, withstood multiple cooling–heating cycles and the applied laser powers in the μ-PL. The repeatedly good μ-PL response obtained in this study indicates that the heat conduction of the specimen mounted in the holder is sufficient. Thus, there seems to be no reason to coat the specimen with a heat conducting film as done by Bao *et al* [8]. However, in that particular study the power density at the sample was much higher (up to 8000 W cm^{-2}) than in our experiments (below 100 W cm^{-2}). Recently, Heiss *et al* [14] demonstrated that conventional C-foil TEM grids can be used in a scanning confocal μ-PL with a liquid-helium bath cryostat, for a correlated PL–TEM study. The probe spot size used by Heiss *et al* [14] was much smaller (0.8 μm) than in the μ-PL setup (5 μm) used in the present study. However, a 0.8 μm probe still excites relatively large sections of a NW. CL-like resolution and diffusion studies are not possible by either of the two PL–TEM approaches.

In the present study, the silicon nitride support film and Si frame did not affect the PL spectra in the applied photon energy range and the PL response from the NWs was similar to our observations for NWs deposited on a Si substrate [20, 23]. As figure 3 demonstrates, the 50 nm thick silicon nitride support film still allows structural characterization by imaging and electron diffraction techniques. Thicker support films would be more stable in handling, but the TEM techniques would be affected, especially low voltage STEM (1–30 kV), DF TEM and HREM studies. For a 100 nm silicon nitride support film we expect that BF TEM and SAED would still give useful information about the NW crystal phases. The here developed correlated PL–TEM strategy should equally well be applicable to other semiconducting NWs or nanostructures. However, for a complete correlated PL–TEM study of Si and N containing semiconductors including compositional analysis by TEM, alternative frame and support film might be required. As the silicon nitride films are flat and rigid, other characterization tools, like scanning probe techniques, could be incorporated into this routine.

The obtained PL–TEM results demonstrate that there are three major challenges in sampling representative single NWs. First, random NWs break off at random positions along their length during sonication, as figures 1 and 4 demonstrate. In the case of homogeneous NWs (i.e. without significant variation of crystal phases and defect density, for example) or NWs without an intended axial insert, random sampling and breaking would not significantly affect the measured optical properties. Here however, due to the differences between individual NWs and the presence of an axial insert a substantial number of NWs was studied to obtain meaningful correlated data. A possible way to control the sampling of axially heterostructured NWs better is by scraping NWs from the growth substrate and, after dispersion on a TEM grid, cutting the NWs into desired segments by focused ion beam (FIB). However, it should be investigated whether the electrons (see below) and the Ga ions used in the FIB process alter the PL response.

A second challenge is the dispersion of the NWs onto the TEM grid. The dispersion preparation method is quick and can give a large number of candidate NWs for a correlated PL–TEM study. The dispersion solution, contamination concentration, droplet size, evaporation conditions and surface

conditions of the NWs and support film greatly affect the success rate of achieving single NWs on the support film. Thus, for the three specimens studied here, the success rates of achieving single NWs on the support film differed. In addition, objects other than NWs can be transferred onto a grid unintentionally (see figure 1(a)). Hydrocarbons or carbonous contaminants originating from the dispersion solvent, for example the stain around the candidate NW in figure 1, can affect the electron microscopy. Such contaminations can be removed by plasma cleaning before the μ-PL and electron microscopy studies. However, PL–plasma cleaning–PL(TEM) series should be performed to determine the effects of plasma cleaning on the PL response of the NWs. On the other hand, the larger clusters of misaligned NWs and debris from the substrate (also from the bottom side) are beneficial for orientating on the specimen and tracing candidate NWs in a systematic approach in the different experimental setups.

The third major challenge is the optical selection of candidate NWs, as clusters of several parallel or nearly parallel NWs can be easily misinterpreted as a single NW. As TEM revealed, single NWs were dispersed throughout the specimen C1, whereas none of the considered candidate NWs was single. This indicates that the probability of selecting a thin single core-only NW (50–70 nm in diameter) by optical imaging is rather low due to the limited spatial resolution. For the specimens CS1 and CS2, containing core–shell NWs ($>$100 nm in diameter and length of μm order), the initial selection provided more single NWs than in the specimen C1, mainly due to their larger diameter and also due to the better quality of the dispersion.

4.2. The influence of S(T)EM and TEM on PL

In order to overcome the technical challenges, an easily-accessible imaging technique, such as S(T)EM, with sufficient spatial resolution is necessary prior to a correlated PL–TEM study. Therefore, low/medium energy (5–30 kV) S(T)EM was conducted on specimen CS2 in order to investigate whether and how the electrons affect the optical properties. The PL spectra for each NW from the three PL sessions were compared with each other as well as for exposed and referent NWs. When comparing the PL spectra of all 18 candidate NWs exposed to the electron beam in S(T)EM, the observed differences in PL spectra before and after S(T)EM could not be associated with different accelerating voltages or doses for the exposed candidate NWs. In addition, the PL spectra of the referent NWs of specimen CS2 have similar, in some cases significant (see band C in figure 2(b)), variations in the PL intensities. Therefore, PL intensity redistribution (between the present PL bands) of the exposed NWs is not likely to be associated with any kind of structural damage induced by 5–30 kV S(T)EM. These differences in the PL spectra, for both exposed and referent NWs, could be caused by external conditions such as beam alignment and laser power, positioning of the laser spot, orientation of the laser polarization with respect to a candidate NW and small variations of temperature (from 10 to 15 K) between the three μ-PL experiments. PL emission from the unexposed referent NWs is still significantly strong, despite the handling, several heating cycles or the vacuum in the μ-PL stage and in the electron microscopes. We therefore conclude that 5–30 kV S(T)EM is not inducing any observable changes to the optical properties and hence can be used as a selection tool for single NWs. Based on the observations, we see no restriction in using 5–30 kV electron beam lithography for contacting single NWs or integrating NWs into devices. Note that these observations are valid for NW heterostructures based on GaAs, AlGaAs and GaAsSb.

As the here presented observations indicate, S(T)EM imaging at all applied acceleration voltages can reveal whether a candidate NW is indeed single or a cluster of two or more NWs. By using S(T)EM, one can preselect a NW based on the required morphology or diameter and cleanliness. For example, short thin NWs, observable in BF STEM (figure 1(b)), can be missed by secondary electron imaging. Moreover, 30 kV BF STEM revealed the position of the GaAsSb insert in the referent NW depicted in the inset of figure 2(b). At the GaAsSb insert, marked by the black arrow, the diameter of the referent NW is slightly increased compared to the GaAs core below and above the insert. The referent NW is anti-tapering further in the upper part, similar to the candidate NW from the same specimen depicted in figure 1(c). Alternatively, the diffraction contrast in BF STEM could identify the position of a ZB GaAsSb insert within a WZ GaAs core, twins within an insert and SFs within the WZ segments for a particular orientation of the NW with respect to the electron beam. Therefore, BF STEM at 20–30 kV would be the preferred imaging technique prior to a correlated PL–(S)TEM study.

For all the studied NWs from the three specimens and all crystals phases present in the NWs, it is clear that the high energy electrons in the TEM gravely affected the PL spectra. There was no apparent change of the NWs' crystal structure, appearance or morphology during TEM exposure that would indicate the detrimental effects on optical properties introduced by the high energy electrons. This coincides with previous studies of heterostructured GaAs-based NWs [6, 21, 22].

Among the known lattice defects that can be induced in n- and p-type bulk GaAs by electron irradiation are vacancies and interstitials (e.g. Frenkel defects) in the As sublattice [19]. Complex defects can be formed by electron irradiation (0.1–1 MeV) at 300 K when As interstitials migrate away from As vacancies until they are captured by impurities like C on Ga sites [19]. In the case of the heterostructure GaAs-based NWs here studied, we expect that Frenkel and complex defects are created by similar means during room temperature 200 kV TEM experiments. Frenkel defects are undetectable by the basic TEM techniques used here. On the other hand, luminescence of similar NWs was reported up to 80 kV in a CL study at 20–140 K [24]. Thus, a critical electron acceleration voltage is expected between 80 and 200 kV, above which the optical properties of WZ GaAs/AlGaAs NWs are degraded due to the formation of Frenkel defects.

4.3. PL and crystal structure

In this section we focus on the direct correlation between the PL and TEM data obtained in this work. We discuss each

observed PL emission band (A, B, C) separately by comparing the differences in PL spectra and structure for each presented NW.

4.3.1. Origin of band A. We relate the lowest energy PL band (A) with the presence of an intact ZB GaAsSb insert [6, 20, 23]. Only the ZB GaAsSb insert can give emission in band A (1.30–1.45 eV), and we have never observed PL in this region from similar NWs without the ZB GaAsSb insert. The NWs in figures 1 and 4(b) both contain an intact ZB GaAsSb insert and exhibit a band A, starting at 1.364 eV and 1.388 eV, respectively, for low excitation powers. As opposed to this, the left NW in the inset of figure 4(a) was broken within the insert and therefore non-radiative recombinations at the free surface of the insert would be expected to be dominant in this part of the NW and quench any luminescence. The right NW in the inset of figure 4(a) fractured above its insert, hence the remainder cannot contribute to any GaAsSb related luminescence at all. This absence or damage of the GaAsSb insert is reflected in the PL spectra of figure 4(a) by the extremely weak emission within the A range compared to the B and C bands. We notice that the GaAsSb related band position varies in this dataset and in comparison to previous studies [6, 20, 23] due to variations of the Sb composition between the inserts. Therefore, high spatial resolution composition analysis and high angle annular DF STEM (100–300 kV) should be incorporated into the strategy when more accurate correlation of the optical properties and the composition is needed.

The two single NWs in figures 1, 2(a), 3 and 4(b) provide general insight into how the present structural defects affect the GaAsSb insert PL emission. For these two NWs, we observe SFs in the WZ GaAs core, the ZB GaAs twin below or above the ZB GaAsSb insert and a 4H GaAs polytype section above the insert (adjacent to either the insert or the twin). This is similar to what has been observed previously in core WZ GaAs NWs with ZB GaAsSb inserts [6]. For the ZB GaAsSb insert preceded by the ZB GaAs twin and followed by the 4H GaAs polytype (figure 3), several higher energy peaks within band A (figure 2(a)) appear as the excitation power increases. Such behaviour is characteristic for band-filling effects at a type I band alignment, which is expected of a ZB GaAsSb insert in a WZ GaAs core, both adequately defect-free [20]. Note that a ZB twin below and 4H polytype above the insert appear to have no influence on the GaAsSb related band. Another NW (not shown) in the data set, with 4H polytype section directly above the insert, supports this claim.

In contrast, if the ZB GaAsSb insert is followed by a ZB GaAs twin (and 4H polytype section), a blue-shift (35 meV, when the power density is increased by 0.5 to 15 W cm^{-2}) of band A occurs with higher excitation power, and no distinct higher energy peak appears, see figure 4(b). Such a blue-shift could occur if the band alignment between the ZB GaAsSb insert and the subsequent ZB GaAs twin was of type II. In our previous uncorrelated study [20], a similar blue-shift of a 1.27 eV peak was observed for core–shell NWs, and for the NWs from that batch a ZB GaAs twin following the ZB GaAsSb insert was a common feature. However, to get a more precise indication of which type of recombination occurs in the region of the ZB GaAsSb insert, time-resolved μ-PL is required [23].

4.3.2. Origin of band B. The energy of band B corresponds to the GaAs core [7, 20]. When the WZ GaAs core is dominated by SFs (figure 4(b)), band B shows blue-shift with increasing excitation power. When regions of varying SF density are present in the WZ GaAs core (the NW in figures 1 and 3), the corresponding band B contains a couple of distinct peaks (1.507–1.515 eV). The presence of SFs in the WZ GaAs core in these three NWs (figures 1 and 3, the right NW in figures 4(a), (b)) might obscure the observation of the GaAs WZ free exciton.

PL peaks within 1.43–1.51 eV were previously reported for ZB/WZ GaAs NWs [14, 25] and correlated with a mixture of twinned ZB and WZ sections. Heiss *et al* [14] related the PL emission at 1.515 eV to WZ GaAs. In the present case, there are no secluded ZB GaAs segments (longer than several ZB unit cells) nor twinned ZB GaAs sections within the WZ GaAs core in any of the presented NWs. For this reason the peak at $\sim$1.515 eV cannot be associated with ZB GaAs free exciton for the NWs presented here. Therefore, the peak within 1.515 ± 0.005 eV, as observed for a large number of NWs in this data set, has to be associated with the WZ GaAs core with a random density of SFs.

4.3.3. Origin of band C. Band C is AlGaAs related luminescence [21]. For the core–shell NW batch used here, an axially grown WZ AlGaAs segment above the WZ GaAs core, formed during shell growth, is expected [21]. All the NWs examined here which contained the tip with gold particles (figures 1, 4(a)) should contain this axial AlGaAs segment. Based on the growth specifics, we estimate that the GaAs core above the GaAsSb insert is about 0.7 μm long on average. The length above the GaAsSb insert, 1.87 μm for the NW in figure 1(c) and 1.84 μm for the left NW in figure 4(a), exceeds the estimated length of the GaAs core above the insert and suggests the existence of the AlGaAs segment. The remaining segment of 0.77 μm above the GaAsSb insert in the NW depicted in figure 4(b) indicates that the NW contains only a small portion (maximum 0.1 μm long) of the AlGaAs segment, which can be correlated to the absence of the C band at low excitation powers (below 3 W cm^{-2}). Judging from the length (1.4 μm) and absence of the GaAsSb insert, the right NW in figure 4(a) should consist of a GaAs/AlGaAs core–shell and axial AlGaAs segment and thus contribute to both the B and C bands (together with the left NW). Based on all these considerations, we conclude that the PL emission in band C originates from the WZ AlGaAs segment axially grown above the GaAs/AlGaAs core–shell. The AlGaAs shell itself does not contribute to band C.

The repeatedly observed weak intensity (both before and after STEM) of the AlGaAs band compared to the ZB GaAsSb and WZ GaAs bands in figure 2(a) can be associated with the low SF density in the upper half of the NW (figure 1(c)), although the exact position where the WZ GaAs core ends and the axial WZ AlGaAs starts cannot be deduced from basic

TEM images taken here [11]. A low SF density in the upper half of a NW allows transport [16, 17] of carriers from the axial WZ AlGaAs segment all the way to the WZ GaAs core and thus reduces the number of carriers recombining in the AlGaAs. For the two NWs in figure 4(a), despite the low SF density in the upper parts, the AlGaAs emission is repeatedly strong (comparable to the GaAs emission) indicating that the carriers radiatively recombine mostly in the axial AlGaAs segments and GaAs cores.

5. Conclusion

In this work, a correlated PL–TEM strategy is developed in order to efficiently analyse a significant number of single heterostructured GaAs-based NWs and directly correlate their optical and structural properties. As the selection of representative single NWs turned out to be a challenge for optical microscopy, the effects of 5–30 kV S(T)EM on the optical properties were investigated. The PL spectra before and after S(T)EM (5–30 kV) show that the electrons used for S(T)EM imaging do not alter the optical properties. Therefore, the selection of single clean NWs by low voltage S(T)EM can be applied before μ-PL. This would allow more systematic PL–TEM studies by selecting NWs with a specific morphology. In contrast, the high energy electrons in TEM (200 kV) create lattice defects in the NWs, which cause non-radiative recombinations. Hence, TEM should be performed as the last step in a correlated PL–TEM routine. The strategy proposed here can be applied to other nanostructured semiconductor materials and other characterization tools can be incorporated.

Using the correlated PL–TEM data, the optical and structural properties of WZ GaAs/AlGaAs core–shell NWs with axial ZB GaAsSb inserts were directly connected. Depending on which fragment of a NW is sampled, the PL spectra have one, two or three bands related to ZB GaAsSb, GaAs and WZ AlGaAs. The ZB GaAsSb inserts exhibit type I or II PL emission depending on the surrounding crystal phases. The GaAs band, centred at $\sim$1.515 eV, originates from recombinations between SFs and the surrounding WZ phase (type II band alignment). The AlGaAs band in the 1.60–1.65 eV range originates from the axially grown AlGaAs segment and not from the AlGaAs radial shell.

Acknowledgments

This work was supported by the ‘RENERGI’ program (Grant No. 190871) of the Research Council of Norway. We acknowledge the work carried out by Thang Ba Hoang on the initial PL–TEM trial. We thank Lyubomir Ahtapodov for helpful discussions.

References

[1] Yang P, Yan R and Fardy M 2010 *Nano Lett.* **10** 1529

[2] Stelzner T, Pietsch M, Andrä G, Falk F, Ose E and Christiansen S 2008 *Nanotechnology* **19** 295203

[3] Garnett E and Yang P 2010 *Nano Lett.* **10** 1082

[4] Johnson J C, Choi H-J, Knutsen K P, Schaller R D, Yang P and Saykally R J 2002 *Nat. Mater.* **1** 106

[5] Hua B, Motohisa J, Kobayashi Y, Hara S and Fukui T 2009 *Nano Lett.* **9** 112

[6] Dheeraj D L, Patriarche G, Zhou H, Hoang T B, Moses A F, Grønsberg S, van Helvoort A T J, Fimland B-O and Weman H 2008 *Nano Lett.* **8** 4459

[7] Hoang T B, Moses A F, Zhou H L, Dheeraj D L, Fimland B O and Weman H 2009 *Appl. Phys. Lett.* **94** 133105

[8] Bao J, Bell D C, Capasso F, Wagner J B, Mårtensson T, Trägårdh J and Samuelson L 2008 *Nano Lett.* **8** 836

[9] Akopian N, Patriarche G, Liu L, Harmand J C and Zwiller V 2010 *Nano Lett.* **10** 1198

[10] Heiß M, Gustafsson A, Conesa-Boj S, Peiró F, Morante J R, Abstreiter G, Arbiol J, Samuelson L and Fontcuberta i Morral A 2009 *Nanotechnology* **20** 075603

[11] van Helvoort A T J, Dheeraj D L, Zhou H, Grønsberg S, Patriarche G, Fimland B O and Weman H 2010 *J. Phys.: Conf. Ser.* **241** 012084

[12] Caroff P, Dick K A, Johansson J, Messing M E, Deppert K and Samuelson L 2008 *Nat. Nanotechnol.* **4** 50

[13] Zwiller V *et al* 2008 *C. R. Phys.* **9** 804

[14] Heiss M *et al* 2011 *Phys. Rev.* B **83** 045303

[15] Borys N J, Walter M J, Huang J, Talapin D V and Lupton J M 2010 *Science* **330** 1371

[16] Gustafsson A, Bolinsson J, Sköld N and Samuelson L 2010 *Appl. Phys. Lett.* **97** 072114

[17] Bolinsson J, Mergenthaler K, Samuelson L and Gustafsson A 2011 *J. Cryst. Growth* **315** 138

[18] Zagonel L F *et al* 2011 *Nano Lett.* **11** 568

[19] Pons D and Bourgoin J C 1985 *J. Phys. C: Solid State Phys.* **18** 3839

[20] Moses A F, Hoang T B, Dheeraj D L, Zhou H L, van Helvoort A T J, Fimland B O and Weman H 2009 *IOP Conf. Ser.: Mater. Sci. Eng.* **6** 012001

[21] Zhou H L, Hoang T B, Dheeraj D L, van Helvoort A T J, Liu L, Harmand J C, Fimland B O and Weman H 2009 *Nanotechnology* **20** 415701

[22] Dheeraj D L, Patriarche G, Largeau L, Zhou H L, van Helvoort A T J, Glas F, Harmand J C, Fimland B O and Weman H 2008 *Nanotechnology* **19** 275605

[23] Ba Hoang T, Moses A F, Ahtapodov L, Zhou H, Dheeraj D L, van Helvoort A T J, Fimland B-O and Weman H 2010 *Nano Lett.* **10** 2927

[24] Ishikawa K, Yamamoto N, Tateno K and Watanabe Y 2008 *Japan. J. Appl. Phys.* **47** 6596

[25] Spirkoska D *et al* 2009 *Phys. Rev.* B **80** 245325

Chapter 7

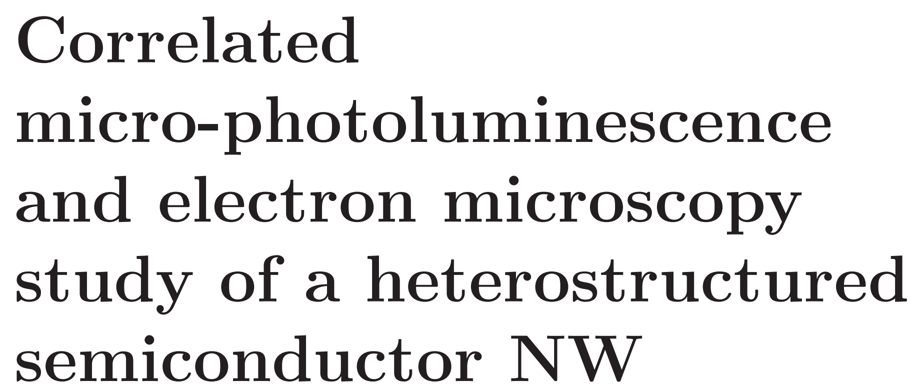

Correlated micro-photoluminescence and electron microscopy study of a heterostructured semiconductor NW

Journal of Physics: Conference Series **326** (2011) 012043

Correlated micro-photoluminescence and electron microscopy study of a heterostructured semiconductor nanowire

J Todorovic[1], A F Moses[2], D L Dheeraj[2], P Olk[2], B O Fimland[2], H Weman[2] and A T J van Helvoort[1]

[1] Department of Physics, [2]Department of Electronics and Telecommunications, Norwegian University of Science and Technology, NO-7491 Trondheim, Norway

a.helvoort@ntnu.no

Abstract. Correlation between the optical and the structural properties of an individual heterostructured nanowire (NW) is crucial for optimising the NW synthesis and device design. In this work, low temperature (10 K) micro-photoluminescence (μ-PL), low and high voltage scanning transmission electron microscopy and conventional transmission electron microscopy are applied to the same individual NWs. The studied NWs, grown by Au-assisted molecular beam epitaxy, have a wurtzite GaAs core with a zincblende GaAsSb axial insert, enclosed with an AlGaAs radial shell and a GaAs capping layer. By subsequent analysis of one and the same NW by μ-PL and several electron microscopy techniques in different microscopes, we can relate the spectral features of a single NW to the structural features, such as different crystal phases, lattice defects and composition.

1. Introduction

III-V semiconductor nanowires (NWs) are attractive for a broad range of applications as for example solar cells, lasers, single photon sources and sensors. The electro-optical properties of III-V NWs are directly related to the crystal phase (zincblende (ZB) or wurtzite (WZ)), lattice defects and the composition. In practice, NWs from the same batch can differ for example by dimensions or defect configuration. Therefore structural and electro-optical properties of the same NW have to be investigated. Direct correlation between the optical properties and the structural characteristics of an individual NW is crucial for understanding band alignments and quantum confinement effects as well as for optimizing the NW synthesis and device design for future applications. Transmission electron microscopy (TEM) based techniques are commonly used to fully characterize structural elements of NWs. However, conventional TEM specimens are not well suited for micro-photoluminescence (μ-PL) studies. So far, only a few correlated PL-TEM studies of the same NW have been reported [1,2].

In this work, low temperature (~10 K) μ-PL, scanning (transmission) electron microscopy (S(T)EM) at 30 kV and 200 kV and conventional transmission electron microscopy (TEM) at 200 kV are applied on the same WZ GaAs/AlGaAs core-shell NWs with ZB GaAsSb core inserts. Due to the complexity of this particular heterostructure, a range of different electron microscopy techniques were required to understand which structural features actually affected the optical properties. By detailed correlated study of one NW, particular structural characteristics are directly connected with the observed PL features.

2. Experimental details

The NWs were grown by Au-assisted molecular beam epitaxy [3,4]. The heterostructure consists of WZ GaAs core with ZB GaAsSb axial insert, AlGaAs radial shell, and GaAs cap. In addition, an axial WZ AlGaAs segment forms on top of the WZ GaAs core during AlGaAs radial shell growth [4]. NWs were ultrasonically dispersed in isopropanol and drops of the solution were transferred onto a Si TEM grid with a 50 nm thick amorphous silicon nitride support film (ThinWindows Inc.). For safe handling and good heat conduction in the μ-PL experiments, the TEM grid was sealed between two Mo washers with central holes of 2 mm [5].

μ-PL was performed in a Janis ST-500 cryostat at ~ 10 K, using continuous laser excitation at the wavelength of 532 nm. The power density at the specimen was varied from 1 W/cm^2 to about 50 W/cm^2. The detection system included a Horiba Jobin Yvon iHR500 spectrometer with a 300 grooves/mm grating and an Andor Newton^{EM} Si electron multiplying charge-coupled device (EMCCD). The spectral resolution of the system is about 200 μeV.

Structural characterization was performed on a Hitachi S-5500 S(T)EM (30kV, cold field emission gun) for low magnification bright field (BF) STEM and on a Philips CM30 TEM (200 kV, LaB_6) for BF TEM, dark field (DF) TEM, and selected area electron diffraction (SAED). A JEOL 2010F TEM/STEM (200 kV, Schottky field emission gun) was used for lattice imaging (HREM) and high angle annular DF (HAADF) STEM (probe size approx. 0.5 nm, 49-120 mrad collection angle range).

3. Results and discussion

A NW, containing all structural elements of the studied heterostructure after breaking off from the substrate, was selected from the PL-TEM dataset of about 30 NWs for a more detailed TEM and STEM characterization. Figure 1 shows that the PL spectra of the NW contain three bands, designated as A (1.35-1.45 eV), B (1.50-1.55 eV) and C (1.58-1.65 eV), which are characteristic for this NW heterostructure. The BF STEM (30 kV) image in the inset of figure 1 presents an overview of the NW divided into regions I (containing ZB GaAsSb insert surrounded by the WZ GaAs core and the AlGaAs shell, full line box), CS (WZ GaAs/AlGaAs core-shell, dashed line box) and AS (WZ AlGaAs axial segment, dotted line box) which are the origins of the characteristic PL emissions A, B and C respectively [2,4,5]. Low voltage STEM provides quick insight into morphology and size of the NW and can be performed before μ-PL as well [5].

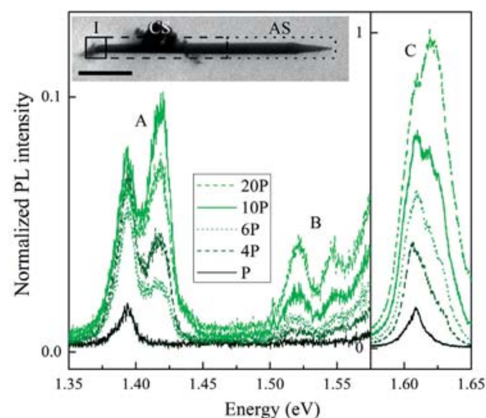

Figure 1. Low temperature (10 K), power dependent PL spectra (P = 2.55 W/cm^2) of a NW together with 30 kV BF STEM image (inset). For this NW heterostructure, A, B and C designate the three characteristic PL bands which originate respectively from the regions I, CS and AS of the NW (inset). The PL spectra were taken before the electron microscopy studies. The scale bar in the inset is 500 nm. Note that the NW is anti-tapering towards the tip.

The ground state of GaAsSb related PL emission (band A) is observed at 1.39 eV (figure 1) for this NW. No blue shift of this PL band can be observed with increase of excitation power. Such behavior indicates that both electrons and holes are confined within the GaAsSb insert (i.e. type I band alignment between ZB GaAsSb insert and WZ GaAs core) [6]. At higher excitation powers a PL peak at 1.42 eV appears (figure 1). The origin of this PL transition is not clear at present.

Region I of the NW is shown in detail in figure 2. DF TEM (figure 2(a)) visualizes the different crystal phases present with the highest contrast: the ZB insert (dark) in the WZ NW (bright) with some stacking faults (SFs). The NW has a diameter of 76 nm in region I, just above the fracture, and a 38 nm long ZB GaAsSb insert. There are two adjacent SFs in the WZ GaAs core starting at about 21 nm above the insert (figure 2(a,b)). The crystal phases were confirmed by SAED (not shown). Note that the crystal phases and the SFs can be identified by lattice imaging (HREM) on the 50 nm thick SiN support film. Type I behavior of GaAsSb related PL emission (figure 1) indicates that the two SFs (figure 2(a,b)) are far enough away from the insert not to affect carrier recombination within the insert.

Figure 2 shows that the fracture of the NW occurred within ZB and WZ sections in region I, which might have impact on the PL emission from the ZB GaAsSb insert. HAADF STEM was used to visualize the difference between the WZ GaAs core and the WZ AlGaAs shell, or the ZB GaAsSb insert and the ZB AlGaAs shell. The HAADF STEM image in figure 2(d) and area intensity profile in the inset show the core-shell structure of regions I and CS with a core diameter of 27 nm. The shell is about 25 nm thick, whereas the width of the NW at the lower ZB-WZ interface is 49 nm as viewed in a <110> projection. This indicates that the fracture of the ZB section occurred mostly within the ZB AlGaAs shell. Since the insert is mostly intact and almost completely passivated by ZB AlGaAs shell and WZ GaAs core, the GaAsSb related PL emission (band A in figure 1) remains observable.

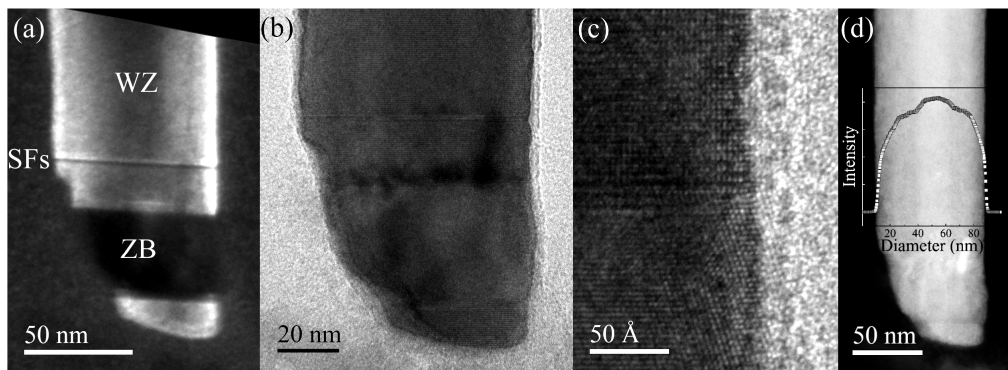

Figure 2. Detailed TEM characterization of the region I: (a) DF TEM image on a <110> zone. (b) HREM image. (c) HREM image of the upper ZB-WZ interface. (d) HAADF STEM image few degrees off a <110> zone with 100 nm area intensity profile (inset). Diameter of the core is 27 nm.

The upper part of the NW (regions CS and AS) is shown in figure 3. HAADF STEM shows where the transition between the core-shell structure and the axial WZ AlGaAs segment occurs (figure 3(a)). The WZ GaAs/AlGaAs core-shell segment above the two SFs in region I (figure 2(a,b,d)) is SF free for about 0.7 μm, which is the estimated core length above the insert based on the growth parameters [3]. The WZ region with high SF density (about 0.3 μm long) follows as observed in HAADF STEM and BF TEM (figure 3(a,b)). The gradual transition from WZ GaAs/AlGaAs core-shell to axial WZ AlGaAs segment starts in this region. In the axial AlGaAs segment, the SF density is reduced (figure 3(a,c)) compared to the core-shell transition region. The area intensity profiles (figure 3(d)) of the HAADF STEM image (figure 3(a)) show the core-shell structure in area 1 and the axial AlGaAs segment (no core-shell structure) in area 2. The anti-tapering shape of the NW (inset of figure 1) explains the higher intensity of the axial AlGaAs area profile (profile 2, figure 3(d)).

In the PL spectra (figure 1), band B (GaAs related PL emission) is broad and weak compared to bands A and C. The B-band is related to a mixture of various type II recombinations due to the SFs in the WZ GaAs core [5]. The peak at 1.55 eV that appears at higher excitation powers is not completely understood at present.

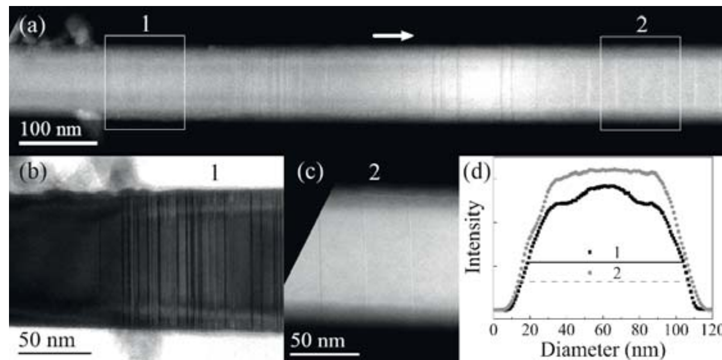

Figure 3. (a) DF STEM image few degrees off zone with two 100 nm long areas selected. The arrow shows the growth direction of the NW. (b) BF TEM image on a <110> zone including area 1. (c) DF STEM image of area 2. (d) Area intensity profiles of areas 1 and 2 in DF STEM image in (a).

The AlGaAs related PL emission is coming from the axial AlGaAs segment and not from radial AlGaAs shell [4,5]. The significant volume of the axial AlGaAs segment (40 % of the total NW length of 2.2 μm), the presence of SFs in the axial AlGaAs and the high SF density in the WZ GaAs/AlGaAs core-shell transition region can partly account for the strong AlGaAs PL emission compared to GaAsSb and GaAs PL emissions since SFs act as carrier traps. SFs here seem to prevent carrier diffusion from their origin, within the axial AlGaAs segment, through the WZ GaAs core towards the ZB GaAsSb insert.

4. Conclusions

One single NW has been studied by μ-PL and in three different electron microscopes to directly correlate the structural features to the optical properties. ZB GaAsSb related PL emission exhibits type I band alignment when the SFs in surrounding WZ GaAs core are far away (about 21 nm) from the ZB GaAsSb insert. By combining HREM and HAADF STEM, it was determined that the fracture within the ZB phase occurred mainly within the AlGaAs shell. Such fracture still allows PL emission from the ZB GaAsSb insert. The GaAs related PL emission, at about 1.52 eV, originates from type II recombination between SFs and the WZ GaAs core with varying distribution of SFs in the region of transition from core-shell to axial AlGaAs segment. The AlGaAs related PL emission originates from the WZ AlGaAs axial segment and is most prominent in the PL spectra of this NW due to the presence and distribution of SFs in the axial segment and in the transition region from core-shell to the axial segment.

Acknowledgment
This work was supported by “RENERGI” program (Grant No. 190871) of the Research Council of Norway.

References
[1] Bao J, Bell D C, Capasso F, Wagner J B, Mårtensson T, Trägårdh J and Samuelson L 2008 *Nano Letters* **8** 836
[2] Heiss M et al. 2011 *Phys. Rev. B* **83** 045303
[3] Dheeraj D L et al. 2008 *Nano Letters* **8** 4459
[4] Zhou H L et al. 2009 *Nanotechnology* **20** 415701
[5] Todorovic J, Moses A F, Karlberg T, Olk P, Dheeraj D L, Fimland B O, Weman H and van Helvoort A T J 2011 *Nanotechnology* **22** 325707
[6] Hoang T B, Moses A F, Ahtapodov L, Zhou H, Dheeraj D L, van Helvoort A T J, Fimland B O and Weman H 2010 *Nano Letters* **10** 2927

Chapter 8

A Story Told by a Single Nanowire: Optical Properties of WZ GaAs

Accepted in Nano Letters

cxs00 | ACSJCA | JCA10.0.1465/W Unicode | research.3f (R3.4.i1:3887 | 2.0 alpha 39) 2012/09/13 09:54:00 | PROD-JCA1 | rq_791126 | 11/07/2012 09:05:14 | 6

NANO LETTERS

Letter

pubs.acs.org/NanoLett

A Story Told by a Single Nanowire: Optical Properties of Wurtzite GaAs

Lyubomir Ahtapodov,[†] Jelena Todorovic,[‡] Phillip Olk,[†] Terje Mjåland,[†] Patrick Slåttnes,[†] Dasa L. Dheeraj,[†] Antonius T. J. van Helvoort,[‡] Bjørn-Ove Fimland,[†] and Helge Weman*,[†]

[†]Department of Electronics and Telecommunications and [‡]Department of Physics, Norwegian University of Science and Technology, NO-7491 Trondheim, Norway

Supporting Information

ABSTRACT: The optical properties of the wurtzite (WZ) GaAs crystal phase found in nanowires (NWs) are a highly controversial topic. Here, we study high-quality pure WZ GaAs/AlGaAs core–shell NWs grown by Au-assisted molecular beam epitaxy (MBE) with microphotoluminescence spectroscopy (μ-PL) and (scanning) transmission electron microscopy on the very same single wire. We determine the room temperature (294 K) WZ GaAs bandgap to be 1.444 eV, which is ~20 meV larger than in zinc blende (ZB) GaAs, and show that the free exciton emission at 15 K is at 1.516 eV. On the basis of time- and temperature-resolved μ-PL results, we propose a Γ_8 conduction band symmetry in WZ GaAs. We suggest a method for quantifying the optical quality of NWs, taking into consideration the difference between the room and low temperature integrated PL intensity, and demonstrate that Au-assisted GaAs/AlGaAs core–shell NWs can have high PL brightness up to room temperature.

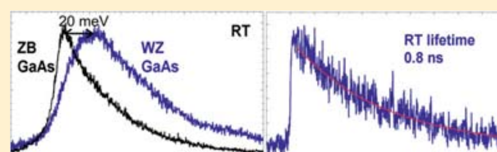

KEYWORDS: *Nanowire, wurtzite, optical properties, GaAs, photoluminescence, PL-TEM*

Semiconductor nanowires (NWs) are expected to provide a platform for future nanotechnology applications. Many prototype devices in electronics and optoelectronics such as NW transistors,[1] lasers,[2] light-emitting diodes,[3] and photovoltaics[4] have already been demonstrated, and many more are no doubt waiting in store. However, while much of the ongoing research is aimed at exploring the vast possibilities of novel device design that semiconductor NWs offer, some of their fundamental optical and electronic properties are still elusive. Especially controversial are the optical and electronic properties of the hexagonal wurtzite (WZ) GaAs crystal phase which is often observed in NWs and never in the bulk.

Current discussions on the topic have two main issues. The first one deals with the bandgap width, the free exciton binding energy, and the conduction band symmetry of WZ GaAs. Theoretical works predict a change of the low temperature GaAs bandgap from the conventional cubic zinc blende (ZB) to the WZ phase in opposite directions, suggesting values of 1.553 eV[5] and 1.504 eV[6] versus the well-known 1.519 eV in bulk ZB GaAs.[7] Reported experimental results for WZ GaAs point at higher,[8,9] lower,[10,11] and approximately the same value as in ZB.[12,13] There is a further uncertainty as to whether the conduction band in WZ GaAs is of Γ_8 symmetry, as proposed by De and Pryor,[6] or of Γ_7 symmetry, as claimed by Ketterer et al.[13] Knowledge of the conduction band symmetry is critical for gaining a better understanding of important properties of WZ GaAs such as the electron effective mass, the free exciton binding energy, and recombination lifetimes.

The second issue is related to the optical quality of Au-assisted NWs grown via the vapor–liquid–solid (VLS) technique and their suitability for device applications. Breuer et al.[12] suggest that Au incorporation in the NWs takes place during Au-assisted MBE growth, leading to extremely short recombination lifetimes at room temperature and greatly suppressed radiative quantum efficiency as compared to self-catalyzed MBE grown GaAs NWs. Since it is well established that Au-assisted MBE growth using the VLS mechanism often yields NWs of large crystal phase diversity,[14,15] it is important to study high-quality pure WZ GaAs NWs in this context and develop a method for benchmarking their overall optical quality. The latter is expected to have large implications on the performance of NW-based optoelectronic devices.

In this Letter, measurements were done on carefully selected GaAs/AlGaAs/GaAs core–shell–cap NWs and comprised correlated microphotoluminescence spectroscopy (μ-PL) and (scanning) transmission electron microscopy ((S)TEM) on the same single NW. In the first stage of the experiment, NWs were drop-cast on a 50 nm thick SiN TEM support, and single wires were identified with low-voltage (30 kV) STEM[16] prior to optical characterization. Then, polarization-resolved μ-PL was performed at several temperatures, from low (15 K) to room temperature (RT, 294 K), in order to assess the crystalline purity of the WZ phase in the NWs and to select NWs of interest. The selection criteria will be described in the following. The NWs of choice were studied further with time- and temperature-resolved μ-PL, again in the range from 15 K to RT.

Received: July 12, 2012
Revised: October 22, 2012

 © XXXX American Chemical Society dx.doi.org/10.1021/nl3025714 | *Nano Lett.* XXXX, XXX, XXX–XXX

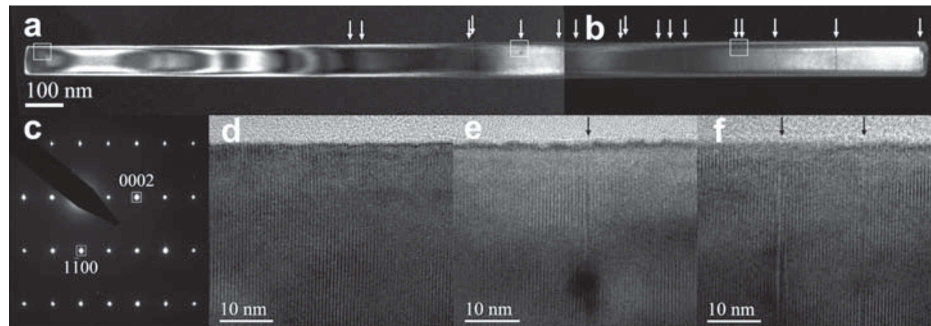

Figure 1. Dark-field (DF) TEM images of the whole WZ GaAs/AlGaAs core−shell NW: (a) from the (0002) reflection, showing the lower part of the NW, and (b) from the (−2200) reflection, showing the upper part or the NW. (c) Selected area electron diffraction pattern taken from the lower part of the NW. (d−f) Examples of high-resolution TEM images from the areas marked with white squares in (a) and (b), from left to right, respectively. Arrows mark the selected stacking faults.

The third and final stage of the experiment was extensive structural characterization of the chosen NWs with TEM. All results reported in this work refer to one particular NW representative of high-quality, nearly defect-free Au-assisted VLS growth. All in all six such NWs with a pure WZ crystal phase were found which amounts to roughly 10% of all studied NWs.

The NW presented in this Letter consists of a pure WZ GaAs crystal phase with a total of 17 stacking faults (SF) and no ZB segments along its entire length of 2.4 μm, as verified with TEM (Figure 1). Notably, all SFs are well separated from each other, the smallest spacing between two SFs being 8 nm. A low temperature (15 K) μ-PL spectrum of the selected WZ GaAs NW is presented in Figure 2a. The emission peak at 1.516 eV is in agreement with other observations in similar NWs,[11,13] and the full width at half-maximum (fwhm) line width of 6 meV is among the narrowest reported in a single WZ GaAs NW so far. The linear polarization properties of this peak are displayed in Figure 2b. The PL is polarized perpendicularly to the NW axis, at 92 ± 5°, as determined from a least-squares fit to the data (see captions in Figure 2b for a description), which is in accordance with optical selection rules and earlier observations in WZ GaAs NWs.[11,13,17] The degree of linear polarization of the PL peak is, however, also influenced by another effect in addition to optical selection rules, namely the linear polarization due to the dielectric contrast between the high-refractive index NW and the surroundings (vacuum).[18] The dielectric contrast effect implies that optical transitions that are unpolarized according to the selection rules (like e.g. the ZB GaAs bandgap emission/absorption) are eventually polarized parallel to the NW axis and acts as to depolarize the WZ GaAs emission peak[17] that is polarized perpendicular to the NW axis according to the selection rules. Hence, the WZ GaAs emission will not be as strongly polarized as ZB GaAs, and the degree of polarization will change from NW to NW depending on the wire diameter. For the particular NW presented in this work the degree of linear polarization is −71%.

More important than this linear polarization degree is, however, the fact that the emission from the NW comprises only a single, narrow PL peak without any significant spectral features of different emission energy or polarization direction or degree, regardless of excitation power. In particular, the contribution of the SFs to the PL spectra could not be conclusively recognized based on the obtained data. In fact, a

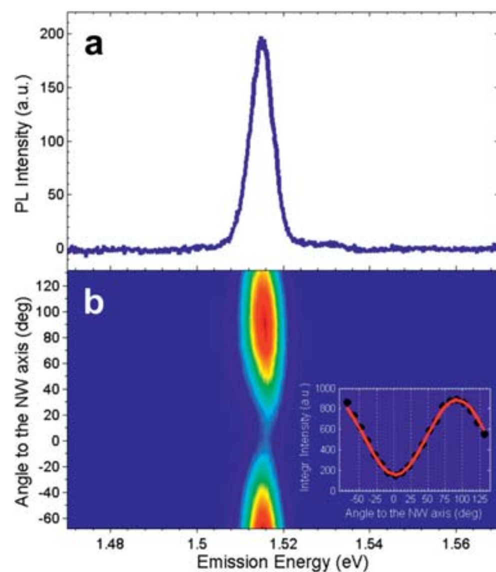

Figure 2. (a) Low temperature (15 K) PL spectrum of the WZ GaAs/AlGaAs core−shell NW grown by Au-assisted MBE presented in this Letter. (b) False-color plot of the linearly polarized PL as a function of the angle to the NW axis. Inset shows a fit to the integrated PL intensity as a function of the angle to the NW axis obtained with the Jones matrix formalism. The PL polarization direction is determined from this fit to be at 92.4° to the NW axis.

WZ GaAs SF, interpreted as a GaAs ZB electron quantum well or dot with WZ GaAs NW barriers[17,19] (depending on the NW core diameter; here it is ~40 nm which favors its interpretation as a quantum well), can provide only one spin-degenerate shallow bound state for electrons. The main reason for this is the short width of a single SF in WZ GaAs: 0.98, 1.31, or 1.63 nm determined by whether it is 1, 4/3, or 5/3 ZB GaAs unit layers thick, respectively. An estimate of the emission energy difference between SF-mediated optical transitions and the free exciton emission was carried out using conduction band offsets between WZ and ZB GaAs as calculated in ref 6 and considering a range of values for the electron effective mass

133 in WZ GaAs between the ZB value[7] and the theoretical WZ value from ref 6. The SF was modeled as a rectangular potential well. The results reveal that both emission lines should lie within ~10 meV where the upper limit corresponds to electron effective mass of $1.025m_0$ (m_0 is the free electron rest mass) in the WZ GaAs crystal phase. The value of $1.025m_0$ was arrived at by De and Pryor assuming that the ZB and WZ GaAs lattice constants are identical;[6] if the actual electron effective mass in WZ GaAs is in fact lower, SF-mediated recombination may turn out to be energetically unfavorable compared to the WZ GaAs free exciton emission. Considering the fact that spectral features neither of different emission energy nor of different polarization direction or degree were observed close to the main PL peak, we conclude that in the present case the contribution of isolated SFs to the PL spectrum of a WZ GaAs NW is negligible.

This will not be the case for regions of high density of SFs where electronic coupling between SFs can lead to the formation of minibands and alter the emission energy while promoting more available states for electrons, as has been demonstrated for rotationally twinned InP NWs.[20] Spectra consisting of several differently polarized contributions to the PL signal were indeed observed for other NWs from the same growth batch that did contain ZB segments and WZ segments with a high density of SFs. Consequently, in order to gain access to the fundamental optical properties of WZ GaAs, such NWs were disregarded in the NW selection process, and only ones showing a single PL peak polarized perpendicularly to the NW axis were chosen for further studies. Moreover, several important conclusions follow from the arguments presented so far. First, considering the fact that TEM characterization has been proven to deteriorate the optical properties of NWs,[16] polarization-resolved μ-PL presents a straightforward, non-destructive alternative for evaluating the crystal phase purity of single NWs. Second, NW sampling and/or growth optimization as means of avoiding the presence of multiple SFs and other defects are crucial when using NWs in order to observe and exploit the WZ GaAs properties. Finally and perhaps most importantly, since the bandgap emission in pure semiconductor materials at low temperatures (15 K) is due to free exciton recombination, the free exciton emission in WZ GaAs (see Figure 2) was determined to be 1.516 eV, only 1 meV larger than its ZB counterpart.[7]

At RT, the WZ GaAs PL emission peaks at 1.444 eV, as shown in Figure 3. To compare this value to ZB, the spectrum of a ZB GaAs epilayer grown by MBE is plotted in Figure 3 as well. Since all excitonic effects are thermalized at RT, as indicated by the asymmetric PL line shape, the emission peak corresponds to band-to-band transitions. Excitation levels were kept as low as possible so that band-filling effects are not expected. The WZ GaAs bandgap at RT (294 K) is hence determined to be 1.444 eV ± 1 meV, where the error margin stems from inaccuracies in the PL peak position determination. The bandgap at room temperature is thus 20 meV larger in WZ GaAs compared to ZB GaAs.

For a closer inspection of the bandgap difference between WZ and ZB GaAs, the PL emission energy of the WZ GaAs NW is plotted as a function of temperature in Figure 4, along with reference data for bulk ZB GaAs,[21] and the ZB GaAs epilayer presented in Figure 3. Data sets for both GaAs phases are least-squares fitted with a modified version of the Varshni equation.[22] Clearly, the Varshni curves diverge as temperature is increased, requiring different parameters for WZ and ZB GaAs in the modified Varshni equation. This is unlike previous observations of the WZ and ZB phases of InP in NWs,[23] where the lowest conduction band in the WZ phase is expected to have Γ_7 symmetry. Indeed, the Γ_7 conduction band symmetry corresponds to wave function symmetry very similar to the Γ_6 symmetry of the ZB conduction band. At the same time, the Γ_8 symmetry predicted theoretically for the WZ GaAs conduction band[6] implies different electron effective mass and electron−phonon interaction and is hence a prerequisite for a different temperature dependence of the bandgap. As a matter of fact, divergences of the Varshni curves corresponding to the split-off gaps in WZ and ZB GaAs[10] and between various higher-lying conduction bands in ZB GaAs[21] have already been reported. This reasoning is further corroborated by the low temperature (50 K) time-resolved μ-PL data shown in Figure 5a. The time decay of the PL signal is fitted with a double-exponential model, taking into account the shorter-lived electron−hole plasma emission in the initial stages of the carrier relaxation after excitation with a high energy laser pulse (pulse peak power ~2 MW/cm^2), and the slower free exciton or band-to-band recombination at later stages.[24] According to theoretical results for the WZ GaAs band structure,[6] free excitons should still provide the dominant part of the recombination at 50 K. The free exciton PL lifetime is hence determined to be 3.3 ns, which exceeds reported corresponding values for ZB GaAs NWs (~1 ns[24,25]). The PL lifetime is likely the result of a competition between free exciton radiative recombination and nonradiative 222

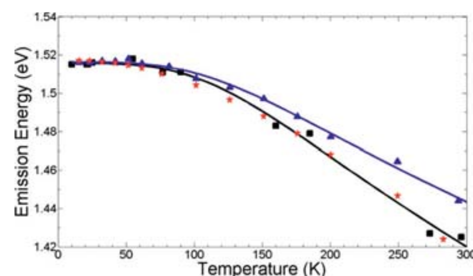

Figure 4. Comparison of the temperature dependence of the WZ (blue triangles) and the ZB GaAs PL emission energy (red stars correspond to the ZB GaAs epilayer from Figure 3 and black squares correspond to bulk ZB GaAs data from ref 21). Solid lines represent fits with the modified Varshni equation[22] to the WZ (blue) and the ZB (black) GaAs data (NW).

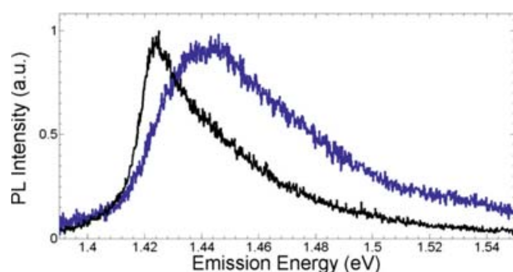

Figure 3. Room temperature PL spectra for the WZ GaAs/AlGaAs core−shell NW grown by Au-assisted MBE (blue) and a reference ZB GaAs epilayer grown in the same MBE machine (black).

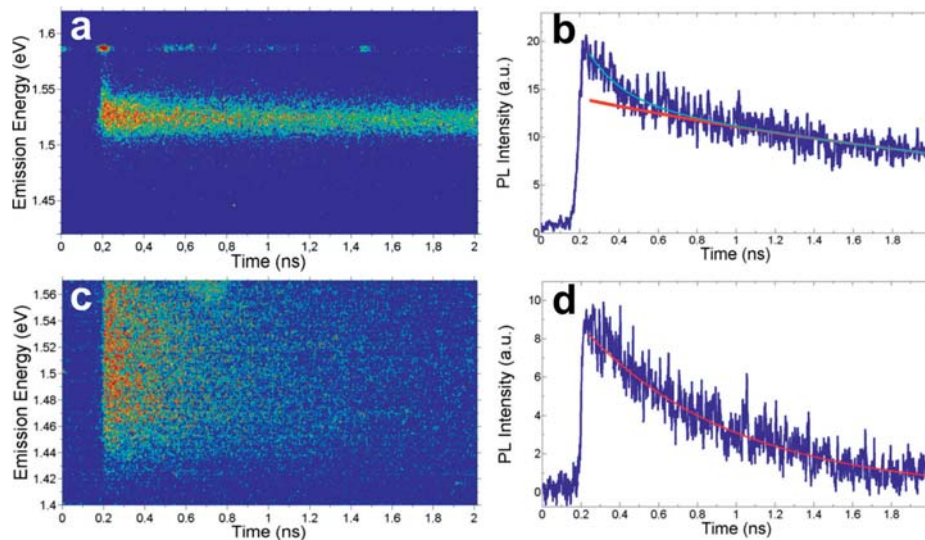

Figure 5. (a) Time-resolved streak image of the WZ GaAs/AlGaAs core−shell NW at 50 K. (b) Time decay of the main PL peak from (a). The spectrum is fitted with two exponentials corresponding to the high peak-power effects in the initial stages of the decay (not shown) and the free exciton emission at later instants (red line). Cyan line represents the sum of the two exponentials. The energy range considered is ∼20 meV wide, centered on the main PL peak, and the free exciton recombination lifetime is 3.3 ns. (c) Time-resolved streak image of the WZ GaAs/AlGaAs core−shell NW at RT. Because of the low sensitivity of the streak camera below 1.5 eV, the GaAs PL peak is not fully resolved. Consequently, for the time-decay profile in (d), integration was done on the high-energy flank of the PL peak. An energy window of ∼40 meV centered at 1.45 eV was used. The room temperature PL recombination lifetime is 0.8 ns.

recombination at the GaAs/AlGaAs core−shell interface,[25] but even so, the observed WZ GaAs PL lifetime is longer than the volume lifetime for state of the art ZB GaAs NWs determined in that reference. Assuming that there is no fundamental difference between the quality of the WZ and ZB GaAs/AlGaAs interfaces, we hence conclude that the longer free exciton recombination lifetimes are an inherent property of the WZ GaAs crystal phase and reflect the reduced oscillator strength of the Γ_8–Γ_9 optical transition. A WZ GaAs conduction band minimum with Γ_8 symmetry was also favored by Peng et al. in their discussion on resonant Raman spectroscopy of single WZ GaAs NWs.[26]

The results for the WZ GaAs free exciton emission energy and the conduction band symmetry presented in this Letter are in contradiction with some of the published work on the subject. Jahn et al.[9] presented μ-PL and cathodoluminescence (CL) data from predominantly WZ GaAs NWs with (μ-PL and CL) and without (only μ-PL) AlGaAs shell. By examining the spatially resolved CL spectra, these authors determined the low temperature WZ GaAs bandgap to be at least 55 meV larger than its ZB counterpart. However, there are two phenomena that should be kept in mind which could explain the discrepancy with our results. First, high excitation intensities typically used in CL can cause band-filling effects in surface-passivated GaAs/AlGaAs core−shell NWs leading to a blue-shift of the CL emission. The effect is similar to what happens in the initial stages of the PL decay after transient excitation with laser pulses of high peak power.[24] Furthermore, the presence of coupled SFs may introduce quantum confinement of holes in WZ GaAs segments between narrowly spaced ZB GaAs segments. This could lead to spatially indirect type II emission at energies larger than the WZ GaAs bandgap. The same argument holds for the work of Hoang et al.[8] where the WZ GaAs free exciton emission was reported to be at 1.544 eV. Additionally, quantum confinement effects may have been present in those NWs in view of their small diameter and the presence of a dead layer at the unpassivated GaAs surface. There are also reports of WZ GaAs bandgap values lower than ZB[10] and a WZ GaAs conduction band minimum of Γ_7 symmetry.[13] In the former case, radial quantum confinement effects were proposed in the WZ GaAs NWs which may in fact have been bulklike. In the latter case, the claim was made based only on indirect evidence from the 2LO phonon intensities in resonant Raman spectra of mixed WZ/ZB phase GaAs NWs. In all of the above work no direct correlation of the PL properties with the structure properties was made, which in the present study was found to be crucial in order to exclude effects due to a nonpure WZ GaAs crystal phase.

Another topic of controversy has of late been the suitability of Au-assisted NWs for optoelectronic applications. In order to evaluate the optical quality of our MBE grown Au-assisted WZ GaAs NWs, we studied the NW presented above with time- and temperature-resolved μ-PL. The streak image obtained at RT (294 K) with 2 ps pulsed excitation (∼5 MW/cm^2 peak power) is presented in Figure 5c. Note that the PL peak at 1.444 eV is not resolved due to the sharp decrease of the streak tube sensitivity below 1.5 eV. Therefore, the high-energy flank of the WZ GaAs peak was used for the analysis of the PL recombination lifetimes. The corresponding time-decay curve, along with a single-exponential fit, is shown in Figure 5d. The PL recombination lifetime at room temperature is 0.8 ns, which, taking into account that the NW core diameter is ∼40 nm, is comparable with state-of-the-art self-catalyzed MBE

grown GaAs NWs reported previously[12] and is far superior to the Au-assisted NWs presented in the same study.

A question that remains to be answered is what physical quantity should be used as an indicator for the optical quality of semiconductor NWs? As pointed out by Breuer et al.,[12] this should ideally be the internal quantum efficiency. It is defined as $\eta_i = \tau/\tau_r$, where τ is the PL recombination lifetime and τ_r is the radiative recombination lifetime.[27] However, the PL recombination lifetime depends strongly on the nonradiative recombination rate. Moreover, the nonradiative and radiative recombination lifetimes have different temperature dependence and are not measured directly. It is thus apparent that neither the PL recombination lifetime nor its temperature dependence provides direct information on the internal quantum efficiency η_i.

Instead, an alternative and more direct method of assessing the optical quality of NWs, based on a comparison between the low temperature and RT PL brightness, is presented below. μ-PL spectra of the WZ GaAs NW taken at 15 K and RT at the same excitation conditions are plotted in Figure 6. The decrease

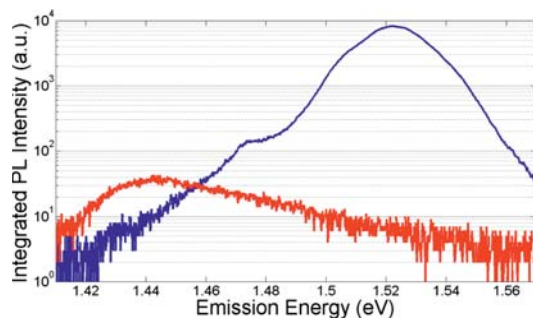

Figure 6. Comparison of the PL spectra of the WZ GaAs/AlGaAs core–shell NW at 15 K (blue curve) and at 294 K (red curve) under similar excitation conditions. The integrated PL intensity at room temperature is less than 2 orders of magnitude lower than at 15 K (precisely, 91 times). The weak shoulder peak in the low temperature PL spectrum is attributed to impurities or native defects in the WZ GaAs NW core.

of the integrated PL intensity from low to room temperature is ~90 times, slightly less than the value reported by Breuer et al.[12] for self-catalyzed ZB GaAs NWs and much lower than the 5 orders of magnitude reported by the same authors for their Au-assisted WZ GaAs NWs. These results were repeated for all other NWs, the brightest of which showed a decrease between 15 K and RT by a mere 21 times (not shown). While the net internal quantum efficiency remains unknown, by virtue of the identical excitation this value corresponds directly to the decrease of the internal quantum efficiency from low to room temperature. We thus propose monitoring of the temperature dependence of the integrated PL intensity as a function of temperature as a reliable and straightforward method for evaluating optical quality in semiconductor NWs. The decrease by 21 times between 15 K and RT is set as a benchmark for state-of-the-art GaAs NWs. We note in passing that the question of Au incorporation in the NW core during Au-assisted VLS growth, as used in the present study, is now rendered of little significance by the bright PL emission and long PL recombination lifetime at RT obtained from the NWs presented in this Letter.

To conclude, we show that the WZ GaAs free exciton emission is at 1.516 eV at low temperature (15 K), almost coinciding with the ZB free exciton emission energy at 1.515 eV. At the same time the RT bandgap of WZ GaAs is 1.444 eV ± 1 meV, which is 20 meV larger than the RT bandgap of ZB GaAs. The divergence of the emission energies of WZ and ZB GaAs as temperature is increased, supported by the unusually long free exciton recombination lifetimes at low temperature, suggest that the conduction band symmetry in WZ GaAs is of Γ_8 symmetry rather than Γ_7. We establish that the decrease of the integrated PL intensity from 15 K to RT is a more reliable means of evaluating the NWs' optical quality than PL lifetimes and set the benchmark of a decrease by around 20 times or less as an indicator of the highest PL brightness achievable with GaAs NWs today. It is thus revealed that Au-assisted GaAs NWs can have a high optical quality and PL brightness comparable to self-catalyzed GaAs NWs.

■ ASSOCIATED CONTENT

Supporting Information

Experimental details for sample growth by MBE, optical characterization by μ-PL spectroscopy, and structural characterization by (S)TEM. This material is available free of charge via the Internet at http://pubs.acs.org.

■ AUTHOR INFORMATION

Corresponding Author

*E-mail: helge.weman@iet.ntnu.no.

Notes

The authors declare no competing financial interest.

■ ACKNOWLEDGMENTS

The authors thank C. Pryor for helpful discussions and T. B. Hoang for critical reading of the manuscript. We are also grateful to J. P. Bergman, P. O. Holtz, and especially to M. Eriksson for their invaluable help during the preliminary lifetime experiments. This work was partly supported by the "NANOMAT" (Grant No. 182091) and "RENERGI" (Grant No. 190871) program of the Research Council of Norway.

■ REFERENCES

(1) Cui, Y.; Duan, X.; Hu, J.; Lieber, C. M. *J. Phys. Chem. B* **2000**, *104* (22), 5213–5216.
(2) Duan, X.; Huang, Y.; Agarwal, R.; Lieber, C. M. *Nature* **2003**, *421* (6920), 241–245.
(3) Huang, Y.; Duan, X.; Lieber, C. M. *Small* **2005**, *1* (1), 142–147.
(4) Garnett, E.; Yang, P. *Nano Lett.* **2010**, *10* (3), 1082–1087.
(5) Murayama, M.; Nakayama, T. *Phys. Rev. B* **1994**, *49* (7), 4710–4724.
(6) De, A.; Pryor, C. E. *Phys. Rev. B* **2010**, *81* (15), 155210.
(7) Gilliland, G. D. *Mater. Sci. Eng., R* **1997**, *18*, 99–399.
(8) Hoang, T. B.; Moses, A. F.; Zhou, H. L.; Dheeraj, D. L.; Fimland, B. O.; Weman, H. *Appl. Phys. Lett.* **2009**, *94* (13), 133105–3.
(9) Jahn, U.; Lähnemann, J.; Pfüller, C.; Brandt, O.; Breuer, S.; Jenichen, B.; Ramsteiner, M.; Geelhaar, L.; Riechert, H. *Phys. Rev. B* **2012**, *85* (4), 045323.
(10) Ketterer, B.; Heiss, M.; Livrozet, M. J.; Rudolph, A.; Reiger, E.; Fontcuberta i Morral, A. *Phys. Rev. B* **2011**, *83* (12), 125307.
(11) Heiss, M.; Conesa-Boj, S.; Ren, J.; Tseng, H.-H.; Gali, A.; Rudolph, A.; Uccelli, E.; Peiro, F.; Morante, J. R.; Schuh, D.; Reiger, E.; Kaxiras, E.; Arbiol, J.; Fontcuberta i Morral, A. *Phys. Rev. B* **2011**, *83* (4), 045303.
(12) Breuer, S.; Pfüller, C.; Flissikowski, T.; Brandt, O.; Grahn, H. T.; Geelhaar, L.; Riechert, H. *Nano Lett.* **2011**, *11* (3), 1276–1279.

387 (13) Ketterer, B.; Heiss, M.; Uccelli, E.; Arbiol, J.; Fontcuberta i
388 Morral, A. *ACS Nano* **2011**, *5* (9), 7585−7592.
389 (14) Johansson, J.; Bolinsson, J.; Ek, M.; Caroff, P.; Dick, K. A. *ACS*
390 *Nano* **2012**, *6*, 6142−6149.
391 (15) Dheeraj, D. L.; Patriarche, G.; Zhou, H.; Hoang, T. B.; Moses,
392 A. F.; Grønsberg, S.; Helvoort, A. T. J. v.; Fimland, B. O.; Weman, H.
393 *Nano Lett.* **2008**, *8* (12), 4459−4463.
394 (16) Todorovic, J.; Moses, A. F.; Karlberg, T.; Olk, P.; Dheeraj, D. L.;
395 Fimland, B. O.; Weman, H.; Helvoort, A. T. J. v. *Nanotechnology* **2011**,
396 *22* (32), 325707.
397 (17) Hoang, T. B.; Moses, A. F.; Ahtapodov, L.; Zhou, H.; Dheeraj,
398 D. L.; Helvoort, A. T. J. v.; Fimland, B. O.; Weman, H. *Nano Lett.*
399 **2010**, *10* (8), 2927−2933.
400 (18) Ruda, H. E.; Shik, A. *Phys. Rev. B* **2005**, *72* (11), 115308.
401 (19) Spirkoska, D.; Efros, A. L.; Lambrecht, W. R. L.;
402 Cheiwchanchamnangij, T.; Morral, A. F. i.; Abstreiter, G. *Phys. Rev.*
403 *B* **2012**, *85* (4), 045309.
404 (20) Bao, J.; Bell, D. C.; Capasso, F.; Wagner, J. B.; Mårtensson, T.;
405 Trägårdh, J.; Samuelson, L. *Nano Lett.* **2008**, *8* (3), 836−841.
406 (21) Lautenschlager, P.; Garriga, M.; Logothetidis, S.; Cardona, M.
407 *Phys. Rev. B* **1987**, *35* (17), 9174−9189.
408 (22) Tran, T. K.; Park, W.; Tong, W.; Kyi, M. M.; Wagner, B. K.;
409 Summers, C. J. *J. Appl. Phys.* **1997**, *81* (6), 2803−2809.
410 (23) Mishra, A.; Titova, L. V.; Hoang, T. B.; Jackson, H. E.; Smith, L.
411 M.; Yarrison-Rice, J. M.; Kim, Y.; Joyce, H. J.; Gao, Q.; Tan, H. H.;
412 Jagadish, C. *Appl. Phys. Lett.* **2007**, *91* (26), 263104−3.
413 (24) Smith, L. M.; Jackson, H. E.; Yarrison-Rice, J. M.; Jagadish, C.
414 *Semicond. Sci. Technol.* **2010**, *25* (2), 024010.
415 (25) Demichel, O.; Heiss, M.; Bleuse, J.; Mariette, H.; Fontcuberta i
416 Morral, A. *Appl. Phys. Lett.* **2010**, *97* (20), 201907−3.
417 (26) Peng, W.; Jabeen, F.; Jusserand, B.; Harmand, J. C.; Bernard, M.
418 *Appl. Phys. Lett.* **2012**, *100* (7), 073102−3.
419 (27) Hwang, C. J. *Phys. Rev. B* **1972**, *6* (4), 1355−1359.

Supporting Information
A Story Told by a Single Nanowire: Optical Properties of Wurtzite GaAs

Lyubomir Ahtapodov[1], Jelena Todorovic[2], Phillip Olk[1], Terje Mjåland[1], Patrick Slåttnes[1], Dasa L. Dheeraj[1], Antonius T. J. van Helvoort[2], Bjørn-Ove Fimland[1] and Helge Weman[1]

[1]Dept. of Electronics and Telecommunications and [2]Dept. of Physics
Norwegian University of Science and Technology, NO-7491 Trondheim, Norway

Experimental Details

1. **Crystal Growth:** The nanowires (NWs) and epilayer studied within this work were grown on GaAs(111)B substrates in a Varian Gen II Modular molecular beam epitaxy (MBE) system. The GaAs/AlGaAs radial heterostructure NWs were grown by Au-assisted vapor-liquid-solid (VLS) technique. The complete growth procedure is described elsewhere[1]. To obtain SF-free WZ GaAs NWs, NWs were grown under high V/III flux ratio at a substrate temperature of 540 °C. For AlGaAs shell growth, the temperature of the Al effusion cell was preset to yield an Al content of ~30%, as calibrated for epitaxial layer on a GaAs(100) substrate. The average diameter of the NW core was defined by the thickness of the deposited Au film, which was set to yield NWs with diameters around 40 nm. In order to achieve efficient passivation of the surface states, the shell was made around 20 nm thick An approximately 5 nm thick radial GaAs shell (cap) was grown on the AlGaAs shell to prevent oxidation. Reference zinc blende (ZB)

GaAs epilayer was grown at a substrate temperature of 610 °C under an As_4 flux of 9×10^{-6} Torr, and the temperature of the Ga effusion cell was preset to yield a nominal planar GaAs growth rate of 0.7 MLs^{-1}.

2. **Micro-Photoluminescence (μ-PL) Spectroscopy -** Measurements were performed in a Janis ST500 continuous flow optical cryostat at sample temperatures ranging from 15 K to 294 K. Excitation was achieved with a Spectra Physics Millennia Nd:YVO laser operating at 532 nm (for the linearly polarized excitation PL measurements) or a Spectra Physics Model 3909S continuous wave (CW) Ti:sapphire laser tuned to 780 nm (the rest of the continuous wave excitation experiments). For time-resolved PL a pulsed Spectra Physics Tsunami Ti:sapphire laser was used to provide ~ 2 ps full-width-at-half-maximum (FWHM) pulses at 780 nm. For all measurements the laser beam was focused to a ~ 1.5 μm diameter spot on STEM-preselected single NWs. PL excitation and detection was done with a 50x, 0.65 numerical aperture (NA), infinity-corrected Mitutoyo microscope lens. PL signal was dispersed with a Horiba Jobin-Yvon single grating spectrometer and detected with an Andor Newton Si charge coupled device (CCD) camera. Time-resolved measurements were carried out with a Princeton Optics Acton SP2500 spectrometer and an Optronis Optoscope SC-10 NIR enhanced streak camera.

3. **(Scanning) transmission electron microscopy ((S)TEM):** A Hitachi S-5500 S(T)EM (30 kV, cold field emission gun) was used for the initial selection of single NWs in bright field (BF) STEM mode at 30 kV. A Philips CM30 TEM (200 kV, LaB_6) was used for BF TEM, dark field (DF) TEM, and selected area electron diffraction (SAED). A JEOL 2010F TEM/STEM (200 kV, Schottky field emission gun) was used for lattice imaging (high resolution electron microscopy).

REFERENCE:

1. Zhou, H. L.; Hoang, T. B.; Dheeraj, D. L.; Helvoort, A. T. J. v.; Liu, L.; Harmand, J. C.; Fimland, B. O.; Weman, H. *Nanotechnology* **2009,** 20, (41), 415701.

Chapter 9

Antimony concentration variation among and within zinc blende GaAsSb inserts in wurtzite GaAs and GaAs/AlGaAs core-shell nanowires

To be submitted

Antimony concentration variation among and within zinc blende GaAsSb inserts in wurtzite GaAs and GaAs/AlGaAs core-shell nanowires

J Todorovic[1], H Kauko[1], L Ahtapodov[2], A F Moses[2], P Olk[2], D L Dheeraj[2], B O Fimland[2], H Weman[2] and A T J van Helvoort[1]*

[1]Department of Physics, Norwegian University of Science and Technology, NO-7491, Trondheim, Norway

[2]Department of Electronics and Telecommunications, Norwegian University of Science and Technology, NO-7491, Trondheim, Norway

*E-mail: a.helvoort@ntnu.no

Abstract. In this work we investigate variation of the Sb concentration among and within zinc blende GaAsSb inserts in bare-core and core-shell wurtzite GaAs nanowires (NWs) grown by Au-assisted molecular beam epitaxy. The NW structure and the Sb concentration are studied by transmission electron microscopy (TEM), energy dispersed X-ray (EDX) spectroscopy and quantitative high angle annular dark field scanning TEM (HAADF STEM) for a large number of NWs. The Sb concentration determined by EDX was systematically lower than as determined by quantitative HAADF STEM. A clear trend relating the Sb concentration with the insert length is observed: the longer the insert the higher the Sb concentration. In addition, there is an Sb concentration gradient both along and across the GaAsSb inserts. Along the insert, the Sb concentration increases gradually from the lower insert interface along the NW axis, reaches a maximum value and decreases towards the upper insert interface. The influence of the Sb concentration gradient on the PL emission from the GaAsSb inserts is investigated with correlated micro-photoluminescence (μ–PL) and TEM-EDX on the same single NWs. Based on the PL results and the observed Sb concentration gradient, we propose a qualitative band diagram for a typical ZB GaAsSb insert in a WZ GaAs NW for the heterostructured NWs studied here. The ground state energy of the GaAsSb insert PL emission was found to decrease with the increasing Sb concentration. Using an existing empirical model, the Sb concentrations were determined from the ground state PL energies. The calculated values were in agreement with quantitative HAADF STEM results, whereas the EDX systematically underestimated the Sb concentration.

PACS: 61.14.-x, 61.72.Nn, 73.40.Kp, 78.55.-m, 78.55.Cr
Keywords: nanowires, heterostructures, GaAs, GaAsSb, zinc blende, wurtzite, (scanning) transmission electron microscopy, composition variation, photoluminescence

1. Introduction

Axial inserts and quantum dots in heterostructured semiconductor nanowires (NWs) have become an attractive topic of research within the last decade and promise a wide range of applications such as transistors[1], solar cells[2] and photodetectors[3]. Growth optimisation of the axial inserts in terms of controlling their size, composition, crystal phase and the structural defects in the surrounding NW core, is of most importance for realizing the application potential of the axially heterostructured NWs.

One of the interesting III-V ternary systems is $GaAs_{1-x}Sb_x$ due to the widely tunable bandgap[4-6]. The composition and the optical properties of strained GaAs/GaAsSb quantum wells[4, 7, 8] and pseudomorphic GaAsSb on GaAs[5, 9], have been a topic of study for some decades. In contrast to these two-dimensional heterostructures, the $GaAs_{1-x}Sb_x$ system in heterostructured semiconductor NWs is a relatively new topic. The growth of zinc blende (ZB) GaAsSb (axial) inserts in wurtzite (WZ) GaAs NWs by Au-assisted molecular beam epitaxy (MBE) was demonstrated in 2008 by Dheeraj et al.[10] Subsequently, there have been a number of reports on ZB GaAsSb inserts in GaAs NWs, focused on the growth optimisation, optical characterization by micro-photoluminescence (PL) and structural characterization by transmission electron microscopy (TEM) of such heterostructured NWs[11-14].

The Sb composition is most commonly studied by energy dispersive X-ray spectroscopy (EDX) in TEM[12, 14], although this technique has a limited detection limit and spatial resolution[15]. One of the few alternative analytical techniques is quantitative high angle annular dark field scanning TEM (HAADF STEM). Recently, quantitative HAADF STEM study of the Sb concentration in ZB GaAsSb inserts in ZB GaAs/ZB GaAsSb/WZ GaAs axially heterostructured NWs grown by Ga-assisted MBE has been reported[16]. In that study, the Sb concentration variations in the ZB GaAsSb inserts were determined for the first time, and a certain concentration gradient both along and across the inserts was observed.

The composition variation within the axial inserts and the interface sharpness can affect the optical properties of these inserts. While the effects of the structural defects on NW optical properties have been reported in a number of studies[17-19], the effect of composition variation within a NW heterostructure on the optical properties has not been studied systematically yet. Furthermore, to achieve precise tailoring of the bandgap, it is crucial to correlate the exact Sb content in the insert with the insert PL emission energy.

In this work, we report on the Sb concentration variation among ZB GaAsSb inserts and within each insert in WZ GaAs bare-core and WZ GaAs/AlGaAs core-shell NWs, and study how this affects the insert optical properties. The Sb concentration and its variation within the inserts were studied with EDX and quantitative HAADF STEM. Using correlated PL-(S)TEM-EDX, the Sb concentration is correlated with the ground state of the ZB GaAsSb PL emission for a large number of bare-core and core-shell NWs. Furthermore, possible effects of the Sb concentration gradient within the insert on the GaAsSb related PL emission, are investigated.

2. Methods

2.1 NW growth

The NWs were grown by Au-assisted MBE on GaAs (111)B substrates. Two different batches were studied in this work: bare-core and core-shell NWs. The difference in the substrate preparation for these two batches is that the bare-core batch had 6 Å thick gold layer, whereas the core-shell batch had 2 Å thick gold. The lower WZ GaAs core was grown for ~ 17 min at a substrate temperature of ~540 ^{o}C under an As_4 flux of $6{\cdot}10^{-6}$ Torr and at a growth rate of ~ 0.7 MLs^{-1} before the insert. The ZB GaAsSb insert was grown for 30 s under an Sb_2 flux of $6{\cdot}10^{-7}$ Torr. For both batches, a growth interruption for one minute with all MBE shutters closed was introduced immediately after the growth of the GaAsSb insert. The growth of the core was continued by opening the Ga shutter 2 s before the As shutter. The upper WZ GaAs core was grown for 17 and 8 min after the insert for bare-core and core-shell NWs respectively. The core-shell NWs had in addition a radial AlGaAs shell around the NW core in order to passivate the GaAs/GaAsSb surface states. The AlGaAs shell, with nominal 30% Al as calibrated for two-dimensional growth on GaAs<100>, was grown for 15 min at ~540 ^{o}C under an As_2 flux of $6{\cdot}10^{-6}$ Torr. An axial AlGaAs segment forms as well during the radial shell growth[20, 21]. Core-shell NWs were capped by a thin GaAs layer (grown for 5 min) to prevent oxidation of the AlGaAs shell. More details on the growth procedures can be found elsewhere[11, 12, 22].

2.2 Specimen preparation and overview

The NWs were scratched off the substrate, dispersed in isopropanol and drop-cast onto TEM grids. In the initial TEM study and compositional studies (EDX, HAADF STEM), 2000 mesh Cu grids with graphene support (Graphene Supermarket Ltd) were used. For the correlated μ–PL and (S)TEM study, 200 μm thick Si TEM grids with nine windows of a 50 nm thick amorphous SiN film (Thinwindows Inc.) were used. NWs from core-shell samples were initially selected by optical microscopy and the single NWs were subsequently identified by low voltage (S)TEM or TEM. In the bare-core samples, single NWs were initially selected by 30 kV STEM (Hitachi S5500). Further details on the PL-TEM method have been reported previously[23].

We studied a substantial number of single NWs from both batches, 14 bare-core and 15 core-shell, by correlated PL-(S)TEM. In addition, we studied more NWs (on Cu/graphene grids) from both batches only by TEM, HAADF STEM and EDX to obtain better statistics and to be able to correlate the Sb concentration to the GaAsSb PL emission energies in the existing PL-TEM data set.

2.3 Micro-PL

The power-dependent μ-PL measurements were carried out using a low vibration optical cryostat (Janis ST-500) with a piezo-driven sample stage. The NWs were excited by a 532 nm laser line at a temperature of ~ 20 K. The power density at the sample was varied from ~30 to ~8500 W/cm^2. The laser was focused (spot size ~ 1.5 μm) onto a single NW using a long working distance microscope

objective lens (50x, NA 0.65, M Plan Apo NIR HR, Mitutoyo). The PL from the NWs was collected by the same lens, dispersed by a spectrograph (Horiba iHR550) and detected by a thermo-electric cooled Andor Newton Si electron multiplying charge-coupled device (EMCCD). The spectral resolution of the system is about 200 μeV.

2.4 TEM and EDX

The structural characterization was performed on a Philips CM30 (LaB_6) TEM and a JEOL 2010F TEM/STEM (Schottky field emission gun, C_s = 1 mm), both operated at 200 kV. The NW crystal phase was analyzed by bright field (BF) and dark field (DF) TEM, selected area electron diffraction (SAED) and high-resolution TEM (HRTEM) lattice imaging. HAADF STEM and EDX analysis (silicon drift detector, INCA software, Oxford Instruments Ltd.) were performed on the JEOL 2010F. EDX analysis was performed in STEM mode (probe size 0.7 or 1 nm, condenser aperture of 50 or 70 μm). To avoid the effects of channelling on the EDX signal[15], the NWs were kept off a major axis, in most cases slightly off the [110] zone axis. The effect of random specimen tilt on the concentration values was estimated by a tilt series to be in the order of a few % Sb. To study the composition variations along a GaAsSb insert, EDX line scans were performed for ~45 min (in total 1-2x10^6 counts) along the inserts starting from and ending in a WZ GaAs region below or above the insert. For quantitative EDX, point scans were performed at several different positions within the inserts for a live time of 200-300 s (counts in the order of ~10^3-5x10^4 per peak). The Ga, As and Sb concentration within the GaAsSb inserts were determined using the INCA software quantification routine with the measured NW thicknesses and the calculated k-factors (in the software). For core-shell NWs, Al in the shell was taken into account as well when calculating the Sb concentration. No reference ZB GaAs regions were available in these NWs to manually determine the k-factors (see reference[16]) for the illumination and detector set-up used here.

2.5 Quantitative HAADF STEM

The Sb concentration was determined more accurately in some representative ZB GaAsSb inserts of bare-core NWs by quantitative HAADF STEM analysis[16], i.e. by performing quantitative comparisons between simulated and experimental HAADF image intensities. Images along the [110] axis for ZB GaAsSb ([11-20] for WZ) were recorded using a probe-forming aperture semi-angle of 8.4 mrad, probe size of approximately 0.2 nm and a dwell time of 38.8 μs. The ADF detector covered an angular range from 29 to 114 mrad.

Simulations for ZB GaAsSb for different Sb concentrations and thicknesses were performed with the STEMsim software[24], based on the frozen-lattice multislice method. Static atomic displacements, caused by Sb being introduced to the GaAs lattice[25], as well as increase in the unit cell size with increasing Sb concentration, were taken into account in the simulations. In order to compare the experimental and simulated intensities, the experimental images were normalized relative to the

incident probe intensity. This was accomplished by performing a detector scan, according to Rosenauer et al[26]. For the GaAsSb inserts, intensity profiles across the NWs as well as profiles taken along the evenly thick central part of the NWs were studied. For more details on the simulations and the quantification approach see Kauko et al[16].

3. Results and Discussion

This section is divided into two parts. In the first part, we present results from the TEM, EDX and quantitative HAADF STEM studies. In the second part, correlated PL-(S)TEM-EDX results are presented.

3.1 Sb concentration variation in the zinc-blende GaAsSb inserts

3.1.1 Structural characterization with basic TEM techniques. The basic structural characterization of NWs from both batches was carried out using BF and DF TEM, SAED and HRTEM. The bare-core NWs had a diameter of ~ 45-80 nm, whereas the diameter of the core-shell NWs was in the range of ~ 70-140 nm. It was confirmed that the GaAs core below and above the GaAsSb insert has predominantly WZ crystal phase with a random density and distribution of SFs for both batches (figure 1). The WZ GaAs core directly below the insert has no other defects than SFs. The GaAsSb inserts have a ZB crystal phase, and for some NWs (~ 25%) the insert consists of two or more twinned segments (see figure 1(a)). In the WZ GaAs core directly above the insert, there is a random distribution of SFs as well, and some NWs (~ 25%) have a 4H polytype segment at the upper insert interface (see figure 1(b)). This is in agreement with the SEM and TEM characterization of similar NWs reported previously[11, 23]. Note that for many NWs there is a SF twinned with respect to the insert at the very interface (lower and/or upper) with the WZ GaAs core (see figure 1(c)). A twinned SF can be single, i.e. a ZB unit layer ABC (0.98 nm), or longer ABCA (1.30 nm) or ABCAB (1.63 nm), where A, B and C represent Ga-As bilayers. To summarize, roughly half of all studied NWs have a twinned insert, a twinned SF at the lower and/or upper insert interface or a 4H polytype segment above the insert, or a combination of these defects. Compared to a previous study[11], the growth interruption introduced after the growth of the insert is found not to prevent the formation of twins within the insert or the 4H polytype at the upper insert interface.

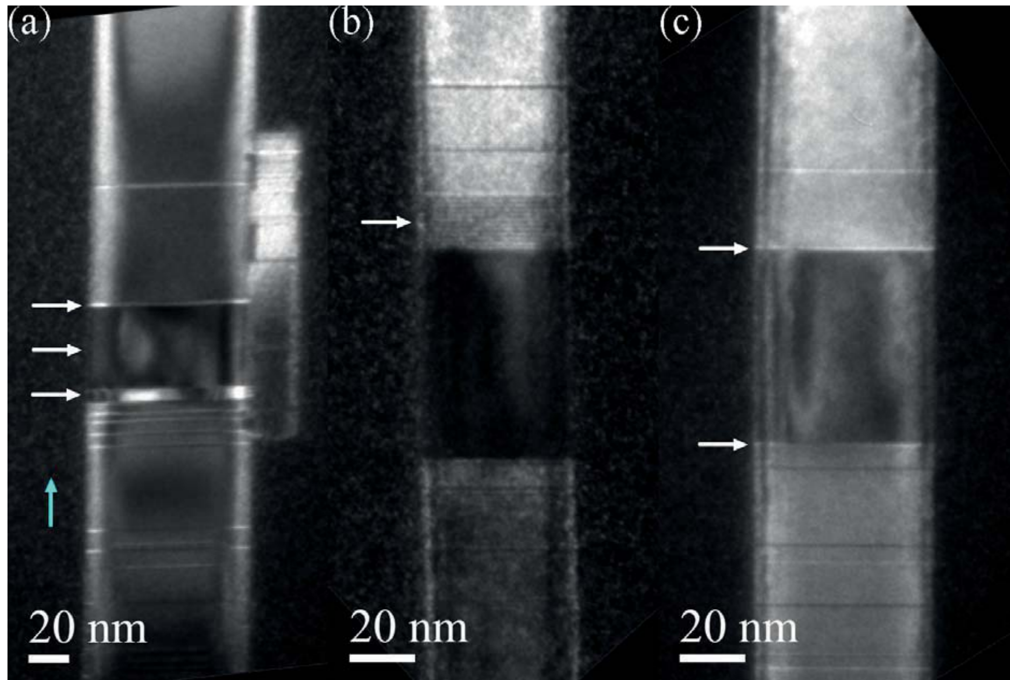

Figure 1. DF TEM images of a bare-core NW with a: (a) 47 nm long twinned ZB GaAsSb insert (twinned segments, 7 nm and 40 nm, are marked by the white arrows), and a 2 nm long twinned SF at the upper interface; (b) 64 nm long ZB GaAsSb insert with a 16 nm long 4H polytype segment at the upper interface (marked by the white arrow) and the closest two SFs 2 nm and 9 nm away from the lower insert interface; (c) 59 nm long ZB GaAsSb insert with twinned SFs at both insert interfaces (marked by the white arrows). All three NWs have SFs both below and above the insert. The blue arrow in (a) indicates $[0001]_{WZ}$ ($[111]_{ZB}$) growth direction for all three NWs.

3.1.2 The dependence of the Sb concentration on the GaAsSb insert length. Figure 2 shows the maximum Sb concentration within the ZB GaAsSb insert as a function of the insert length for 31 NWs from the two batches, out of which 17 NWs were part of the correlated PL-(S)TEM-EDX study. The Sb concentrations presented in the graph were determined by the EDX point analysis. A clear trend can be observed in this plot: the longer the insert the higher the Sb concentration. This trend is evident for the bare-core NWs, whereas for the core-shell NWs, the Sb concentration-insert length distribution is more scattered. This scattered distribution for the core-shell NWs could be due to a lower detection efficiency that would affect the accuracy for low Sb concentrations[15]. In addition, a worse spatial accuracy of the EDX point analysis is present since the probe was spread in the AlGaAs/GaAs shell-cap. Furthermore, the graph shows that the core-shell NWs have in general lower Sb concentrations, shorter inserts (~ 30-55 nm) and a smaller range of insert lengths than the bare-core NWs (~ 20-80 nm).

The GaAsSb insert length was determined from the crystal phase, i.e. as the length of the single or twinned ZB segment between the WZ segments (or between WZ and 4H). The EDX point analysis indicates that there is no Sb in 4H. Twinned SFs, at the lower and/or upper insert interfaces, were not added to the insert length. Larger twinned ZB segments (see figures 1(a) and 3) are included in the insert length since the EDX point analysis indicated the presence of Sb in such segments. However, due to the limited spatial resolution of the EDX point analysis, it might not be possible to prove whether shorter twinned segments and twinned SFs at the insert interfaces contain Sb.

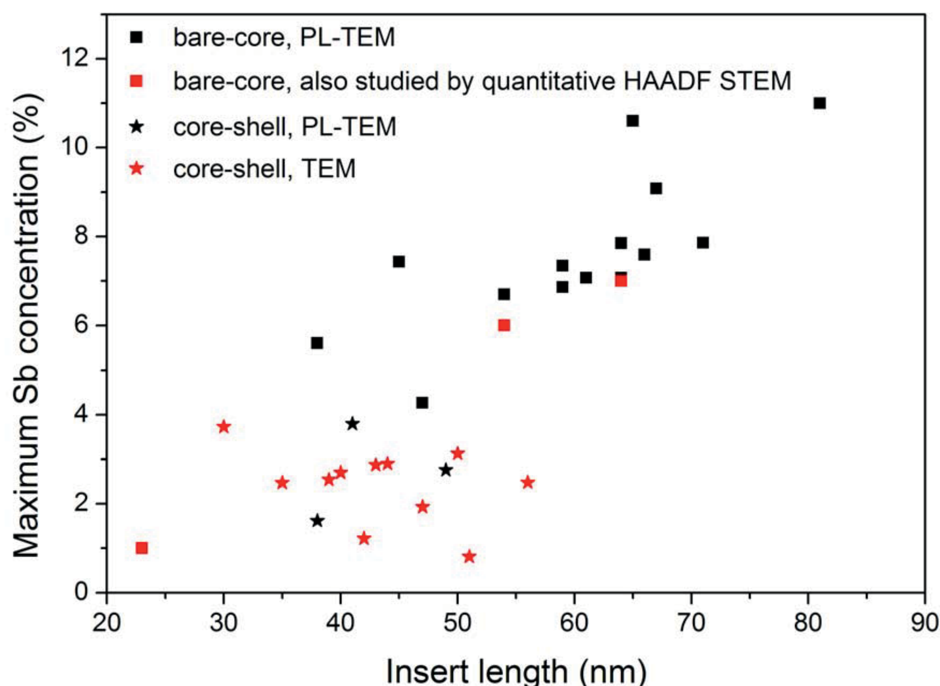

Figure 2. Maximum Sb concentration within the insert, as determined by the EDX point analysis, as a function of ZB GaAsSb insert length for bare-core NWs (squares) and core-shell NWs (stars). The three bare-core NWs marked by red squares were studied by quantitative HAADF STEM as well. The NWs marked by black squares/stars were a part of the correlated PL-(S)TEM study. The rest of the core-shell NWs (red stars) were studied only by TEM and EDX.

Since the GaAsSb inserts were grown for the same time (30 s) for both batches, the large range of insert lengths (altogether ~ 20-80 nm) indicates that the growth rate varied from NW to NW. The NW growth rate for Au-assisted NWs depends on the NW diameter[27, 28] in such a way that the NWs with smaller diameters grow faster than those with larger diameters. The increasing insert length (i.e. increasing growth rate) with decrease of the NW diameter was indeed observed for the bare-core NWs

(not shown). However, no direct connection between the NW core diameter and the growth rate can be drawn for the core-shell NWs, since the core diameter could not be measured directly in this case.

The NW core diameter is determined by the size of the Au-Ga droplet. The diameter distribution and the density of the droplets depend on the thickness of the Au layer and on the processes of heating and dissociation of the Au layer on the substrate before the growth initiation. We assume that the thicker gold layer (6 Å) for the bare-core batch resulted in a larger range of droplet diameters and on average smaller droplets, than for the core-shell batch (2 Å Au layer). This claim is supported by on average longer inserts (i.e. higher growth rates and smaller diameters) for bare-core NWs than for core-shell NWs (see figure 2). The smaller range of insert lengths and shorter inserts for the core-shell NWs, indicate indirectly that this batch has on average larger NW core diameters and more homogeneous growth of the core than in the bare-core batch.

During the GaAsSb growth, there is a competition between Sb and As for incorporation into the Au-Ga droplet[29]. At higher NW growth rates, Sb is incorporated more efficiently than As into the droplet, and thus more Sb is incorporated into the NW. This could explain the Sb concentration-insert length trend in figure 2: NWs with smaller diameters grow faster and hence have longer inserts with more Sb. To summarize, the variation of the insert lengths and the corresponding Sb concentrations is mainly driven by the variation of the NW diameters (i.e. droplet sizes) and subsequently different growth rates.

3.1.3 The Sb concentration variation within an insert analysed by EDX. To determine the maximum Sb concentration for an insert (the values used in figure 2), EDX point analysis was performed at several points along the insert at the evenly thick central part. For all inserts, a clear variation of the Sb concentration values was observed along the insert. The maximum values were found approximately at the insert centre for most of the bare-core NWs, or within the upper half of the insert for a few bare-core NWs. For most of the core-shell NWs, the maximum Sb concentration was found within the upper half of the insert. For both bare-core and core-shell NWs, a much lower Sb concentration was measured in the vicinity (~ 5-10 nm) of the insert interfaces than in the central region of the insert where the Sb concentration reached its maximum.

To study the observed Sb concentration variation within the inserts in more detail, EDX line scans were performed. Comparisons between Sb L_α EDX line scan profiles along the insert for two bare-core NWs with a short and a long insert, and two core-shell NWs with similar insert lengths, are shown in figures 3(a) and (b), respectively. The Sb concentrations indicated in figure 3 are the maximum values as determined by the EDX point analysis. The Sb L_α EDX line profiles confirm that longer inserts have higher Sb concentrations and that the maximum concentration value lies at or above the insert centre. The specific structural characteristics of the NWs shown in figure 3 are described in the following. The bare-core NW with 11% Sb has a 81 nm long defect-free insert and some SFs in the WZ GaAs core below and above the insert. The bare-core NW with 4.3% Sb, which is

presented in figure 1(a), has a twinned insert (two twin planes), where the two, 7 nm and 40 nm long, twinned segments contain Sb, and one 2 nm long twinned SF at the upper GaAsSb/GaAs interface, which may or may not contain Sb. The core-shell NW with 1.6% Sb has a 38 nm long defect-free ZB insert. The core-shell NW with 3.8% Sb also has a twinned insert (one twin plane): 35 nm and 6 nm long segments, where the maximum Sb concentration, as determined by the EDX point analysis, was within the 6 nm twin; followed by a Sb-free 35 nm long 4H polytype GaAs.

These line profiles indicate that the Sb concentration increases gradually from the lower insert interface, reaches a maximum value near the insert centre and decreases with a similar slope as the increase, towards the upper interface. Moreover, the distance over which the Sb concentration increases or decreases varies with the insert length. For shorter inserts this happens over ~ 5-10 nm, whereas for longer inserts (> 60 nm) the Sb concentration gradient spans over ~ 20 nm or more. For some NWs, the Sb L_α EDX line scan profile is fairly symmetric (see NWs with 11% and 3.8% Sb in figure 3), whereas for others, a slightly steeper slope occurs towards the upper insert interface (see NWs with 4.3% and 1.6% Sb in figure 3). For NWs with longer inserts (especially for lengths > 60 nm), the Sb concentration reaches a plateau within, as for the bare-core NW with 11% Sb in figure 3(a). This indicates that the Sb concentration reaches equilibrium and remains approximately the same over the central region of the insert. Indeed, the value of 10-11% was measured with the EDX point analysis at several points near the insert centre for this NW. This was especially observed for long inserts (> 60 nm). For some NWs with shorter inserts, a plateau with an even Sb concentration does not occur (see the bare-core NW with 4.3% Sb in figure 3(a), TEM in figure 1(a)). This is further discussed in the following in terms of the growth kinetics.

The Sb concentration gradient at the beginning of the insert can be explained with increasing Sb content in the Au-Ga droplet with the insert growth time[30]. The higher the growth rate, the longer the insert and the longer the region over which the Sb gradient extends from the lower insert interface (see figure 3(a)). The Sb signal plateau, as in figure 3(a-blue line), indicates that for NWs with long inserts, the equilibrium of Sb concentration in the insert is achieved during the 30 s of insert growth. After the Sb flux is shut off, some Sb remains in the droplet. At this point, the growth interruption is introduced and the NWs stop growing. This suggests that the insert should end with a saturated or high Sb concentration, which is not the case. Therefore, the observed decrease of Sb concentration towards the upper insert interface might be created during the 1 min of the growth interruption due to depletion of Sb from the insert, and diffusion through the droplet into the MBE chamber.

So far, the EDX results were considered as an estimate for a qualitative correlation between the Sb concentration and gradient, with the GaAsSb insert lengths. Despite of the known drawbacks of the EDX point analysis of nano-objects (discussed below)[15], the Sb concentrations still create a clear trend with the insert lengths as seen in figure 2. The accuracy of the EDX analysis largely depends on the number of counts, which is in general low due to the small volumes sampled within a NW. Higher probe currents induce apparent beam damage in the NWs and could not be used to increase the number

of counts. To obtain a high number of counts long scan times are necessary, which means that a certain amount of specimen drift is unavoidable. Due to the drift, there is inaccuracy both in the positions of the point scans and in the spatial range of the line scans, depending on the direction and amount of the drift. In the case of NWs presented in figure 3 for example, the Sb rich area is longer than the actual insert length.

Other sources of errors for the Sb concentrations determined by the point analysis are for example NW tilt[15], beam broadening within the NW and the way the composition is calculated in the INCA software. The calculated k-factors are based on flat geometry, and crystal phase, orientation and morphology are not taken into account in the INCA software. Moreover, the EDX quantification is poor at the detection limit (few atomic percent)[15]. Previous study[16] showed that for Ga-assisted ZB GaAs NWs with similar ZB GaAsSb inserts, manual determination of ZB GaAs k-factor was most reliable for quantification. However, this approach could not be applied here since the GaAs core has WZ phase and no ZB GaAs segments were available in these NWs for reference, as mentioned previously. Therefore, a more accurate quantification method was necessary to determine the Sb concentration and gradient.

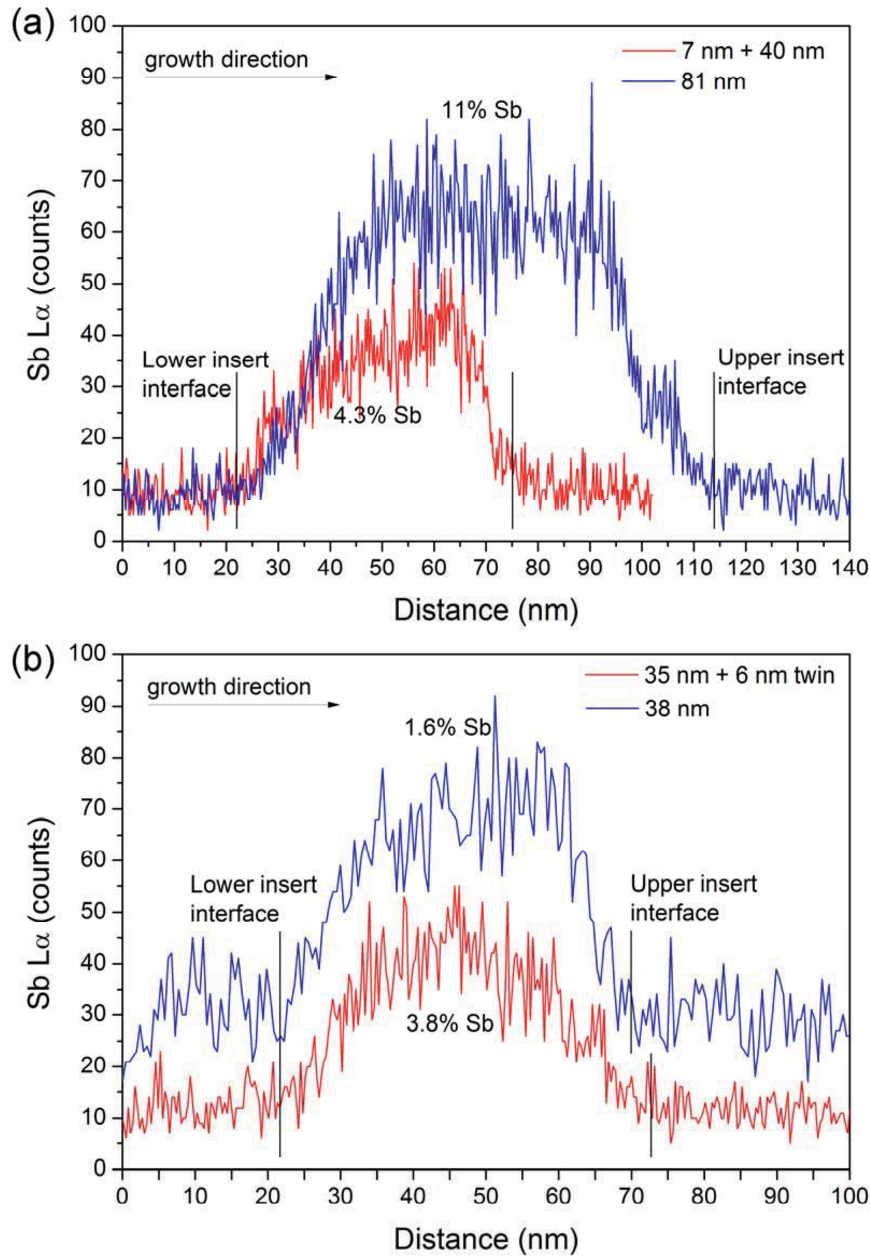

Figure 3. Sb L_α EDX line scan profiles along the ZB GaAsSb inserts for two (a) bare-core and (b) core-shell NWs. Lower and upper insert interfaces are indicated with vertical black lines. The drift along the NW growth axis during the EDX line scan was about 6 nm for the NW with 4.3% Sb and about 10 nm for the other three NWs, which results in Sb-rich region appearing longer than the actual insert length. In addition, there was certain amount of drift across NW for all four NWs. However, the line scans remained within the evenly thick central region.

3.1.4 The Sb concentration and gradient analysis by quantitative HAADF-STEM. To verify the Sb concentration values and qualitative profiles obtained by the EDX analysis, some bare-core NWs (indicated with red squares in figure 2) were additionally analyzed with quantitative HAADF STEM. Results from two bare-core NWs with an extremely short and a long insert are presented in figures 4 and 5, respectively. The figures include HRTEM (a) and HAADF STEM (b) images as well as HAADF STEM intensity profiles across (c) and along (d) the inserts. The experimental HAADF STEM intensity profiles across the insert were taken from a 3 nm wide region near the insert centre, indicated with the red boxes in figures 4(c) and 5(c). The simulated intensity profile across the insert is generated assuming a uniform distribution of Sb and a certain value of the Sb concentration, based on the experimental intensity level at the central part of the cross-sectional profile. The Sb concentration profiles along the inserts, shown in figures 4(d) and 5(d), are obtained by quantifying the HAADF STEM intensities averaged along the evenly thick central part of the NWs, indicated with the ~ 20 nm wide red boxes in figures 4(c) and 5(c).

The NW presented in figure 4 has a 23 nm long GaAsSb insert and some SFs above the insert, as seen in the HRTEM image (figure 4 (a)). The simulated HAADF STEM intensity profile across the insert, assuming a uniform Sb concentration of 6% (figure 4(c), dashed black line), matches well the experimental intensity profile (figure 4(c), full blue line). The slight discrepancy between the profiles towards the NW wedges, i.e. the experimental intensity being lower than the simulated one, indicates that the Sb concentration is decreasing slightly towards the outer NW surfaces. This will be discussed further below.

The maximum Sb concentration along the insert obtained by quantitative HAADF STEM (6±1%) is much higher than the EDX point analysis result (1% at the insert centre), a value which fits well into the trend in figure 2. The Sb profile along the insert (figure 4(d)), taken from the 20 nm wide red box in figure 4(b), is slightly asymmetric and steeper towards the upper insert interface. The increase of the Sb concentration extends from the lower insert interface for ~ 15 nm. The maximum Sb concentration is reached for this insert exactly at the position of the 3 nm wide red box in figure 4(b), which is located slightly above the insert centre. The profile displays no plateau of even Sb concentration, and the concentration begins to decrease towards the upper insert interface immediately above the narrow region with 6% Sb (maximum). This is in accordance with observations from the EDX line scans for shorter inserts (see figure 3). The negative intensity minima that occur around the insert interfaces (figure 4(c)) are not due to compositional effects but are caused by surface strain relaxation at the insert interfaces and/or the SFs[16, 25].

The NW shown in figure 5 has a 64 nm long insert, which corresponds to the average insert length for the bare-core NWs. This NW has a 20 nm long 4H GaAs polytype segment directly above the GaAsSb insert. Regions with varying intensity can be observed within the insert in the HRTEM (figure 5(a)) and the HAADF STEM images (figure 5(b)). This intensity variation in both HRTEM and HAADF images indicates the presence of strain within the insert, or an inhomogeneous Sb

distribution. Similarly, intensity variations due to strain within the inserts were observed in DF TEM images for nearly all bare-core NWs analysed in this work (see for example the three inserts in figure 1), especially for those with longer inserts and higher Sb concentrations. Note that this type of intensity variation does not occur for the NW in figure 4, which had the maximum of 6% Sb (1% as determined by point EDX) and an extremely short insert.

For this NW the simulated HAADF STEM intensity profile across the insert, assuming a uniform Sb concentration of 15% (figure 5(c), dashed black line), does not fit well the experimental intensity profile (figure 5(c), full blue line). Especially at the NW wedges, the experimental intensity is clearly lower than the simulated intensity. This misfit is much more pronounced in figure 5(c) than in figure 4(c) and indicates that the Sb concentration is decreasing from the NW centre towards the outer surfaces of the NW, as mentioned previously. This misfit has been observed earlier for ZB GaAsSb inserts in Ga-assisted NWs[16]. The radial Sb gradient could be due to diffusion of Sb (i.e. exchange with As within the NW) towards the outer surfaces and evaporation of Sb into the MBE chamber during the growth of WZ GaAs core above the insert. This effect will be addressed in a future study.

The maximum Sb concentration along the insert is found to be 15±4%. The high error for this value is due to the strong intensity variations observed within the central part of the insert. Compared to the value of only 7% at the insert centre obtained from the EDX point analysis, quantitative HAADF STEM provided a much higher maximum Sb concentration for this NW as well. For the third NW, with a 54 nm long insert, analysed by quantitative HAADF STEM, a similar mismatch was present: quantitative HAADF STEM resulted in 13±4% Sb whereas the EDX point analysis gave only 6%.

The Sb concentration profile along the insert (figure 5(d)), taken from the 22.5 nm wide box in figure 5(b), appears to be slightly asymmetric towards the upper insert interface. The increase/decrease of the Sb concentration occurs over ~ 20 nm/15 nm from/towards the lower/upper insert interface. The Sb concentration reaches a plateau of almost even value in the central region of the insert. All this is in agreement with the the EDX line scan results for long inserts (see for example figure 3(a), NW with 11% Sb).

Presently, the quantitative HAADF STEM approach could not be applied to the core-shell NWs as there is no suitable model to account for the scattering from the AlGaAs shell. In addition, this approach could not be applied on the 50 nm thick SiN supports used for correlated PL-TEM, as the thick support affects the overall image contrast. Due to the lattice mismatch[6] between ZB GaAs and ZB GaSb, and the Sb concentration gradients within the ZB GaAsSb insert both along and across the insert, a certain amount of strain is expected and observed within the inserts especially for higher Sb concentrations. Based on the quantitative HAADF STEM study, we can conclude that the Sb richest region is located about the centre of the insert and the NW, and its size varies with the overall maximum Sb concentration and the insert length. The Sb concentrations determined by quantitative HAADF STEM and the EDX point analysis differ significantly in such a way that the simulated Sb

concentration is systematically higher for 5-8%. Therefore, an independent approach, here correlated PL-TEM, is needed to verify which of these two methods is more reliable (section 3.2).

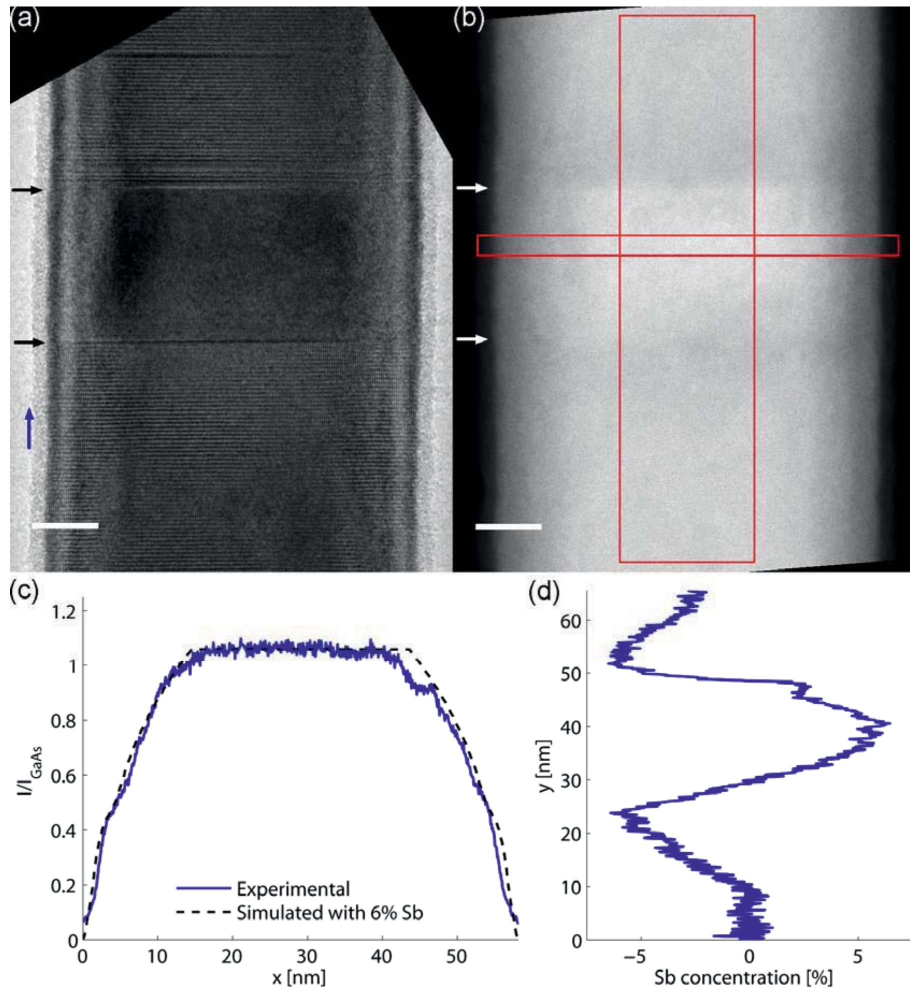

Figure 4. A bare-core NW with a 23 nm long ZB GaAsSb insert: (a) HRTEM image. The blue arrow shows the growth direction. (b) HAADF STEM image. The black and white arrows in (a) and (b) respectively mark the insert interfaces. The scale bars in (a) and (b) are 10 nm. (c) Relative experimental and simulated HAADF STEM intensity profiles across the insert (x-direction); the experimental profile (blue) averaged over the 3 nm wide red box in (b), and the simulated profile (black dashed) assuming an even distribution of 6% Sb. (d) The Sb concentration along the insert (y-direction), obtained from HAADF-STEM intensity profile averaged over the 20 nm wide red box in (b). Note that the negative concentrations at the interfaces are not related to composition variations, but are due to surface strain relaxation[16, 25].

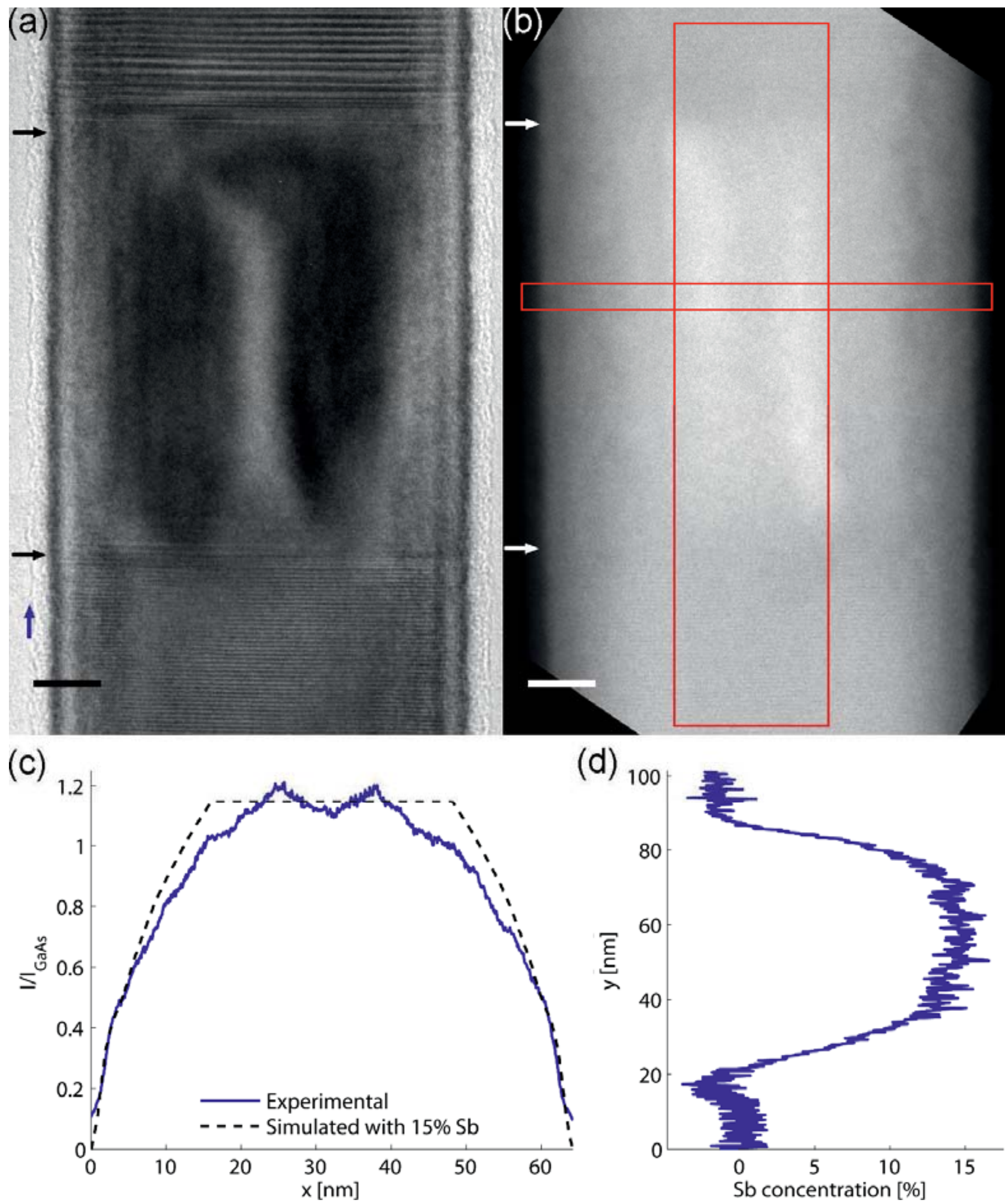

Figure 5. A bare-core NW with a 64 nm long ZB GaAsSb insert: (a) HRTEM image. The blue arrow shows the growth direction. (b) HAADF STEM image. The black and white arrows in (a) and (b) respectively mark the insert interfaces. The scale bars in (a) and (b) are 10 nm. (c) Relative experimental and simulated HAADF STEM intensity profiles across the insert (x-direction); the experimental profile (blue) averaged over the 3 nm wide red box in (b), and the simulated profile (black dashed) assuming an even distribution of 15% Sb. (d) The Sb concentration along the insert (y-direction), obtained from HAADF-STEM intensity profile averaged over the 22.5 nm wide red box in (b).

3.2 Correlated PL-TEM for the ZB GaAsSb inserts

The bare-core and core-shell NWs were studied by both PL and TEM to directly correlate the Sb composition results to the optical properties. An example of a representative bare-core NW, regarding both the structural and optical characteristics, is presented in figure 1(c), and will be discussed in more detail. The insert is 59 nm long and the EDX point analysis resulted in 6.9% Sb. Strain contrast is visible within the insert in the DF TEM in figure 1(c). The DF TEM image (figure 1(c)) further shows that there is a twinned single SF (~1 nm) at both insert interfaces, and some SFs below and above the insert.

Figure 6 shows the low temperature power-dependent PL spectra of the GaAsSb insert emission for this particular NW. Lorentzian lineshape fit (inset in figure 6) at a low excitation power (~ 566 W/cm^2) indicates that there are three distinct PL peaks at 1.249 eV, 1.261 eV, and 1.273 eV. In addition, a very weak PL peak is observed at 1.222 eV (not fitted), which is most probably a spectral artefact. At the lowest excitation power (283 W/cm^2), the PL emission at 1.261 eV is dominant and does not blueshift when the excitation power is increased. The PL peak at 1.273 eV and a couple of higher energy PL peaks appear and become dominant at higher powers. The PL peaks at 1.261 eV and 1.273 eV are attributed to the ground and an excited state of the GaAsSb insert, respectively.

To explain the origin of the insert related PL peaks in more detail, a qualitative band diagram for a typical ZB GaAsSb insert with the Sb concentration gradients towards the interfaces, in a WZ GaAs NW, is illustrated in figure 7. This band diagram is proposed based on the compositional results presented so far in this work, as explained in the following. Due to the increasing Sb concentration from the insert interfaces towards the central region of the insert, there is no sharp ZB GaAsSb/WZ GaAs heterojunction. Instead, there is a sharp WZ GaAs/ZB GaAs heterojunction at the insert interfaces, followed by a gradual transition from ZB GaAs to ZB GaAsSb. The twinned SFs at the insert interfaces can be considered as ZB GaAs as well, and they fall within the region of ~ 0% Sb at the beginning and/or at the end of the insert. The common understanding is that the WZ GaAs/ZB GaAs heterojunction has a type II band alignment[18, 31] with electrons confined in ZB GaAs and holes non-confined in WZ GaAs. The band alignment for ZB GaAs/GaAsSb heterojunction is also considered to be type II, for the Sb concentrations below 40%, with electrons weakly confined in ZB GaAs and holes strongly confined in ZB GaAsSb, according to the references[4, 5]. The Sb concentrations obtained in this work are well below this value. Thus, the central Sb-richest region of the ZB GaAsSb insert should have a type I band alignment with respect to the WZ GaAs barriers.

The insert PL emission (1.261 eV and 1.273 eV) can be assigned to transitions between electrons weakly confined, and holes more strongly confined in the GaAsSb insert (type I transition in figure 7), and occur in the Sb-richest central region of the insert. The absence of the blueshift for the ground and the excited state, as the excitation power increases (see figure 6), is characteristic for type I behaviour as reported previously[21, 23]. Further evidence for the type-I band alignment is the relatively strong emission generally obtained from the bare-core NWs (non-surface passivated), as shown in

figure 6. The radial gradient of the Sb concentration may act as self-passivation for the bare-core NWs, but not very efficiently as the depleted layer is thin. Indeed, for some bare-core NWs a higher PL intensity was observed than for others at the same excitation levels. However, as quantitative HAADF STEM could not be preformed on SiN support, it is unclear if these NWs had a larger radial gradient (as for example in figure 5(c)). Note that the intensity of the insert PL emission is in general much stronger for the core-shell NWs for the same range of the excitation powers.

The weak and broad peak at 1.249 eV is blueshifted for ~ 5 meV compared to the lowest excitation power, and merges with the insert ground state as the excitation power increases. Hence, this PL peak can be attributed to the type II transitions within the insert (see figure 7), between holes confined in ZB GaAsSb in the central region of the insert, and electrons confined in ZB GaAs near the insert interfaces. Note that the radial gradient of the Sb concentration may contribute to this type II transition as well.

Comparison of all bare-core and core-shell NWs with different structural defects in the insert region, as shown in figure 1, resulted in the conclusion that the isolated structural defects (single SFs, 4H) in the WZ GaAs core, at or near-by the insert interfaces, have no major contribution to the GaAsSb insert PL emission. A small number of twin planes (1-4) within the ZB GaAsSb inserts have no effect on the insert PL emission either, since the Sb gradient imposes the dominant effect.

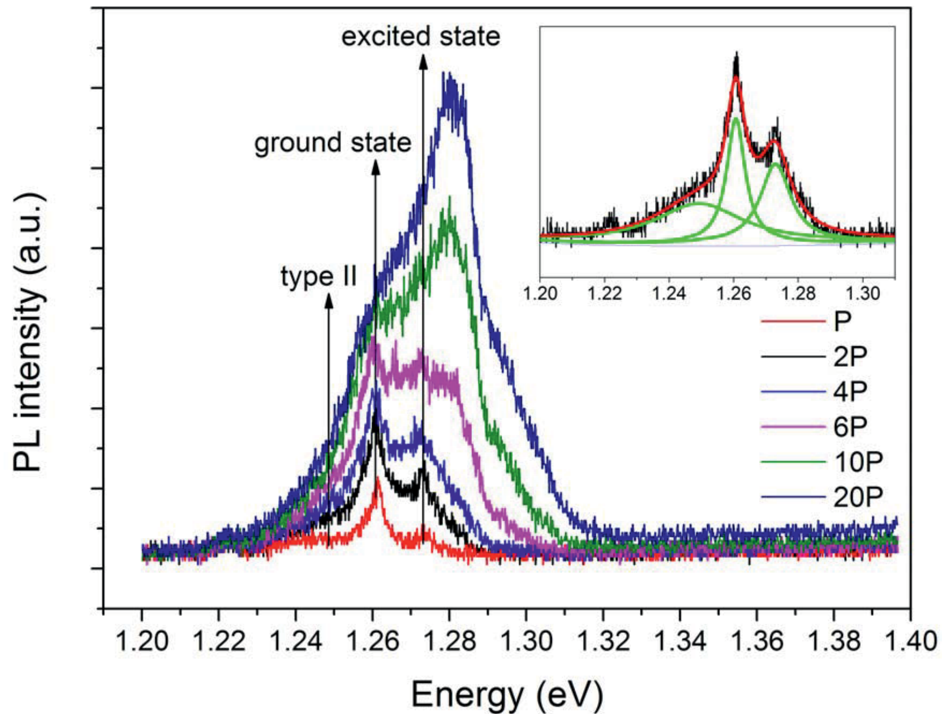

Figure 6: Low temperature power-dependent PL spectra of the NW shown in figure 1(c). (Inset) Lorentzian lineshape fit of the PL spectrum at 2P power density, where P=283 W/cm^2.

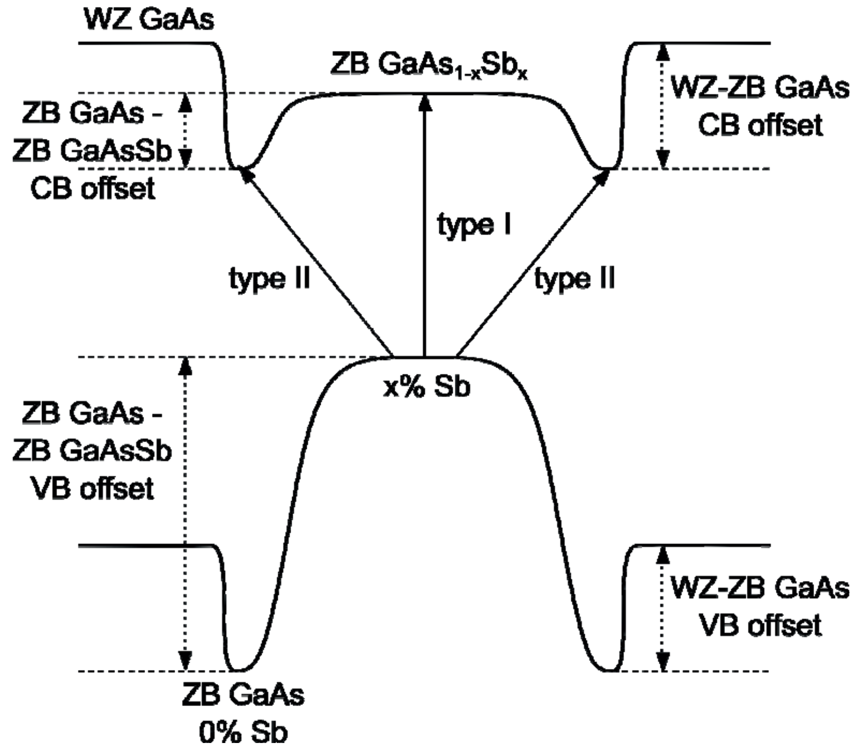

Figure 7: Proposed schematic band diagram for a ZB GaAsSb insert with a symmetric gradient of the Sb concentration (decreasing towards interfaces) along the insert, within WZ GaAs barriers. ZB GaAs (i.e. 0% Sb) is assumed at the insert interfaces with WZ GaAs. The band-alignment between WZ and ZB GaAs[18, 31], and between ZB GaAs and ZB GaAsSb[4, 5] is considered to be type II. The dashed lines qualitatively indicate the conduction (CB) and valence band (VB) offsets at the insert interfaces and within the insert. The arrows show two possible transition routes within the insert, type I and type II.

The ground state PL emission energies, obtained by fitting with Lorentzian or Lorentzian-Gaussian lineshape functions, were used to determine independently the Sb concentration in the inserts for all studied bare-core and core-shell NWs. An empirical model for low temperature bandgap of unstrained bulk $GaAs_{1-x}Sb_x$, according to Teissier et al.[5], was used to determine the Sb concentration, x, from the ground state PL emission energy. These results are presented in figure 8(a) together with the corresponding values obtained with the EDX point analysis. Figure 8(b) plots the Sb concentration determined optically as a function of the insert length (analogous to figure 2) and for comparison, includes the three NWs studied by quantitative HAADF STEM (section 3.1.4).

Notably, there is a significant systematic discrepancy between the Sb concentrations determined with the EDX point analysis and calculated from the PL emission energies. For example, the difference is 6% in favour of the calculated Sb concentration for the NW shown in figure 6. As can be

seen from figure 8(a), the calculated Sb concentrations are systematically offset to higher values, by 5-7 %, from the corresponding Sb concentrations obtained with EDX. At the same time, there is a good agreement with the Sb concentrations determined with the quantitative HAADF-STEM (see figure 8(b)). Hence, we can conclude that the strain has no major effect on the insert PL emission energy of GaAsSb inserts in these NWs.

Figure 8(b) shows a trend similar to the one in figure 2: the calculated Sb concentration increases with the increasing insert length, which is reflected in decreasing PL emission energy (figure 8(a)). As in figure 2, the inserts are generally shorter for the core-shell NWs and they have much lower Sb concentrations than in the bare-core NWs. Here however, a clear trend is present for the core-shell NWs as well, which could not be concluded with the EDX point analysis only.

It should be emphasized that this approach based on correlated PL-TEM, can be used both for bare-core and core-shell NWs, whereas the quantitative HAADF STEM approach used here can presently be only applied to the bare-core NWs. Rigorous HAADF-STEM analysis of core-shell NWs would require simulation of an entire core-shell NW, which is beyond our simulation capacity available at present. The EDX results for the core-shell NWs were not reliable either.

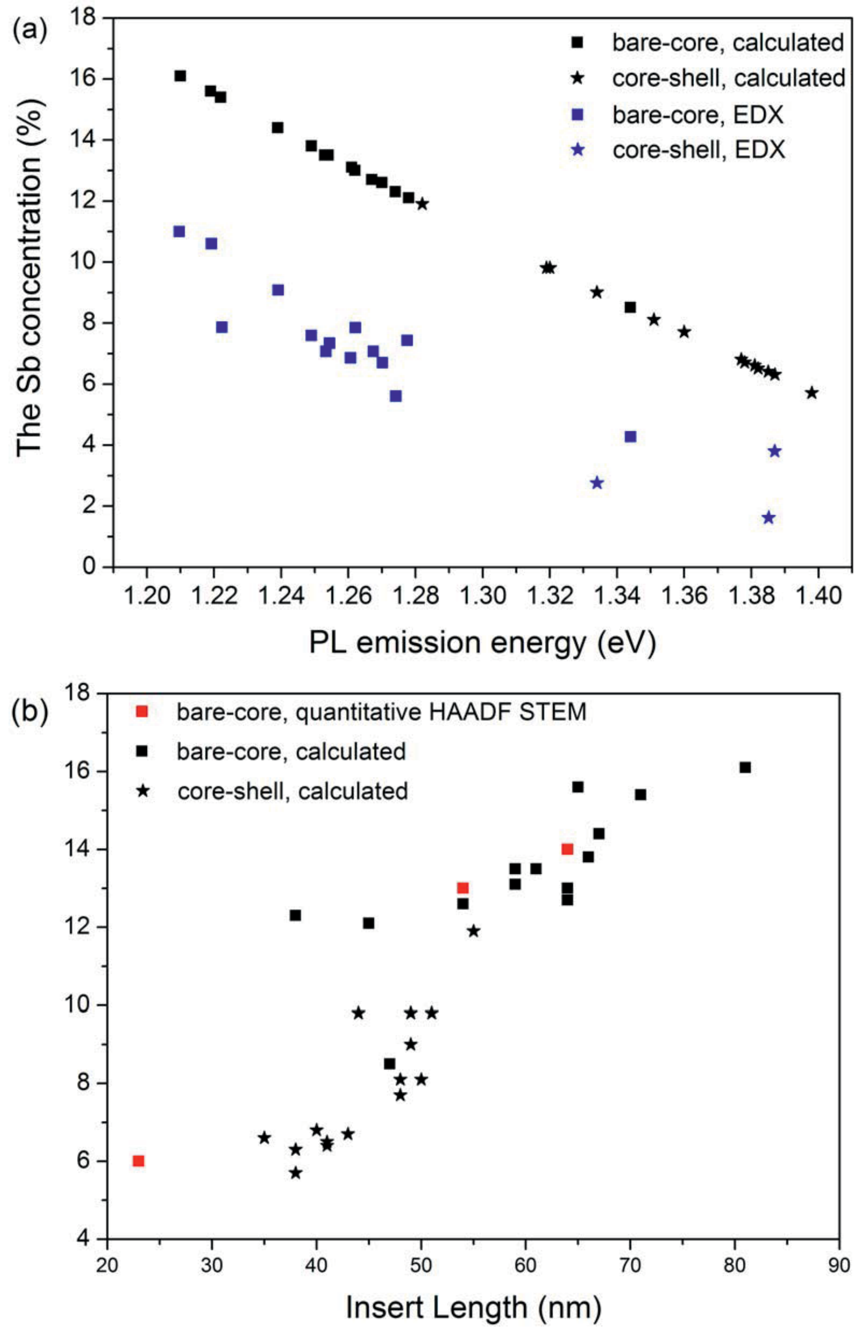

Figure 8. (a) The Sb concentration, determined using the model by Teissier et al.[5] (all PL-TEM NWs) and by the point EDX (17 PL-TEM NWs from figure 2), as a function of the ground state PL emission energy of the ZB GaAsSb insert, for the bare-core (squares) and core-shell (stars) NWs. (b) The optically determined Sb concentration for the NWs presented in (a) as a function of the insert length, together with the NWs studied by quantitative HAADF STEM (red squares).

4. Conclusions

In this work, the Sb concentration distribution within and variation among the ZB GaAsSb inserts, were investigated using different methods: EDX analysis, quantitative HAADF STEM and correlated PL-TEM. A large range of insert lengths and the Sb concentrations, for the same growth conditions for bare-core and core-shell NWs, was observed. This is probably due to a broad distribution of sizes of Au-Ga droplets. The longer the GaAsSb insert, the higher the NW growth rate and the more Sb is incorporated into the insert. This was evidenced by a clear trend of increasing insert length with increasing Sb concentration. The EDX analysis and the quantitative HAADF STEM confirmed that there is a decreasing Sb concentration gradient along the insert towards both insert interfaces, probably caused by in/out diffusion of Sb. In addition, quantitative HAADF STEM indicated that there is a radial gradient of the Sb concentration towards the outer surfaces.

The quantitative HAADF STEM provided systematically higher Sb concentrations (for 5-8%) compared to the automatic EDX quantification. On the other hand, the results from quantitative HAADF STEM were in agreement with the Sb concentrations calculated from the insert PL emission energies using a model for unstrained bulk GaAsSb. We conclude that the Sb concentrations obtained with quantitative HAADF STEM and PL methods are more reliable than the EDX results. The EDX point analysis clearly underestimates the Sb concentrations in ZB GaAsSb inserts in WZ GaAs NWs.

The ground state energy of the GaAsSb PL emission was found to decrease with the increase of the Sb concentration. No pronounced influence of the structural defects in the WZ GaAs core on the GaAsSb PL emission was found. In addition, strain appears to have no major effect on the insert PL emission. On the other hand, the Sb concentration gradient has an effect on the GaAsSb related PL emission. We believe that the observed type II transitions originate from recombinations of holes in the valence band of the central region of the insert (ZB GaAsSb), and electrons in the conduction band in the regions near-by the insert interfaces (ZB GaAs), due to the decreasing Sb concentration towards the interfaces. The type I transitions within the central Sb-richest region of the insert dominate in the insert related PL emission.

Acknowledgments

This work was supported by the "RENERGI" program (Grant No. 190871) of the Research Council of Norway. H. Kauko and A. T. J. van Helvoort thank the Faculty of Natural Sciences and Technology at NTNU for financial support.

References

1. M. T. Björk, C. Thelander, A. E. Hansen, L. E. Jensen, M. W. Larsson, L. R. Wallenberg and L. Samuelson, Nano Letters **4** (9), 1621–1625 (2004).
2. K. S. Leschkies, A. G. Jacobs, D. J. Norris and E. S. Aydil, Applied Physics Letters **95** (19), 193103 (2009).
3. M. P. van Kouwen, M. H. M. van Weert, M. E. Reimer, N. Akopian, U. Perinetti, R. E. Algra, E. P. A. M. Bakkers, L. P. Kouwenhoven and V. Zwiller, Applied Physics Letters **97** (11), 113108 (2010).
4. G. Liu, S.-L. Chuang and S.-H. Park, Journal of Applied Physics **88** (10), 5554 (2000).
5. R. Teissier, D. Sicault, J. C. Harmand, G. Ungaro, G. Le Roux and L. Largeau, Journal of Applied Physics **89** (10), 5473 (2001).
6. I. Vurgaftman, J. R. Meyer and L. R. Ram-Mohan, Journal of Applied Physics **89** (11), 5815 (2001).
7. Y. G. Sadofyev and N. Samal, Materials **3** (3), 1497-1508 (2010).
8. M. Baranowski, M. Syperek, R. Kudrawiec, J. Misiewicz, J. A. Gupta, X. Wu and R. Wang, Applied Physics Letters **98** (6), 061910 (2011).
9. J. B. Wang, S. Johnson, S. Chaparro, D. Ding, Y. Cao, Y. Sadofyev, Y. H. Zhang, J. Gupta and C. Guo, Physical Review B **70** (19) (2004).
10. D. L. Dheeraj, G. Patriarche, L. Largeau, H. L. Zhou, A. T. J. van Helvoort, F. Glas, J. C. Harmand, B. O. Fimland and H. Weman, Nanotechnology **19** (27), 275605 (2008).
11. D. L. Dheeraj, G. Patriarche, H. Zhou, T. B. Hoang, A. F. Moses, S. Grønsberg, A. T. J. van Helvoort, B.-O. Fimland and H. Weman, Nano Letters **8** (12), 4459-4463 (2008).
12. D. L. Dheeraj, G. Patriarche, H. Zhou, J. C. Harmand, H. Weman and B. O. Fimland, Journal of Crystal Growth **311** (7), 1847-1850 (2009).
13. T. Ba Hoang, A. F. Moses, L. Ahtapodov, H. Zhou, D. L. Dheeraj, A. T. J. van Helvoort, B.-O. Fimland and H. Weman, Nano Letters **10** (8), 2927-2933 (2010).
14. S. Plissard, K. A. Dick, X. Wallart and P. Caroff, Applied Physics Letters **96** (12), 121901 (2010).
15. D. B. Williams and C. B. Carter, *Transmission Electron Microscopy: A Textbook for Materials Science. Part 4: Spectrometry*. (2nd Edition, Springer, 2009).
16. H. Kauko, T. Grieb, R. Bjørge, M. Schowalter, A. M. Munshi, H. Weman, A. Rosenauer and A. T. J. van Helvoort, Micron, 10.1016/j.micron.2012.1007.1002 (2012).
17. J. Bao, D. C. Bell, F. Capasso, J. B. Wagner, T. Mårtensson, J. Trägårdh and L. Samuelson, Nano Letters **8** (3), 836-841 (2008).

18. M. Heiss, S. Conesa-Boj, J. Ren, H.-H. Tseng, A. Gali, A. Rudolph, E. Uccelli, F. Peiró, J. Morante, D. Schuh, E. Reiger, E. Kaxiras, J. Arbiol and A. Fontcuberta i Morral, Physical Review B **83** (4) (2011).
19. U. Jahn, J. Lähnemann, C. Pfüller, O. Brandt, S. Breuer, B. Jenichen, M. Ramsteiner, L. Geelhaar and H. Riechert, Physical Review B **85** (4), 045323 (2012).
20. A. T. J. van Helvoort, D. L. Dheeraj, H. Zhou, S. Grønsberg, G. Patriarche, B. Fimland and H. Weman, Journal of Physics: Conference Series **241**, 012084 (2010).
21. J. Todorovic, A. F. Moses, D. L. Dheeraj, P. Olk, B. O. Fimland, H. Weman and A. T. J. van Helvoort, Journal of Physics: Conference Series **326**, 012043 (2011).
22. H. L. Zhou, T. B. Hoang, D. L. Dheeraj, A. T. J. van Helvoort, L. Liu, J. C. Harmand, B. O. Fimland and H. Weman, Nanotechnology **20** (41), 415701 (2009).
23. J. Todorovic, A. F. Moses, T. Karlberg, P. Olk, D. L. Dheeraj, B. O. Fimland, H. Weman and A. T. J. van Helvoort, Nanotechnology **22** (32), 325707 (2011).
24. A. Rosenauer and M. Schowalter, Microscopy of Semiconducting Materials 2007 of Springer Proceedings in Physics **120**, 170–172 (2008).
25. V. Grillo, E. Carlino and F. Glas, Physical Review B **77** (5), 054103 (2008).
26. A. Rosenauer, K. Gries, K. Müller, A. Pretorius, M. Schowalter, A. Avramescu, K. Engl and S. Lutgen, Ultramicroscopy **109** (9), 1171-1182 (2009).
27. M. C. Plante and R. R. LaPierre, Journal of Crystal Growth **286** (2), 394-399 (2006).
28. V. G. Dubrovskii and N. V. Sibirev, Journal of Crystal Growth **304** (2), 504-513 (2007).
29. M. Yano, M. Ashida, A. Kawaguchi, Y. Iwai and M. Inoue, Journal of Vacuum Science & Technology B: Microelectronics and Nanometer Structures **7** (2), 199-203 (1989).
30. K. A. Dick, J. Bolinsson, B. M. Borg and J. Johansson, Nano Letters **12** (6), 3200-3206 (2012).
31. A. De and C. E. Pryor, Physical Review B **81** (15) (2010).